From structure to bioactivity : exploring confinement effects in multicompartment and multicomponent vesicles

Clémence Schvartzman

université de BORDEAUX

THÈSE PRÉSENTÉE

POUR OBTENIR LE GRADE DE

DOCTEUR DE

L'UNIVERSITÉ DE BORDEAUX

ÉCOLE DOCTORALE DES SCIENCES CHIMIQUES

SPÉCIALITÉ POLYMÈRES

Par Clémence SCHVARTZMAN

From Structure to Bioactivity: Exploring Confinement Effects in Multicompartment and Multicomponent Vesicles

Sous la direction du Pr. Sébastien LECOMMANDOUX

Soutenue le 28 Novembre 2023

Membres du jury :

Mme BASSEREAU Patricia	Directrice de Recherche, CNRS	Président
M. NASSOY Pierre	Directeur de recherche, CNRS	Examinateur
Mme PALIVAN Cornélia	Professeure, Université de Bâle	Rapporteur
M. TRIBET Christophe	Directeur de recherche, CNRS	Rapporteur
M. Van HEST Jan	Professeur, TU/e	Examinateur
M. MARTIN Nicolas	Chargé de Recherche, CNRS	Examinateur
M. LECOMMANDOUX Sébastien	Professeur, Bordeaux INP	Directeur de thèse

Remerciements

I would first of all like to express my gratitude to the members of my jury for agreeing to assess my work and for the engaging discussion during my defense. Special thanks to my referees, Cornelia Palivan and Christophe Tribet, my examiners, Jan Van Hest, Nicolas Martin, and Pierre Nassoy, and the president of the jury, Patricia Bassereau.

Je tiens à remercier mon directeur de thèse, Sébastien Lecommandoux, pour m'avoir accompagné tout au long de ce projet de thèse, de m'avoir permis de présenter mes travaux à de nombreuses conférences, et avant tout, de m'avoir fait découvrir ce surprenant et joli monde que sont les cellules artificielles.

This project received funding from the European Union's Horizon 2020 research and innovation program under the Marie Skłodowska-Curie Grant Agreement N° 859416. I am honored to have been part of such a program and express my gratitude to the Biomolmacs community, where I encountered remarkable individuals, discussed interesting topics, and had the opportunity to travel to incredible places for our meetings. This project has led to exciting collaborations, and I am grateful for the chance to contribute.
I also want to thank Professor Cornelia Palivan for hosting me in her research group, as well as Adi and Maria for their help during my stay.
I also thank Professor Petra Schwille for welcoming me into her research group.

I would like to thank Hang Zhao for his support during the first year of my PhD, sharing his knowledge, and facilitating a smooth continuation of my research. It has been a pleasure to collaborate with you.

Je voudrais remercier mon petit Manu pour son aide précieuse au confocal et tout au long de cette thèse. Merci pour ton soutien et pour tous nos moments de partage, passés à faire des parties de tennis, ramasser des prunes, chanter des chansons à tue-tête, et faire de nombreux paris (souvent perdus d'avance pour moi…). Merci pour ton humour grinçant, ta mauvaise foi et tes chantages aux gâteaux, ma thèse aurait bien été morose sans toi ! Petit scarabé est devenu grand.

En ce qui concerne le LCPO, je remercie toutes les personnes qui nous facilitent notre quotidien au sein du laboratoire : Dominique, Claude, Olivier, Séverine, Corinne et Emilie. Je remercie également les experts techniques de nous former et aider aux machines : Paul, Léna, Cédric, Sylvain, Frédérique, Amélie et Nina.

Je voudrais remercier mes collègues du groupe 3 : Julien, Albanito, Sifan, Leslie, Eloïse, Rosanna, Hannah, Antoine, Anouk, Mostafa, Yupei, Valentin, Sarah, Yue, Dongxu, Martin, Ségolène, Pedro; mais également ceux du groupe 1 et 2 que j'ai pu rencontrer sur le chemin du confocal: Zakir, Quentin, Manon, Florent, Yelin, Maëva, Clémence, Simon, Clément, Nichollas, Alexandre, Marie, Arthur, Romain, Solène, Azmil, Barbara, Coco, Toto, Zoi, Ana, Thomas D. Je voudrais également remercier Vusala Ibrahimova pour la synthèse des ELPs et conjugués utilisés lors de ma thèse. Je remercie également Bertrand Garbay pour son aide et expertise en enzymologie.

Je tiens également à remercier ma stagiaire, Manon, toujours super motivée ! Quel trio de choc nous formions avec Manu, vivent le rose et le vert fluo ! Sans oublier Harmony, ma stagiaire par alliance. Merci à vous deux pour votre bonne humeur et les bons moments passés ensemble.

Merci à mes ami.e.s du du lycée, de la fac, des Erasmus et de longue date : Mona, Justine, Mathilde, Flore, Alizée, Théo, Maxi, Elise, Quentin, Hugo, Joan… Merci d'avoir suivi cette thèse de près ou de loin, mais surtout d'avoir fait le déplacement pour me soutenir et m'encourager le jour J !

Je remercie également Dijwar pour ces trois années de thèse que nous avons vécues ensemble, à nous soutenir dans les hauts et les bas que peut offrir une thèse. Nous partons avec de nombreux souvenirs de voyages et de conférences à travers le monde, de prix, de stratégies habiles pour gagner au time bomb, de séjours sympathiques aux urgences, qui ont pimenté notre quotidien, et j'en passe !

Enfin, merci à mes parents, mon frère, Jules, et ma sœur, Alice, pour leur soutien infaillible durant ces 3 années de thèse, et bien plus encore ! Merci d'avoir toujours été là et de m'avoir aidé à m'épanouir. C'est grâce à vous que j'en suis là aujourd'hui.

List of abbreviations

ABTS	2,2'-azinobis(3-ethylbenzothiazoline-6-sulfonic) acid
AC	Artificial Cell
ADH	Alcohol Dehydrogenase
ADP	Adenosine Diphosphate
AR	Amplex Red
ATP	Adenosine Triphosphate
ATPS	Aqueous Two-Phase System
BDP	Bodipy
BSA	Bovine Serum Albumin
Cy5.5	Cyanine 5.5
DLS	Dynamic Light Scattering
DMSO	Dimethylsulfoxide
DNA	Deoxyribonucleic Acid
DOPC	1,2-dioleoyl-sn-glycero-3-phosphocholine
DPPC	Dipalmitoyl-sn-glycero-3-phosphocholine
E. coli	Escherichia Coli
Egg-PC	L-α-phosphatidylcholine
ELP	Elastin Like Polypeptide
FCCS	Fluorescence Cross-Correlation Spectroscopy
FCS	Fluorescence Correlation Spectroscopy
FITC	Fluorescein Isothiocyanate
GOx	Glucose Oxidase
GPMVs	Giant Plasma Membrane Vesicles
GUV	Giant Unilamellar Vesicle
H_2O_2	Hydrogen Peroxide
HA	Hyaluronic Acid
HRP	Horseradish Peroxidase
IDPs	Intrinsically Disordered Proteins
IMVs	Inverted Membrane Vesicles
ITO	Indium Tin Oxide
IVTx	In Vitro Transcription
kD	kiloDalton
LCST	Lower Critical Solubility Temperature
LLPS	Liquid-Liquid Phase Separation
LUV	Large Unilamellar Vesicle

List of abbreviations

MVD	Multivesicular Droplet
NADPH	Nicotinamide Adenine Dinucleotide Phosphate
NO	Nitric Oxide
PBut-*b*-PEO	Poly(butadiene)-*b*-poly(ethylene oxide)
PEG	Poly(ethylene glycol)
POPC	Phosphatidylcholine
PVA	Poly(vinyl alcohol)
RNA	Ribonucleic Acid
T_{cp}	Cloud Point Temperature
UV	Ultraviolet
UV-Vis	Ultraviolet-Visible
W/O	Water-in-Oil
W/O/W	Water-in-Oil-in-Water
α-HL	Alpha Hemolysin

Résumé général - De la structure à la bioactivité : étude des effets de confinement dans les vésicules multi-compartimentées et multicomposantes

L'apparition de la vie sur Terre demeure une question fondamentale que les scientifiques cherchent à résoudre depuis des siècles. De nombreuses hypothèses ont été émises afin d'élucider ces mécanismes, comme la théorie de la « soupe primordiale », proposée dans les années 1920 par Oparin et Haldane.[1] Cette théorie suggère qu'il y a environ 4 milliards d'années, les conditions rudimentaires sur la planète, marquées par une intense activité volcanique, de fréquentes tempêtes et une pénurie d'oxygène, ont fourni les conditions idéales à la synthèse de molécules organiques telles que les acides aminés, les sucres, les nucléotides et les acides gras. Au fil du temps, ces composés organiques se sont accumulés dans les océans, formant une riche « soupe primordiale » de molécules complexes où des réactions chimiques ont eu lieu, conduisant à la formation de molécules plus complexes telles que l'ARN.[2] Ces molécules pourraient avoir donné naissance aux premières formes primitives de la vie, connues sous le nom de protocellules. Ces dernières sont considérées comme les précurseurs des cellules biologiques actuelles. En effet, bien que les protocellules manquent de la complexité des cellules modernes, elles présentent tout de même des propriétés similaires telles que la compartimentalisation et la capacité à effectuer des fonctions de base, jouant un rôle crucial dans l'évolution de la vie et le développement de formes cellulaires plus avancées.[3] La cellule, l'unité de base de la vie, commune à tous les organismes vivants, fascine les scientifiques en raison de sa structure complexe et multicompartimentée.[4] Dans le domaine de la biologie, on distingue des sous-compartiments distincts, appelés organites, qui créent des microenvironnements spécialisés avec une partition sélective des biomolécules et des fonctions spécifiques. On retrouve les organites avec membrane[5–7] et les organites sans membrane, [8-10] assurant une régulation spatiale et temporelle.[11–13] Les chercheurs ont développé des modèles synthétiques intégrant ces structures multi-compartimentées en utilisant des vésicules lipidiques et polymères, afin d'imiter certains aspects biologiques des cellules.[9,14–23]

Cependant, la plupart de ces reconstructions tendent à séparer les organites avec membranes et sans membrane, ce qui ne reflète pas exactement la structure et manière dont ces organites travaillent ensemble pour réguler les fonctions cellulaires. Pour répondre à cette problématique, nous avons proposé dans le **Chapitre II** une conception structurelle simple utilisant des liposomes produits par microfluidique (Figure 1), intégrant en leur sein des organites membranaires synthétiques, fabriquées à partir de nanovésicules auto-assemblées de PEG_{22}-*b*-$PTMC_{51}$-$Cy_{5.5}$, et des organites sans membrane synthétiques, faites à partir de la séparation de phase liquide-liquide (SPLL) de protéines thermosensibles ELP[M1V3-80] (Figure 2). Cette structure vise à ressembler davantage à la structure cellulaire naturelle et à permettre une étude plus approfondie de leurs interactions. Nous avons démontré que les organites synthétiques coexistaient et accomplissaient leurs tâches respectives à l'intérieur des vésicules. Ce prototype est unique car il combine plusieurs composants cellulaires vitaux, et a le potentiel d'ouvrir la voie au développement de cellules artificielles avancées qui reproduisent les comportements des cellules vivantes. Cette avancée crée des opportunités intéressantes pour le développement de cellules artificielles par une approche « bottom-up » ou ascendante, ainsi que pour l'exploration de nouvelles fonctions et interactions entre ces deux types d'organites, tout comme le ferait une cellule eucaryote naturelle.

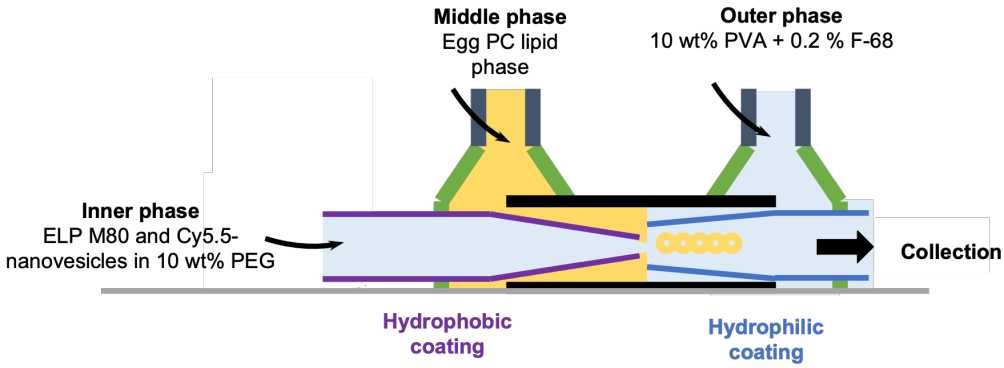

Figure 1: Production de doubles émulsions eau-dans-huile-dans-eau à l'aide d'un dispositif microfluidique permettant de reproduire des systèmes complexes multi-compartimentés.

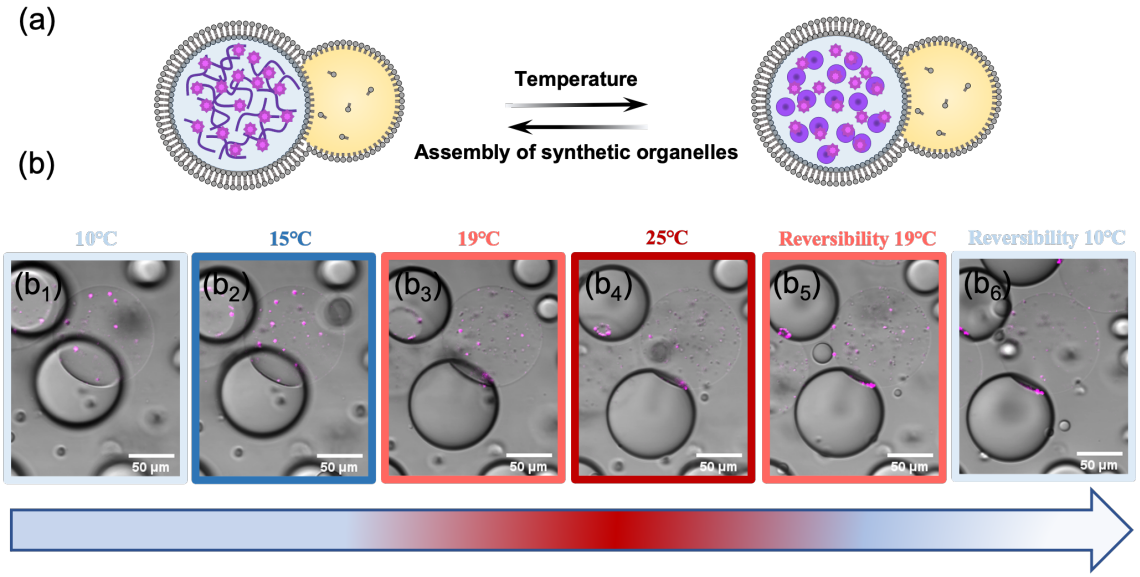

Figure 2: Encapsulation d'organites synthétiques avec membrane et sans membrane (a) Schéma illustrant des vésicules encapsulant des nanovésicules de PEG_{22}-b-$PTMC_{51}$ marquées Cy5.5 et ELP-M80 avant et après une séparation de phase lorsque le point critique de température (T_{cp}) est atteint. (b) Rampe de température appliquée à un échantillon de microgouttelettes partiellement démouillées. La présence d'organites PEG_{22}-b-$PTMC_{51}$-Cy5.5 membranaires est indiquée par la présence de points roses. L'auto-assemblage et le désassemblage des organites sans membrane ELP M80 sont indiqués par la présence des points noirs.

Dans le **Chapitre III**, nous avons particulièrement concentré notre projet sur le développement et le contrôle de la SPLL de polypeptides élastine-like thermo-sensibles afin d'assembler des organites sans membrane (Figure 3). En effet, en réponse aux variations de stress osmotique, les cellules ont développé des mécanismes complexes pour libérer leur excès d'eau, évitant ainsi leur éclatement et leur mort. Lorsque l'eau est expulsée, les cellules rétrécissent et concentrent leur contenu bio(macro)moléculaire interne, induisant la formation d'organites sans membrane suite à un mécanisme de SPLL. Pour imiter cette propriété intrinsèque des cellules, des conjugués biomacromoléculaires thermo-réactifs à base d'élastine-like polypeptide (ELP) sont encapsulés dans des vésicules lipidiques auto-assemblées à l'aide d'un système de microfluidique, avec du polyéthylène glycol (PEG) pour imiter le microenvironnement encombré des cellules. En provoquant un choc hypertonique sur les vésicules, l'eau expulsée induit une augmentation locale de la concentration et une diminution concomitante du point critique de température (T_{cp}) des bioconjugués ELP qui se séparent en phase et forment des coacervats imitant les assemblages d'organites sans membrane induits par le stress cellulaire. La peroxydase de raifort (HRP), en tant

qu'enzyme modèle, est bioconjuguée aux ELP et est localement confinée dans les coacervats en réponse au stress osmotique. Cela induit un confinement de l'enzyme HRP et de son substrat, accélérant la cinétique de la réaction enzymatique (Figure 4). Ces résultats illustrent une façon unique d'ajuster dynamiquement les réactions enzymatiques en réponse à un changement physiologique dans des conditions isothermes.

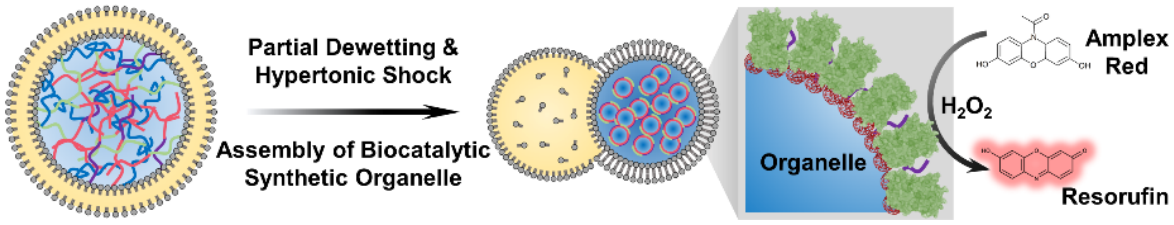

Figure 3: Organites catalytiques synthétiques construites à partir du co-assemblage d'un système multicomposant complexe à base d'ELP. (a) Schéma illustrant le co-assemblage induit par le choc osmotique de BDP-ELP, ELP-b-PEG et ELP-b-HRP formant des organites synthétiques capables de catalyser un substrat chimique, l'amplex red, en un produit, la resorufine, lorsqu'ils sont exposés à un substrat tel que le H_2O_2 dans l'environnement environnant.

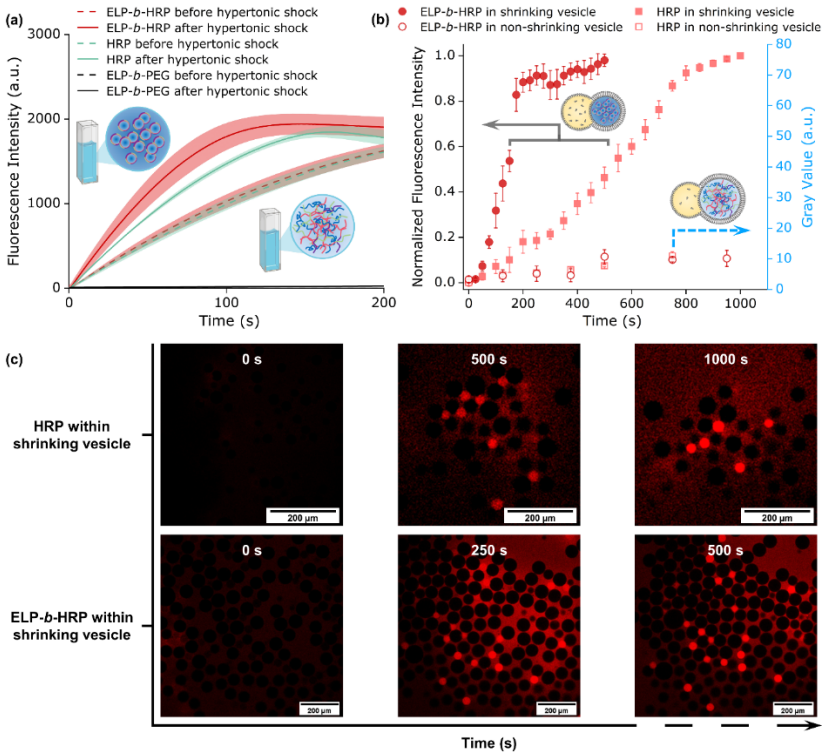

Figure 4: Cinétique de la réaction enzymatique du système multicomposant à base d'ELP et du système HRP libre avant et après un choc hypertonique, respectivement. (a) Suivit cinétique des réactions enzymatiques détectée avec un spectrofluorimètre. (b) Réaction enzymatique se produisant dans les vésicules avant et après un choc hypertonique, comparaison faite entre du systèmes ELP-b-HRP et HRP libre. (c) Série d'images de microscopie confocale dans le canal rouge pour suivre la formation de resorufine après le choc hypertonique dans les vésicules encapsulant la HRP libre et le système ELP-b-HRP, respectivement.

Enfin, la spectroscopie de corrélation de fluorescence a été utilisée pour caractériser la capacité des coacervats d'ELP à partitionner des enzymes. Dans le **Chapitre IV**, nous approfondissons notre compréhension des coacervats d'ELP qui ont été utilisés dans le chapitre précédent, en démontrant qualitativement leur capacité à partitionner certaines molécules (Figure 5), et en observant comment cette partition peut influencer la cinétique des réactions enzymatiques. Nous avons tout d'abord montré qu'une seule enzyme (la HRP) peut être efficacement confinée dans des coacervats d'ELP libre, conduisant à une accélération de la réaction enzymatique, sans avoir besoin de recourir à une réaction de bioconjugaison. Le système a été complexifié et une réaction en cascade combinant GOx et HPR a été testée dans les même conditions. L'analyse cinétique résultante nous a permis de conclure sur la faible probabilité de co-encapsuler deux enzymes dans un seul coacervat, renforcée par des observations de microscopie confocale. Pour résoudre

éventuellement ce problème, la taille des coacervats pourrait être augmentée pour avoir une plus grande probabilité d'avoir plusieurs enzymes dans un même coacervat. L'autre solution possible pourrait consister à conjuguer chaque enzyme à un ELP, comme cela a été fait dans notre travail précédent, toujours afin d'augmenter les chances de les retrouver ensemble dans un même coacervat.

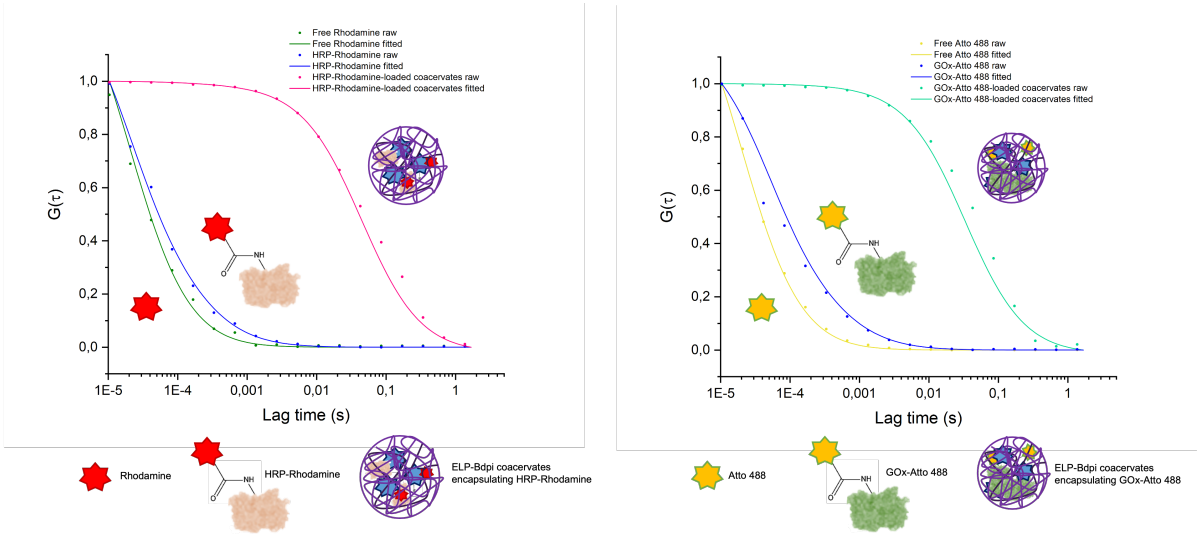

Figure 5: a) Courbes d'autocorrélation FCS normalisées du colorant rhodamine libre (vert), de la HRP marquée à la rhodamine (bleu) et des coacervats marqués Bdpi encapsulant HRP-Rhodamine (rose) b) Courbes d'autocorrélation FCS normalisées du colorant Atto 488 libre (jaune), de la GOx marquée à l'Atto 488 (bleu) et des coacervats marqués Bdpi encapsulant GOx-Atto 488 (vert). Points : bruts. Lignes pleines : courbes ajustées.

Toutes ces avancées ouvrent des opportunités passionnantes pour le développement de cellules artificielles avec des structures élaborées par assemblage « bottom-up », ainsi que l'exploration de nouvelles fonctions complexes et de plus en plus similaires à celles des cellules eucaryotes.

Références

[1] A. Oparin, *Nature* **1938**, *142*, 412–413.
[2] B. Ghosh, R. Bose, T.-Y. D. Tang, *Current Opinion in Colloid & Interface Science* **2021**, *52*, 101415.
[3] P. Stano, *Life* **2018**, *9*, 3.
[4] J. W. Szostak, D. P. Bartel, P. L. Luisi, *Nature* **2001**, *409*, 387–390.
[5] N.-N. Deng, M. Yelleswarapu, L. Zheng, W. T. S. Huck, *J. Am. Chem. Soc.* **2017**, *139*, 587–590.
[6] A. Peyret, E. Ibarboure, N. Pippa, S. Lecommandoux, *Langmuir* **2017**, *33*, 7079–7085.
[7] R. J. R. W. Peters, M. Marguet, S. Marais, M. W. Fraaije, J. C. M. van Hest, S. Lecommandoux, *Angew. Chem. Int. Ed.* **2014**, *53*, 146–150.
[8] D. M. Mitrea, R. W. Kriwacki, *Cell Commun Signal* **2016**, *14*, 1.
[9] W. Mu, Z. Ji, M. Zhou, J. Wu, Y. Lin, Y. Qiao, *Sci. Adv.* **2021**, *7*, eabf9000.
[10] N. G. Moreau, N. Martin, P. Gobbo, T.-Y. D. Tang, S. Mann, *Chem. Commun.* **2020**, *56*, 12717–12720.
[11] M. Marguet, C. Bonduelle, S. Lecommandoux, *Chem. Soc. Rev.* **2013**, *42*, 512–529.
[12] R. Roodbeen, van Hest J. C. M., *BioEssays* **2009**, *31*, 1299–1308.
[13] P. A. Beales, B. Ciani, S. Mann, *Interface Focus.* **2018**, *8*, 20180046.
[14] S. Cao, L. C. da Silva, K. Landfester, *Angewandte Chemie International Edition* **2022**, *61*, e202205266.
[15] N. Deng, W. T. S. Huck, *Angew. Chem. Int. Ed.* **2017**, *56*, 9736–9740.
[16] H. Zhao, E. Ibarboure, V. Ibrahimova, Y. Xiao, E. Garanger, S. Lecommandoux, *Advanced Science* **2021**, *8*, 2102508.
[17] H. Zhao, V. Ibrahimova, E. Garanger, S. Lecommandoux, *Angew. Chem. Int. Ed.* **2020**, *59*, 11028–11036.
[18] A. T. Rowland, D. N. Cacace, N. Pulati, M. L. Gulley, C. D. Keating, *Chem. Mater.* **2019**, *31*, 10243–10255.
[19] J. W. Hindley, D. G. Zheleva, Y. Elani, K. Charalambous, L. M. C. Barter, P. J. Booth, C. L. Bevan, R. V. Law, O. Ces, *Proc. Natl. Acad. Sci. U.S.A.* **2019**, *116*, 16711–16716.
[20] S. Deshpande, F. Brandenburg, A. Lau, M. G. F. Last, W. K. Spoelstra, L. Reese, S. Wunnava, M. Dogterom, C. Dekker, *Nat Commun* **2019**, *10*, 1800.
[21] C. Xu, N. Martin, M. Li, S. Mann, *Nature* **2022**, *609*, 1029–1037.
[22] H. Seo, H. Lee, *Nat Commun* **2022**, *13*, 5179.
[23] T. E. Miller, T. Beneyton, T. Schwander, C. Diehl, M. Girault, R. McLean, T. Chotel, P. Claus, N. S. Cortina, J.-C. Baret, T. J. Erb, *Science* **2020**, *368*, 649–654.

General Introduction

The term Biomimicry (from the Greek words *bios*, meaning 'life', and *mimesis*, meaning imitation[1]) is a cutting-edge field at the intersection of biology, engineering, and design. It draws inspiration from our remarkable nature to create novel solutions for human challenges. One of the most famous examples of biomimicry is the Velcro®, which was inspired by the way burrs stick to animal fur.[2] The engineer George de Mestral developed this hook-and-loop fastening system that has since then found applications in clothing, footwear, and various industries. This illustrates the incredible potential of biomimicry to revolutionize various fields, demonstrating how nature's solutions can be translated into innovative human technologies and used to address complex problems in various industries. One captivating route within biomimicry is the concept of artificial cells, which seeks synthetically reproduce the fundamental characteristics of living cells.

Cells are the fundamental and structural building blocks of life, universally present in all living organisms.[3] The complexity of their structure has captivated scientists, and their evolution over time continues to intrigue the scientific communities. Originally, the exploration of artificial cells emerged as an interest to comprehend the origins of life. Over time, this curiosity shifted towards investigating the various constituents of cells and their intricate interplay. This led to the development of primary rudimental artificial cells, which quickly developed to highly sophisticated synthetic cell-like structures designed to emulate specific aspects of natural cells like compartmentalization,[4,5] growth,[6] communication,[7] and motility.[8] Moreover, artificial cells have been ingeniously integrated with actual living systems and complex genetic circuits to expand the spectrum of behaviours that can be performed.[9] The essential components used to construct the framework of artificial cells draw inspiration from nature, and include substances like lipids,[10] polymers,[11,12] coacervates,[13] proteins,[14,15] and hydrogels.[16] Today, artificial cells combine the fusion of biological knowledge and technological prowess. By harnessing the principles of cellular biology and applying them to engineering, researchers aim to develop artificial cells with unprecedented applications as smart carriers for drug delivery, synthetic cell therapies, diagnostic sensors, chemical microreactors, and as microscale biofoundries.[17–19]

In the frame of this PhD project that deals with biomimicry and artificial cells, we have delved into the captivating world of nature-inspired innovations and attempted to understand how scientists and engineers work to unlock the potential of these synthetic cell analogs. This manuscript summarizes our findings and is organized in four chapters. **Chapter I** is an overview of the literature on the recent advancements made in constructing synthetic cells with high order of complexity in structuration and functionality. The most common methods of producing artificial cells are described, as well as their use in constructing membranebound and membraneless multicompartmentalized systems. **Chapter II** presents the co-encapsulation of these two types of organelles in a cell-like chassis, as step forward in structurally resembling eukaryotic cells. **Chapter III** focuses on the dynamic assembly of intracellular membraneless organelles used to control an enzyme reactivity in response to using a biologically relevant stimulus, osmotic pressure modulation. **Chapter IV** offers a more qualitative analysis of the uptakes and interactions between the coacervates and the enzymes, notably using Fluorescence Correlation Spectroscopy analysis. Finally, we will conclude on this PhD work and offer perspectives for future developments.

References

[1] J. M. Benyus, *Biomimicry: Innovation Inspired by Nature*, Morrow, New York, **1997**.
[2] F. N. Hapsari, R. Purwaningsih, F. Azzahra, D. P. Sari, *IOP Conf. Ser.: Earth Environ. Sci.* **2022**, *1111*, 012057.
[3] M. Marguet, L. Edembe, S. Lecommandoux, *Angew. Chem.* **2012**, *124*, 1199–1202.
[4] G. Zubaite, J. W. Hindley, O. Ces, Y. Elani, *ACS Nano* **2022**, *16*, 9389–9400.
[5] H. Niederholtmeyer, C. Chaggan, N. K. Devaraj, *Nat Commun* **2018**, *9*, 5027.
[6] N. J. Gaut, J. Gomez-Garcia, J. M. Heili, B. Cash, Q. Han, A. E. Engelhart, K. P. Adamala, *ACS Synth. Biol.* **2022**, *11*, 855–866.
[7] B. C. Buddingh', J. Elzinga, J. C. M. van Hest, *Nat Commun* **2020**, *11*, 1652.
[8] S. Zhang, C. Contini, J. W. Hindley, G. Bolognesi, Y. Elani, O. Ces, *Nat Commun* **2021**, *12*, 1673.
[9] Y. Elani, *Angew. Chem. Int. Ed.* **2021**, *60*, 5602–5611.
[10] C. Guindani, L. C. Da Silva, S. Cao, T. Ivanov, K. Landfester, *Angew Chem Int Ed* **2022**, *61*, DOI 10.1002/anie.202110855.
[11] E. Rideau, R. Dimova, P. Schwille, F. R. Wurm, K. Landfester, *Chem. Soc. Rev.* **2018**, *47*, 8572–8610.
[12] Y. Lu, G. Allegri, J. Huskens, *Mater. Horiz.* **2022**, *9*, 892–907.
[13] Z. Lin, T. Beneyton, J. Baret, N. Martin, *Small Methods* **2023**, 2300496.
[14] X. Huang, M. Li, D. C. Green, D. S. Williams, A. J. Patil, S. Mann, *Nat Commun* **2013**, *4*, 2239.
[15] X. Huang, A. J. Patil, M. Li, S. Mann, *J. Am. Chem. Soc.* **2014**, *136*, 9225–9234.

[16] M. E. Allen, J. W. Hindley, N. O'Toole, H. S. Cooke, C. Contini, R. V. Law, O. Ces, Y. Elani, *Proc. Natl. Acad. Sci. U.S.A.* **2023**, *120*, e2307772120.
[17] G. Chen, R. Levin, S. Landau, M. Kaduri, O. Adir, I. Ianovici, N. Krinsky, O. Doppelt-Flikshtain, J. Shklover, J. Shainsky-Roitman, S. Levenberg, A. Schroeder, *Proc. Natl. Acad. Sci. U.S.A.* **2022**, *119*, e2207525119.
[18] A. Groaz, H. Moghimianavval, F. Tavella, T. W. Giessen, A. G. Vecchiarelli, Q. Yang, A. P. Liu, *WIREs Nanomedicine and Nanobiotechnology* **2021**, *13*, e1685.
[19] E. Cho, Y. Lu, *ACS Synth. Biol.* **2020**, *9*, 2881–2901.

Chapter I - Synthetic Cells with High Order of Complexity in Structuration and Functionality – State of the Art

1. Introduction

How life has emerged on Earth remains a deep, fundamental question that scientists have been longing to answer for centuries. Many hypothesis were proposed to unveil these mechanisms, such as the primordial soup theory, proposed in the 1920s by Oparin and Haldane.[1] This theory suggests that around 4 billion years ago, the rudimentary conditions on the planet with intense volcanic activity, frequent lightning storms and oxygen scarcity provided the necessary conditions for the synthesis of organic molecules such as amino acids, sugars, nucleotides, and fatty acids. Over time, these organic compounds accumulated in the oceans, forming a rich "primordial soup" of complex organic molecules where further chemical reactions and interactions occurred, leading to the formation of more complex molecules including self-replicating molecules like RNA.[2] Eventually, these self-replicating molecules could have given rise to the first primitive forms of life, known as protocells. These latter are considered to be precursors of current biological cells as they exhibited similar properties such as compartmentalization and the ability to carry out basic functions. Protocells may have been composed of simple molecules, such as lipids or fatty acids, that formed membrane-like structures, enclosing self-replicating molecules and providing some degree of protection. While protocells lack the complexity of modern cells, they played a crucial role in the evolution of life and the development of more advanced cellular forms.[3] The cell, the basic unit of life, common to any living organism, has fascinated scientists for its highly complex and multi-compartmentalized structure.[4] This feature allows eukaryotic cells to spatiotemporally control and drive key biological events without interfering with one another, crucial for the cell's development and survival.[5–7] Distinct subcompartments in biology, known as organelles, create specialized microenvironments with selective partitioning of biomolecules and specific functions. Two main types of organelles exist within eukaryotic cells, membranebound and membraneless

organelles. Membranebound organelles, such as lysosomes and the nucleus, are self-assembled structures containing a subcellular aqueous environment surrounded by a fluidic unilamellar (phospho)lipid membrane.[8–10] Membraneless organelles, like the nucleolus and P-bodies, are devoid of any lipid boundary.[11–13] Compartmentalization is undeniably one of the most important features of eukaryotic cells, and is, along with energy supply, metabolism, protein expression, communication, replication of genetic material, growth, division, and motility,[14–17] one of the most relevant functions to be mimicked when constructing artificial cells (Figure 6). Building and mimicking protocells with life-like properties has been one of the challenges of recent decades, as the first artificial cell attempt was made in 1957 by Chang.[18] Ever since, artificially constructing and mimicking these eukaryotic cells has been a great challenge, guided by three kinds of motivation. The first one, key driver to develop research in this field, is related to the origins of life, where building protocellular systems helps understanding how life arose and developed in the early earth.[2,3,19] The second motivation is to use artificial cells to study, in a simplified but highly controlled way, the global functioning of these complex systems and multi-step biological processes.[2,20] Remarkable progress has been made, notably in the bottom-up construction of complex, multicompartment artificial cells, in order to understand how primitive cells could have emerged from non-biological components.[12,21–30] The third and final motivation lies in the potential of artificial cells to serve as soft, responsive micromachines, specifically engineered to perform useful biotechnological functions and serve in applications such as drug delivery,[31–33] sensing agents[32,34] and microreactors[15,35–37] to their use as chassis for artificial cells[38,39] and tissue mimics.[40–42]

In this state of the art chapter, we will discuss about the latest and promising developments in the design and construction of new types of multicompartmentalized artificial cells, as well as delve into the latest improvements to mimic living cell functionalities and their real-world applications. In a first part, we will review the most frequent techniques used to develop such kind of artificial cell structures. Then, we will focus on the latest approaches used to develop complex cellular structures enclosed by membranes. Finally, we will closely investigate the recent advancements in the incorporation of Liquid-Liquid Phase Separation systems into artificial cells, highlighting the diverse creative strategies and stimuli applied upon these systems.

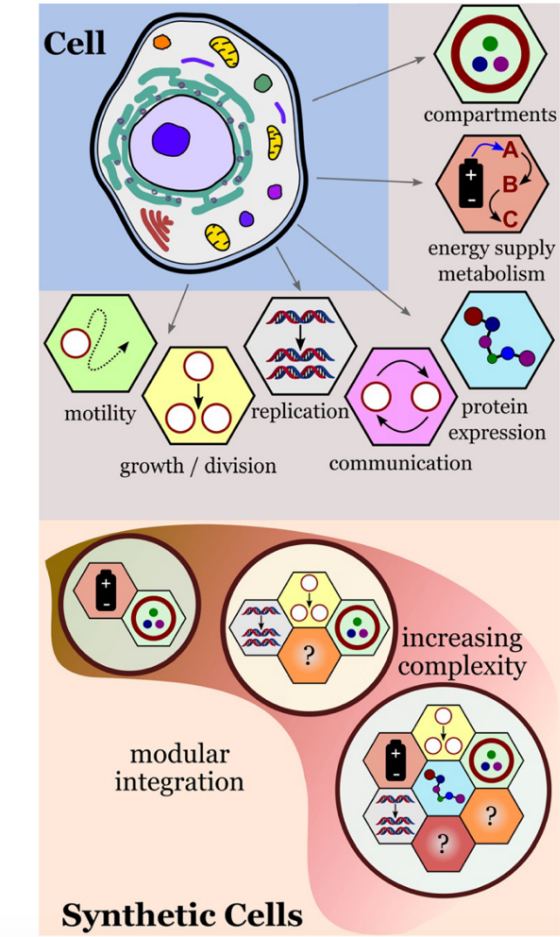

Figure 6: Modular approach for building synthetic cells with cell-like properties. The integration of functional modules creates synthetic cells with increasing complexity. Adapted from *[16]*

2. Membranebound multicompartmentalized systems

Compartmentalization is an essential feature of eukaryotic cells, as it provides the spatial organization of components for proper cell function. Indeed, the cell membrane and organelles are vital attributes necessary to store, protect and process molecular materials which drive the cell's integrity, maintenance, and reproduction.[16] Therefore, compartments not only serve as structural components of cells, they also play a key role in cellular functionality and behavior. In the late 50s, the very first man-made vesicles were successfully created by making a hemoglobin corpuscle of about 7 µm diameter with a thin and permeable collodion membrane.[18] Vesicles were defined as supramolecular self-assemblies of amphiphilic molecules arranged in a bilayer enclosing an

aqueous compartment.[43] From these findings, the concept of artificial cell was born. Subsequently, both single-layered and multi-layered lipid vesicles were used to enclose artificial intracellular components. Lipids, which are the primary constituents of biological membranes, possess amphiphilic properties that enable their spontaneous arrangement into a bilayer structure. Their polar headgroup is oriented towards the external aqueous environment while their hydrophobic tail forms the core of the membrane.[17] Lipid vesicles, commonly known as "liposomes," have long been the strategic choice for creating cell-like systems due to their resemblance to cellular membrane lipid compositions.[5,44] Nevertheless, liposomes have faced various challenges such as instability, sensitivity to the chemical composition of the surrounding medium, and a limited range of chemical functionalities. The emergence of polymer-based vesicles, also known as polymersomes, has provided valuable insights in the fields of biomimicry and nanomedicine.[45] Unlike their lipid counterparts, polymersomes offer enhanced robustness, stability and impermeability thanks to the higher molar masses and chemical tunability conferred by polymers.[5] These attributes have proved crucial to the development of targeted, controlled-release drug nanomedicines.[46–51] Polymersomes are capable of loading both hydrophilic and hydrophobic components, using their internal aqueous reservoir and thick membrane, respectively.[52] Furthermore, their surfaces can be functionalized to specifically target certain tissues or cells.[53] Polymersomes are similar to liposomes but also different in many ways, as reported by Rideau *et al*.[54] and Messager *et al*.[50] Because lipid and polymer materials have their own advantages and disadvantages, vesicles with mixed compositions have been made to exploit the favorable characteristics of the two components.[55–57] As the complexity of synthetic cells increases, so does the demand for multi-compartmentalized architectures that provide more sophisticated organizational and functional properties. These structures are achieved by the encapsulation of subcompartments into larger compartments. To construct these artificial cells, four main methods based on the self-assembly process of lipids and polymers can be used to obtain Giant Unilamellar Vesicles (GUVs): the gentle hydration method, the phase-transfer method, the electro-formation method, and the microfluidic method. In the following section, we will look in more detail at these different techniques, as well as at the latest advances in membranebound multicompartmentalized architectures.

2.1. Common techniques to construct artificial cells (from lipids/polymers)

2.1.1. Gentle Hydration Method

The gentle hydration method (Figure 7) was used in the formation of liposomes in the 1960s,[58] technique developed by Reeves *et al*.[59] Briefly, phospholipids or amphiphilic copolymers are dissolved in an organic solvent such as chloroform. As the solvent is furtherly evaporated until the sample is dry, a phospholipid or copolymer film is left within the glassware surface. The amphiphilic film is then hydrated by adding an aqueous solution like sucrose, and GUVs are formed from the surface. The gentle hydration method is simple, efficient, easy to perform, and has widely been used to produce artificial cells made from polymers and lipids.[60] However, this method has major drawbacks such as the formation of uneven GUVs in size, with a low control over the membrane structure (production of monolayered vesicles) and a poor and uneven loading efficiency when it comes to the introduction of enzymes and DNA for example, as they hinder the spontaneous expansion of the vesicle membrane.[61] In addition, previous studies have shown that it is difficult to obtain vesicles composed of lipid/copolymer mixtures using this method.[56]

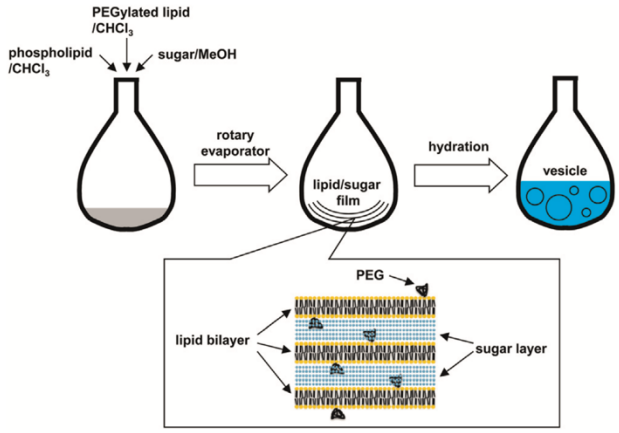

Figure 7: Outline of PEGylated lipid-and-sugar-doped gentle hydration.[61]

2.1.2. Electroformation Method

The electroformation method (Figure 8) was first reported in the 1980s by Angelova & Dimitrov.[62] The principles of the method are the same as the gentle hydration method, but here, amphiphiles are deposited onto an indium tin oxide (ITO)-coated glass. The expansion efficiency of GUV membranes can be improved by applying an alternating electric field current to the hydrated amphiphilic films.[54] Compared to the previous method, the electroformation method leads to a more uniform size distribution of GUVs, but other vesicles with different structures such as monolayer and multivesicular vesicles may be obtained at the same time. However, the main drawbacks of this method are a certain difficulty to produce GUVs from charged phospholipids as their surface charge affects the electric field applied on the electrode,[63] and the method can only form vesicles under physiological conditions at low ion concentration.[56] To solve these problems, the adjustment of the frequency and amplitude of the applied electric field are necessary.[64–66]

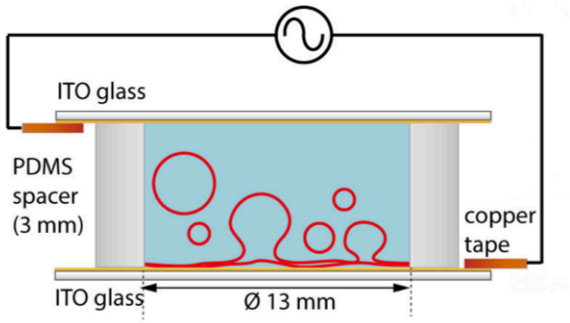

Figure 8: Schematic illustration of an ITO chamber. Two ITO coated glasses with conducting sides facing each other are separated by a spacer. Connecting the ITO layers via copper tape to a function generator leads to swelling of the GUVs.[67]

2.1.3. Phase Transfer Method

The phase transfer method (Figure 9) is another technique based on an emulsion system to build GUVs. Briefly, water droplets coated with a lipid or polymer monolayer are prepared. The droplets are then poured over a lipid or polymer-stabilized water/oil interface. The monolayer of the interface wraps the droplets to produce giant vesicles with a closed bilayer membrane structure.

Centrifugation[10,68] and micromanipulation[69] can also be used to improve the phase transfer efficiency. Different from the hydration and electroformation methods, the phase transfer technique can produce GUV membranes composed of two layers made from different materials. In addition, the vesicles have good stability and a regular shape. This method ensures the encapsulation of charged components as well as macromolecules and nanoparticles, which are loaded during the single-layer water/oil droplets. However, the size of the vesicles is quite dispersed, and the loading of the components not always uniform.[56]

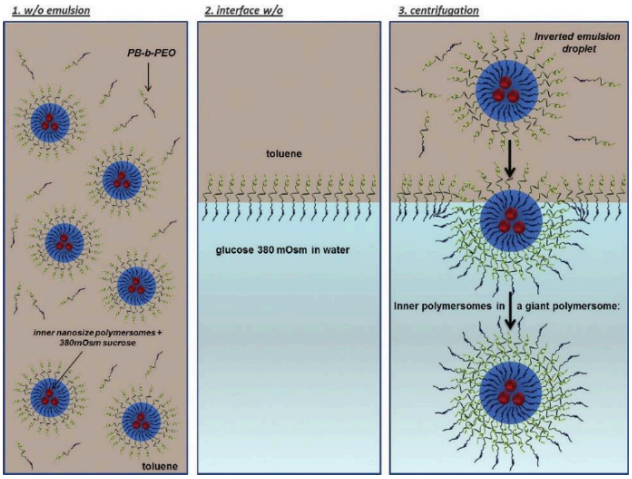

Figure 9: Biomimetic polymer vesicles: towards structural and functional cell biomimicry.[70]

2.1.4. Microfluidic Method

To improve the production efficiency of giant vesicles and accurately control their size and shape, researchers have developed a microfluidic technique based on the phase transfer, micro-jetting, or emulsification methods.[71,72] Briefly, the experiments consist in forming a series of droplets from water/oil/water (w/o/w) double emulsions. Giant vesicles assemble one by one in the microfluidic channel through the subsequent extraction of the middle oil phase.[73] Microfluidic devices are versatile platforms for miniaturizing and integrating fluid handling, sample preparation, analysis, and detection inside microchannels,[74,75] and have mainly been used to produce droplets,[76] microgels[77] and microspheres.[78] This technology has been explored in many disciplines such as chemistry,[79] bioscience,[80] pharmacy,[81] and has lately drawn significant attention in the

emerging field that are artificial cells.[82] Three mainstream devices exist for the fabrication of droplets including T-junction, flow-focusing and coflowing devices (Figure 10).[56] The latest, which has been used in this project, consists in injecting the dispersed phase in a central microchannel placed in the middle of another microchannel with a largest dimension. The dispersed phase becomes unstable and breaks up into droplets by Rayleigh-Plateau, and the formation of the droplet is dependent on the diameter of the microchannel containing the dispersed phase.[83–85] These microfluidic systems can be made from glass, polydimethylsiloxane (PDMS), polycarbonate (PC), poly(methyl methacrylate (PMMA), printed circuit board (PCD),[74] and can be assembled through different techniques like photolithography, maskless lithography, etching and soft lithography.[86] The main advantage of this technique is the ability to control the number and size of inner compartments by tuning the flow rate of the different phases and the diameter of the microcapillary. However, the drying process needed for solvent evaporation can lead to vesicle destabilization and involves traces of solvent left in the bilayer of the vesicles which is a major drawback for biomedical applications. In
Table 1, we summarize the advantages and drawbacks of each of the previously described methods to construct synthetic giant vesicles.

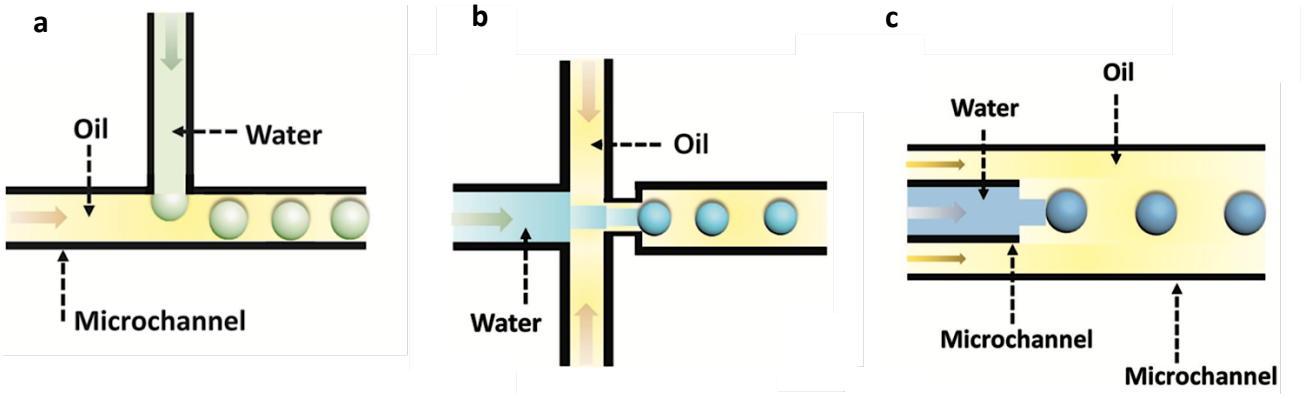

Figure 10: Fabrication of droplets by microfluidic devices: a) scheme illustration of T-junction b) flow focusing c) coflowing microfluidic devices.[74]

Table 1: Advantages and drawbacks of different methods for the construction of giant vesicles[56]

Methods	Advantages	Drawbacks
Gentle hydration method	Simple preparation and running	Low production rate Low encapsulation rate Inhomogeneous vesicle size
Electroformation method	Simple preparation and running Uniform size distribution of GUVs	Limitation to buffers with low ion concentrations Limitation on building materials (e.g., charged lipids)
Phase transfer method	Good vesicle stability Regular vesicle shape Asymmetric leaflet of vesicle composition	Difficult operation Inhomogeneous vesicle size and loading
Microfluidic method	Regular vesicle shape Uniform vesicle size and loading Asymmetric leaflet of vesicle composition	Arduous preparation of homemade chips Traces of solvent inhibits full formation of bilayer Limited vesicle size (dependent on the size of microfluidic channel)

2.2. Complex Cellular Structures Enclosed by Membranes

Artificial vesicles are simplified, well-defined and controllable versatile tools for the study of biological machinery of highly complex cells via a bottom-up approach.[87,88] The construction of cell-like mimics is not only to resemble appearances of cells, but also to imitate some of their functions. In the following paragraphs, we will review the recent works accomplished to produce membranebound multicompartmentalized structures.

2.2.1. Vesicle-in-Droplet

Droplets have a biological relevance as liquid structures are found in living cells in the form of P-granules, providing a means of compartmentalization in the cytoplasm through Liquid-Liquid Phase Separation (LLPS). Considering that life emerged from simple systems, droplets hold potential as pertinent models for studying fundamental principles of cellular organization. Also, because of the difficulties associated with producing lipid vesicles, researchers have explored the use of droplets for creating artificial cell systems. The use of microfluidics has notably allowed to create monodisperse droplets in the volume range of living cells (picolitres to nanoliters) as well as in large numbers, which is interesting for high analysis throughput.[89] Nuti *et al*.[90] have been producing multivesicular droplets (MVDs) to mimic the hierarchical build-up of cells (*Figure 11*), using a microfluidic system. Such method has the potential of spatiotemporally separating the enzymes and components in substructures, and allows selective and continuous release of chemicals to mimic processes like enzymatic reactions[91] and protein expression.[92] However, one major limit of this type of system is the complete consumption of the substrate, which brings the cascade reaction to an end.

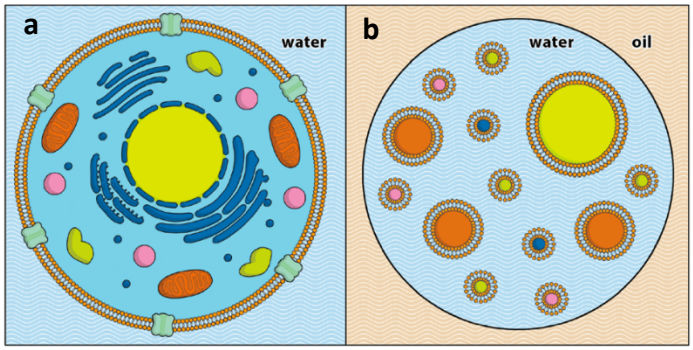

Figure 11: Schematic representation of a eukaryotic cell (a) next to a multivesicular droplet (MVD) (b). Droplet-based microfluidic techniques are used to encapsulate unilamellar lipid vesicles inside aqueous droplets, generating a hierarchical cell-like structure. Not to scale.[90]

To tackle this issue, Beyneton *et al.*[93] have developed a self-sustainable artificial cell to mimic the NADH reaction, an important process that occurs naturally in the body and plays a role in generating energy. To do so, they produced w/o droplets using a microfluidic setup, in which they have integrated a minimal metabolic reaction (Figure 12). The latter consists in the oxidation of D-glucose-6-phosphate 1 (G6P) by Glucose-6-phosphate dehydrogenase (G6PDH) into 6-phospho-D-glucono-1,5-lactone 2 (GLP), with the concomitant reduction of NAD+, which is here the substrate, into NADH. To have the self-sustained compartmentalized metabolism, Inverted Membrane Vesicles (IMVs) extracted from E. coli were inserted within the w/o droplet as functional microcompartments for the regeneration of NAD+ cofactor. Indeed, as NADH is produced by the enzymatic reaction, it is furtherly oxidized by the NADH dehydrogenase activity of the IMVs membrane, to re-obtain NAD+.

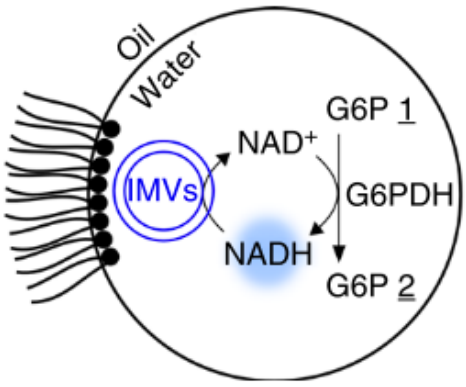

Figure 12: A graphic view of the self-sustained compartmentalized network.[93]

2.2.2. Vesicle-in-Vesicle

In comparison to droplets, vesicles are more challenging to produce. However, they offer closer resemblance to cells thanks to their semipermeable membranes, aqueous inner compartment, and three-dimensional structure. With their picoliter to nanoliter aqueous volumes that are enclosed within a phospholipid bilayer, liposomes stand out as the vesicles of choice and serve as ideal reaction vessels that emulate the cellular environment. In the following paragraphs, we will discuss the different structures and functionalities that have been developed to make multicompartmentalized vesosomes.

2.2.2.1. Liposome-in-liposome

Zasadzinski and coworkers[46] were among the first to introduce compartmentalized lipidic architectures called "vesosomes", with the idea of providing multifunctional drug delivery systems, with a high protection and control over the delivery of the drugs. These vesosomes consisted of small unilamellar liposomes entrapped within a larger liposome, known as liposomes-in-liposome. Briefly, negatively charged phosphatidylserine lipid bilayers were folded into cochleate cylinders upon complexation with calcium. Vesosomes were formed by unrolling the cylinders onto preformed liposomes via biotin-streptavidin interactions and modulation of calcium concentration with a chelating agent (Figure 13).[70]

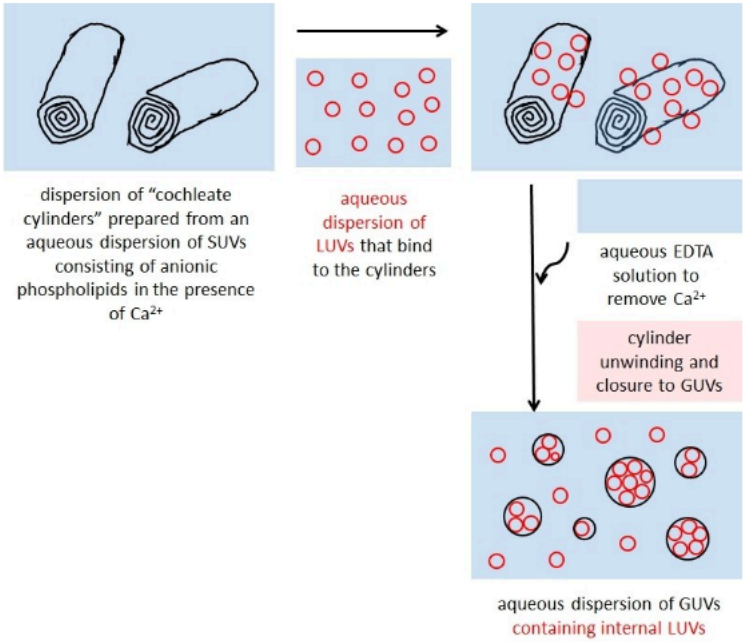

Figure 13: Schematic representation of the formation of an aqueous dispersion of multivesicular vesicle based on the transformation of rolled bilayers ("cochleate cylinders" into spherical vesicles. Separately prepared large unilamellar vesicles (in red) are entrapped inside the GUVs that form from the rolled bilayers (in black). Depending on the experimental conditions, non-entrapped vesicles will also be present. Therefore, depending on the application, free vesicles need to be removed, for example by repeated centrifugation.[94]

Following in Zasadzinki's footsteps, more and more liposome-in-liposome structures have emerged with various internal vesicles containing different types of reactive molecules. Many strategies have been developed to control in time and space the liberation of these chemicals and initiate the synthetic cell's activity. One of them consists in diffusing substrates of enzymatic reactions to induce the slow release of the reactive species from the internal vesicles to the aqueous pool of the outer vesicles, so the enzyme can catalyze and transform the reactive specie into a product. This was done by Li *et al.*,[95] who employed the thin film method to encapsulate glucose oxidase (GOx) within large 1,2-dipalmitoyl-sn-glycero-3-phosphocholine (DPPC) unilamellar vesicles (LUVs). The vesicles were subsequently trapped within lipid giant unilamellar vesicles (GUVs) using an electroformation process. Then, to encapsulate HRP and amplex red into the GUVs, an inward budding approach was used. Finally, to trigger the cascade reaction, the diffusion of glucose through protein pores like melittin initiated the cascade reactions.[95] In another experiment conducted by Hindley *et al.*,[26] 1,2dioleoyl-sn-glycero-3-

phophocholine:1,2-dioleoylsn-glycero-3-phophoglycerol (DOPC:DOPG) vesicles containing reconstituted mechanosensitive channels of large conductance (MscL) and calcein were embedded within 1-palmitoyl-2oleoyl-i-glycero-3-phosphocholine (POPC) GUVs, along with secretory phospholipase A2 enzyme (sPLA2) (
Figure 14A). sPLA2 is a calcium (Ca^{2+}) dependent enzyme. As Ca^{2+} diffuses through α-hemolysin (α-HL) pores of the GUVs, the sPLA2 is activated and catalyzes phosphatidylcholine lipids to lyso-phosphatidylcholine (LPC) (
Figure 14B). The production of LPC on the leaflet of the inner vesicles leads to an asymmetrical change in the lateral pressure profile of the membrane. This change is detected by the mechanosensitive MscL membrane protein that responds to changes in membrane mechanics by opening large, nonspecific pores with a diameter of approximately 2.5–3 nm (
Figure 14C). Consequently, molecules of up to 10 kDa in size like calcein are released. The response of MscL to sPLA2 can be viewed as a protein-protein interaction through inner lipid membranes, controlling the fluorescence behaviour of an artificial cell.

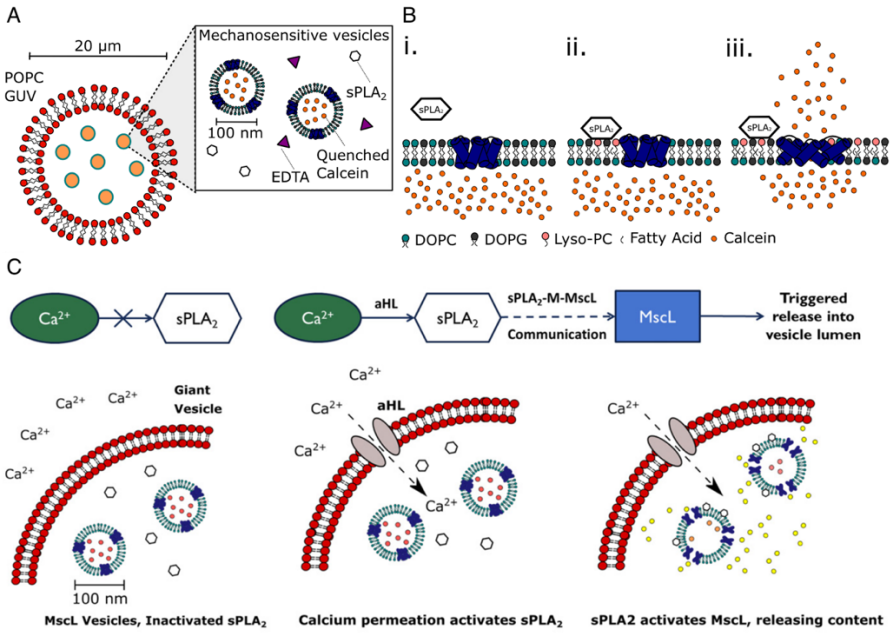

Figure 14: Using the sPLA2–membrane(M)–MscL network to build a synthetic mechanosensitive signaling pathway inside an artificial cell (AC). (A) Composition of the nested AC: A microscale POPC membrane encloses 1:1 DOPC:DOPG vesicles containing reconstituted mechanosensitive channel of large conductance (MscL), secretory phospholipase A2 (sPLA2) enzyme, and EDTA to

chelate trace calcium present in the AC. (B) Function of the sPLA2–M–MscL network. (B, i) MscL is reconstituted into a DOPC:DOPG membrane and is closed in the absence of tension or asymmetry in the membrane. sPLA2 is added to the solution. (B, ii)sPLA2 binds to the membrane and begins to catalyze the production of LPC and a concomitant fatty acid. The asymmetric generation of LPC begins to asymmetrically change the pressure profile of the lipid bilayer. (B, iii) Once a critical amount of LPC has been produced, MscL responds to the lateral pressure change by opening to form a 3- to 4-nm diameter pore in the lipid bilayer, releasing encapsulated cargo across the membrane. (C) Proposed functioning of the synthetic mechanosensitive signaling pathway. Ca2+ is prevented from entering the nested vesicle due to the presence of the outer POPC membrane. Permeabilization of the outer membrane (here accomplished with αHL) then results in a calcium influx, activating latent sPLA2 in the vesicle lumen. This activates the sPLA2–M–MscL network, resulting in content release (and potentially the control of downstream events) within the AC.[26]

Other than the diffusion of substrates, the release of the vesicles content can also be controlled by varying and tunning the chemical structure of the amphiphiles composing the internal vesicle membranes, thus the membrane properties, upon a specific stimulus. This was for example realized by Suzuki *et al*.,[96] who constructed a liposome-in-liposome system, in which the inner liposome encapsulated double-stranded DNA (dsDNA), and their membrane contained a photosensitive group, here photo-labile caged phospholipid 2. A fluorescent probe SYBR Green I was present in the core of the outer liposome. Upon UV irradiation, the phospholipid membrane of the inner liposome became porous, through which the dsDNA could pass and form a fluorescent intercalation complex with the SYBR Green I. In a related example, Hindley *et al*.[97] incorporated diacetylene functional groups within their lipid systems which upon irradiation, lead to cross-linking and pore formation. Their system consisted in vesicles-in-vesicles, where the sub compartments encapsulated fluorescein di-β-D-galactopyranoside (FDG) substrate, and the enzyme β-galactosidase (β-gal) dispersed within the main vesicle core. Upon UV irradiation, photopolymerisation of the inner membrane compartments resulted in FDG release, leading to its catalysis by β-galactosidase forming free fluorescein (Figure 15).

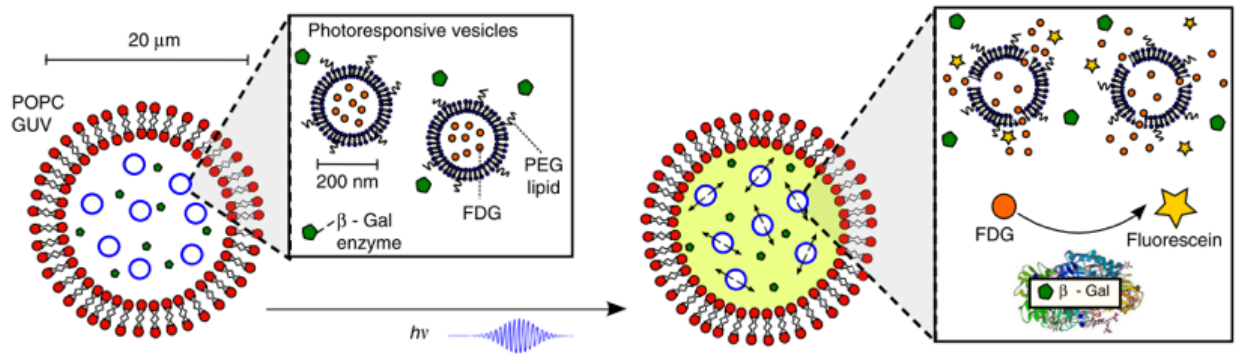

Figure 15: Cartoon of UV-responsive nested vesicle mechanism. Photo-responsive vesicles and the enzyme β-galactosidase are co-encapsulated within POPC GUVs created via phase-transfer. Upon illumination with UV-C, photopolymerization of the inner compartment membranes results in FDG release, leading to its catalysis by β-galactosidase forming free fluorescein.[97]

An important step to furtherly resemble cell's intrinsic function has been to develop artificial cells capable of producing the most essential features of a cell, adenosine triphosphate (ATP), the energy source for all biological processes. This level of structural organization and functionality shows high similarities to chloroplasts in cells. Lee *et al*.[98] developed photosynthetic liposomes with two types of membrane-embedded photoconverters: a plant derived photosystem II(PSII) and a bacteria-derived proteorhodopsin (PR) (Figure 16a). Encapsulation of the photosynthetic liposomes into larger liposomes resulted in light-responsive synthetic cells able to produce their own ATP using light as an energy source. On the one hand, exposing the synthetic cells to green light suspended the proton generation by PSII, and impeded the ATP synthesis as PR pumped the protons outside of the GUV. On the other hand, exposing the synthetic cells to red light activated the electron transport chain by PSII, thereby establishing a transmembrane proton gradient between the interior of the synthetic organelle and the interior of the giant vesicle. Like in cells, the proton gradient was used to generate ATP from Adenosine Diphosphate (ADP) (Figure 16b). Finally, to simulate a ubiquitous process in cells which is the cytoskeleton formation, the ATP-dependent polymerization of actin filaments was triggered by red light activation of the artificial organelles. The polymerization of actin monomers can regulate the morphology and motility of living cells, and herein deformed the spherical membrane system into mushroom shape via heterogeneous membrane–actin interactions (Figure 16c).

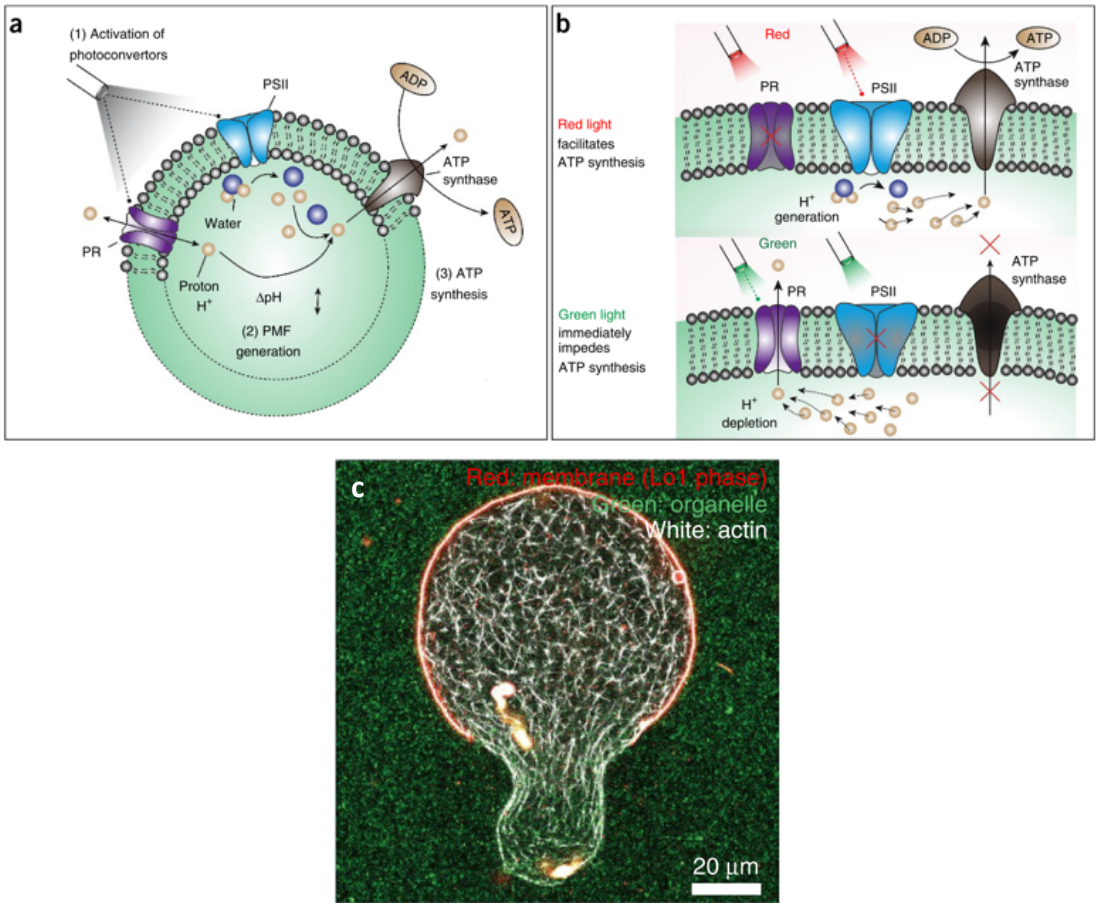

Figure 16: Design and applications of the photosynthetic artificial organelle. (a) Upon optical stimulation, the artificial organelle synthesizes ATP by the coordinated activation of two complementary photoconverters (PSII and PR) and an ATP synthase reconstituted into the organelle's membrane. (b) Activation of PSII with red light facilitates ATP synthesis by generating protons inside the organelle, while activation of PR with green light impedes ATP synthesis by depleting protons. (c) Actin polymerization deformed the spherical membrane system into mushroom shape via heterogeneous membrane–actin interactions.[98]

Another example is the work of Berhanu *et al*.,[99] who produced GUVs containing a cell-free protein synthesis system and small proteoliposomes, which consist of purified ATP synthase and bacteriorhodopsin. The ATP produced by light inside the GUVs by the internal proteoliposomes served as substrate and energy source for the synthesis of the proteins of the internal proteoliposomes, as seen in the chemical reaction of Figure 17.

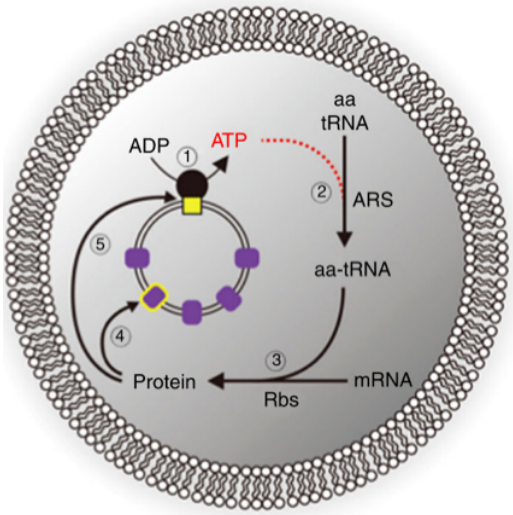

Figure 17: Self-constituting protein synthesis in artificial photosynthetic cells. a Schematics of self-constituting protein synthesis. The numbers indicate the order of reactions; ①: adenosine triphosphate (ATP) synthesis, ②: aminoacylation of transfer RNA (tRNA) by aminoacyl-tRNA synthetase (ARS), ③: translation by ribosomes (Rbs), ④: de novo bacteriorhodopsin (bR) synthesis, and ⑤: de novo Fo synthesis.[99]

In the continuity of mimicking eukaryotic cells and developing complex cell-like systems, Zong *et al*.[100] were able to mimic DNA replication and cell division using liposome-in-liposome structures (Figure 18). The inner liposome was formed by the invagination of the liposome following a hypertonic shock. Through this process, the inner content of the liposome was loaded with DNA. A polymerase chain reaction was then used to amplify the amount of DNA within the inner vesicle. An osmotic stress was furtherly applied to induce the separation of the mother cell into two daughter cells, each of them containing the inner vesicle with the DNA content of the mother cell.

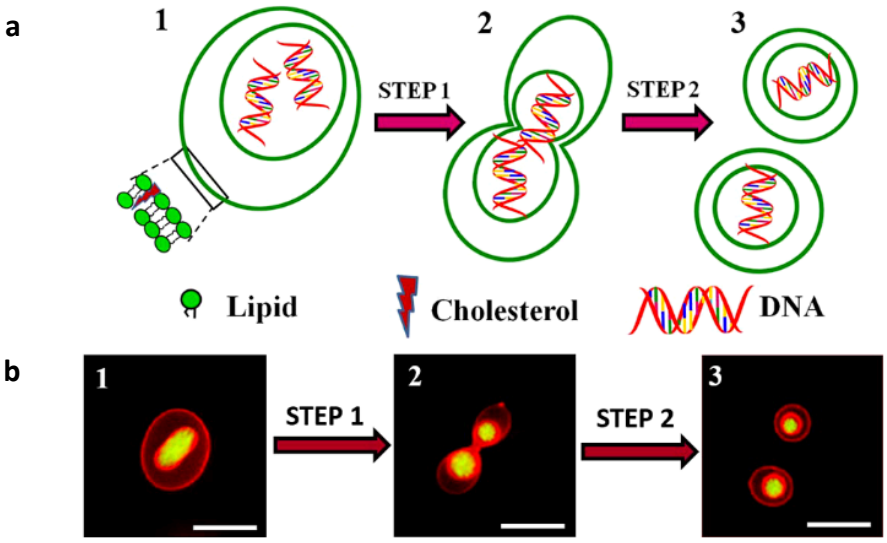

Figure 18: (a) Schematic illustration of the fission process of a DNA-amplified VIV. (b) Fluorescence images of a single VIV at rest (1), elongated (2), and the resulting two daughter VIVs containing amplified DNA molecules inside their respective IV (3). The lipid bilayer was labelled with 1 mol% Texas Red® DHPE (red fluorescence) and DNA molecules were labelled with SYBR Green I (green fluorescence). The scale bar in (b) is 20 µm. [100]

Most of the methods discussed in **2.1.** and used in the previously described examples often produce polydisperse populations of vesicles. To achieve precise and controlled nested liposomal structures, termed vesosomes, with specific sizes and configurations, a microfluidic setup was used by Deng *et al.*[8] They utilized a surfactant-assisted microfluidic strategy to create monodisperse liposomes from water-in-oil-in-water (W/O/W) double emulsion droplets. Specifically, they encapsulated multiple types of liposomes as the inner phase by using a two-inlet channel, offering a wide range of possibilities (Figure 19a,b). After undergoing dewetting, these liposomes were reintroduced as the inner phase into the microfluidic devices, forming larger liposome-loaded W/O/W emulsion droplets (Figure 19c). A second dewetting transition led to the formation of uniform liposome-in-liposome vesicles, with the initially injected liposome acting as the nuclei (Figure 19d). Then, to mimic the key function of the nuclei, an in vitro transcription (IVTx) mix and RNA detector, which is fluorescent only when bound to RNA, were encapsulated within the single liposomes. The increase in fluorescence due to the production of RNA was tracked over time. The transfer of molecules between compartments was also explored: melittin pores and calcein were encapsulated into the inner vesicles. The oligopeptide self-assembled into the

vesicles' bilayers, forming pores of 1 to 3 nm or 3.5 to 4.5 nm, depending on the number of assembling units, so that calcein diffused out of the inner vesicles, a process that could be followed over time. This work successfully demonstrated that the generation of liposome-in-liposome in a highly reproducible manner is possible and they can be used as models for artificial cell-like systems. Overall, all these systems described give high spatiotemporal levels of control over the mixing of different encapsulated components of the microreactor and serve as important hierarchical reaction compartment models with the aim of mimicking some features of the structural and functional complexity of eukaryotic cells.

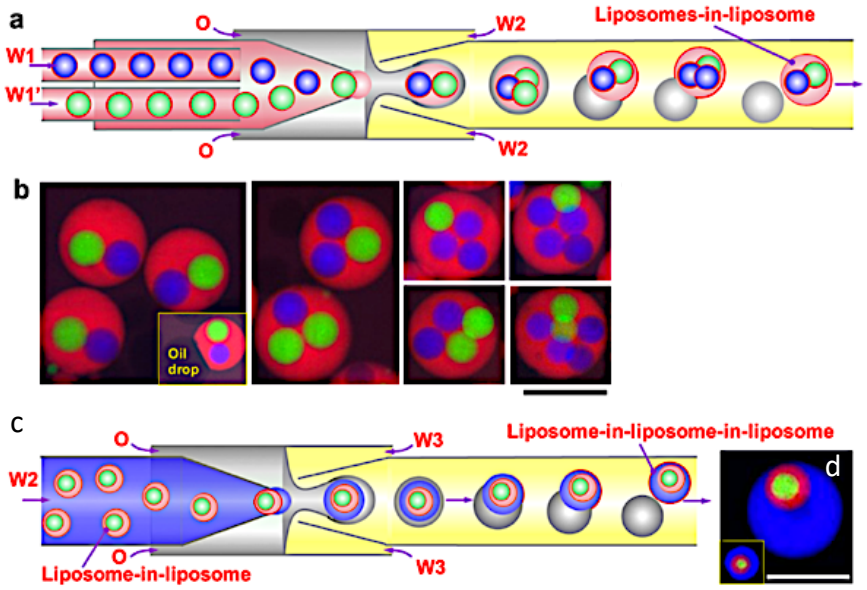

Figure 19: (a) Schematic illustration of the microfluidic preparation of double emulsions with distinct interior liposomes and the dewetting process. (b) Confocal images of the vesosomes with different numbers and ratios of interior liposomes. (c,d) Schematic and confocal images show the formation of triple vesosomes and the resultant structures. Scale bars, 100 µm.[8]

2.2.2.2. Polymersome-in-polymersome

Following this, the first multicompartmentalized system based on polymers was described by Chern and coworkers[101] in 2008, who used a water-in-oil-in-water double emulsion technique to make polymersome-in-polymersome. They used a poly(acrylic acid)-*b*-poly(distearin acrylate) (PAA-*b*-PDSA) copolymer to form a first set of polymersomes. They were furtherly encapsulated in larger polymersomes as the inner phase of a subsequent w/o/w double emulsion preparation. The pH responsiveness of the acrylic acid allowed them to reversibly tune the permeability of their polymersome membrane, to control the diffusion of trapped molecules. Weitz and coworkers[102] elaborated the system by coupling microfluidics to the double emulsion technique to improve size control and reproducibility over the vesicles. In 2012, Marguet *et al.*[103] encapsulated doxorubicin (DOX) drug in poly(trimethylene carbonate)-*b*-poly(L-glutamic acid) (PTMC-*b*-PGA) polymersomes, formed by nanoprecipitation, within larger poly(butadiene)-*b*-poly(ethylene oxide) (PB-*b*-PEO), formed by emulsion centrifugation. To control and follow up the release of the drug, a tailor-made drug release device inspired by Franz cells was used. Later on, Peters *et al.*[10] developed a multi-compartmentalized polymersome system that shows both structural and functional similarities to a eukaryotic cell. Authors investigated the effects of multi-compartmentalization and functional control on a multistep reaction pathway in polymersomes-in-polymersomes systems, as seen in Figure 20. Briefly, phenylacetone monooxygenase (PAMO) was used to oxidize a ketone into an ester, and the ester was subsequently hydrolyzed by a lipase, candida antarctica lipase B (CalB). The resulting hydroxy-functional profluorescent compound was oxidized by alcohol dehydrogenase (ADH), which led to the formation of a fluorescent product. The artificial organelles were made out of intrinsically permeable polystyrene-*b*-poly(3-(isocyano-lalanyl-amino-ethyl)-thiophene) (PS-*b*-PIAT) polymersomes. CalB and ADH were encapsulated in these nanoreactors, and these were loaded together with PAMO and the reagents into micrometre-sized PB-*b*-PEO polymersomes. The validity of the three-enzyme cascade was first tested without the encapsulation in the PB-*b*-PEO polymersomes, with either all enzymes in solution or with CalB and ADH enzymes encapsulated in PS-*b*-PIAT nanoreactors. When CalB was replaced by alcalase, a protease, the activity of the free three-enzyme cascade was considerably decreased due to the proteolytic effect of alcalase on the free enzymes. When alcalase

was encapsulated in PS-*b*-PIAT nanoreactors, the physical separation ensured a more efficient conversion.

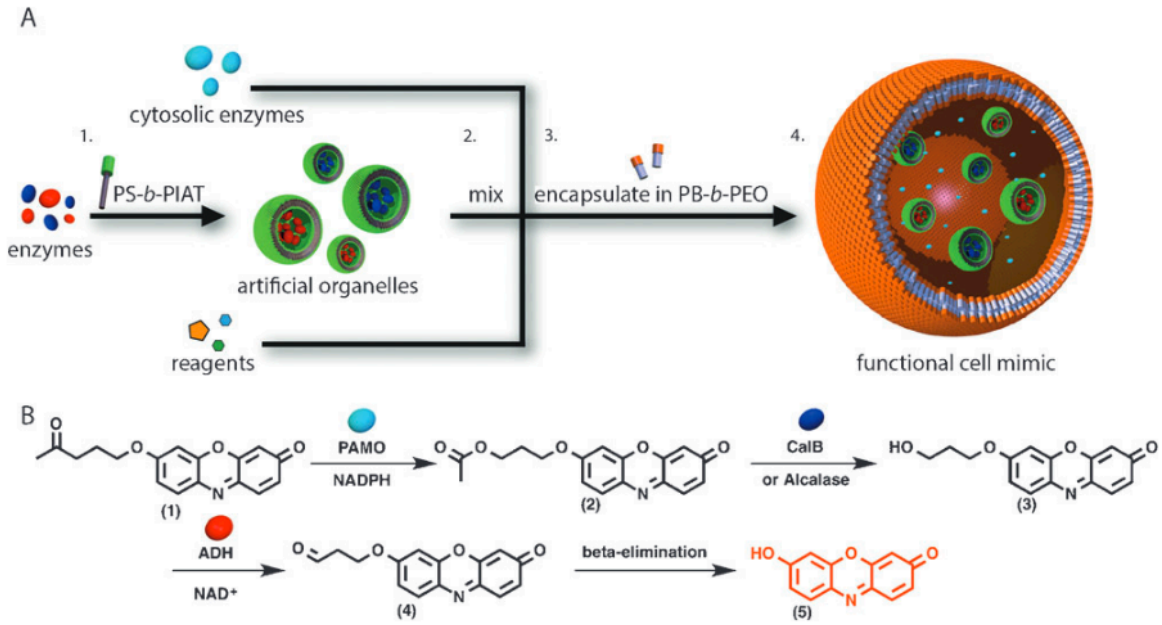

Figure 20: A) The concept of the cell mimic, which shows the initial encapsulation of different enzymes in polystyrene-b-poly(3-(isocyano-lalanyl-amino-ethyl)-thiophene) (PS-b-PIAT) nanoreactors (1), followed by mixing of the organelle mimics, cytosolic enzymes, and reagents (2), before encapsulation of the reaction mixture in polybutadiene-bpoly(ethylene oxide) (PB-b-PEO) vesicles (3) to create the functional cell mimic (4), inside which enzymatic multicompartment catalysis takes place. B) Detailed cascade reaction scheme. Profluorescent substrate 1 undergoes a Baeyer–Villiger reaction catalyzed by phenylacetone monooxygenase (PAMO), with one unit of the reduced form of nicotinamide adenine dinucleotide phosphate (NADPH) being consumed, to yield ester 2, which is subsequently hydrolyzed by Candida antarctica lipase B (CalB) or alcalase to provide primary alcohol 3. Alcohol dehydrogenase (ADH) oxidizes the alcohol, by using the cofactor nicotinamide adenine dinucleotide (NAD+), to give aldehyde 4, which then undergoes spontaneous beta-elimination to yield resorufin (5) as the final fluorescent product.[10]

In another example, Thamboo *et al.*[104] created a self-assembled vesicular multicompartment system in which complex signal transduction was achieved via a cascade reaction involving two different types of artificial organelles. These systems contained structurally different compartments, which were composed of a polymeric membrane (giant unilamellar vesicle (GUV)) encapsulating artificial organelles consisting of a mixture of $PMOXA_5$-*b*-$PDMS_{58}$-*b*-$PMOXA_5$ and $PDMS_{65}$-*b*-heparin copolymers. The lipase substrate 1,2-Di-O-lauryl-*rac*-*glycero*-3-(glutaric

acid 6-methylresorufin ester) (DGGR) was incorporated in the stimuli-responsive artificial organelle (NPGraft) based on the graft copolymer (poly(2-methyl-2-oxazoline)$_{88}$-*graft*(SS)-poly(ε-caprolactone)$_{238}$ (PMOXA$_{88}$-*g*(SS)-PCL$_{238}$), and the lipase enzyme was entrapped in the secondary artificial organelles (LipVes). Then, these two kinds of artificial organelles were loaded into GUVs, which formed a stimuli-responsive multicompartment system. Fluorescence was not observed in a non-reductive environment, but DGGR was released from the subcompartment NP-graft under reductive conditions and interacted freely with enzymes in LipVes forming the fluorescent product after adding the signalling molecule dithiothreitol (DTT) to the GUVs. The lipase reaction was successfully triggered via the signal transduction between two types of artificial organelles within a giant vesicle with multiple internal subcompartments.

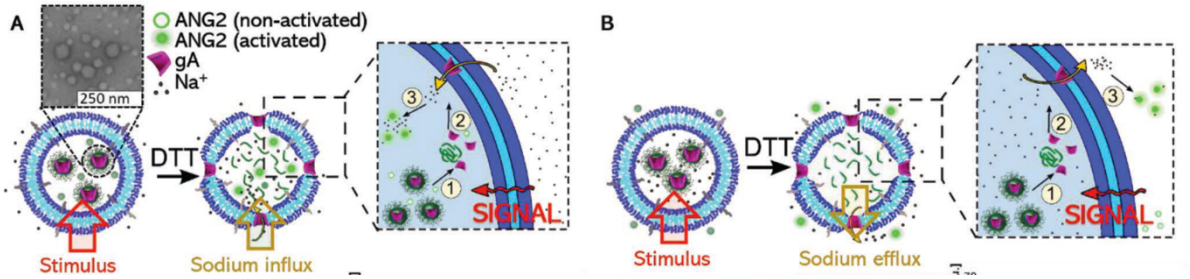

Figure 21: Triggered gramicidin (gA) ion channel recruitment from internal subcompartments to the polymer membrane of a multicompartment using CLSM imaging. A) Schematic representation of gA mediated import of sodium ions. Upon the addition of DTT, encapsulated gA is released from its NP-Graft and inserts into the GUV membrane boundary. This allows sodium ions from the outside to enter the GUV cavity where they activate the sodium sensitive dye ANG2. B) Schematic representation of gA mediated efflux of sodium ions from the GUV cavity. DTT induced gA permeabilization of the GUV membrane, allows sodium ions in the interior to exit the vesicle and activate the ANG2 in the surrounding environment of the multicompartment.[104]

These examples of multi-compartment systems are effective mimics of natural cells reaction pathway, and represent an invaluable technique for increasing complexity in polymersome-based protocells. It is indeed possible to envisage ever more complex and autonomous behaviour with such control over the spatial orientation of enzymes and substrate.[105]

2.2.2.3. Hybrid systems

Finally, hybrid multicompartmentalized systems were first reported by McPhail *et al.*,[106] where liposomes were encapsulated within a 2:1 weight ratio of polymer palmitoyl glycol chitosan and cholesterol outer vesicle. These hybrid lipid-polymer vesicles combined the properties of polymersomes, which have a low permeability and are versatile, to the ones of liposomes like biocompatibility and biological functionality.[107] In 2017, Peyret *et al.*[9] prepared liposomes from 1,2-dipentadecanoyl-sn-glycero-3-phosphocholine (diC15-PC) and 1,2-dipalmitoyl-sn-glycero-3-phosphocholine (DPPC), using a thin-film technique to make the inner compartment of their artificial cells. The liposomes were then encapsulated within giant poly(butadiene)-*b*-poly(ethylene oxide) (PBut-*b*-PEO) polymersomes through an emulsion-centrifugation method. As the experimental temperature was controlled, it could either be set above or below the lipid phase transition temperature (T_m). DPPC exhibited a T_m of 41°C, whilst the T_m of diC15-PC was of 35°C. Raising the temperature above the T_m of each respective liposomes caused their membrane to transition from a gel phase to a fluid phase, resulting in dye release due to membrane permeabilization (Figure 22). This controlled release can be employed to trigger cascade reactions in confined microreactors as needed.

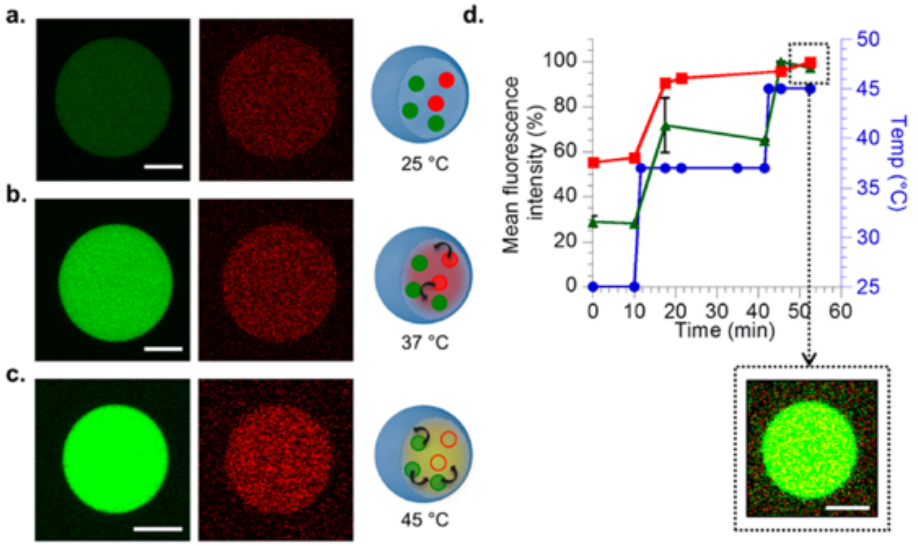

Figure 22: Co-loading of MB-loaded diC15-PC liposomes and fluorescein-loaded DPPC liposomes into giant PBut-b-PEO polymersomes and successive temperature-triggered dye

release: (a) 25 °C, T = 0 min, (b) 37 °C, T = 25 min, and (c) 45 °C, T = 10 min. Left column: emission of fluorescein, right: emission of methylene blue. Scale bar = 10 μm.[9]

2.2.3. Vesicle-in-Coacervate

Coacervates (which are defined as condensed liquid-like droplets formed by liquid-liquid phase separation (LLPS) of molecules through multiple weak associative interactions[108]) and lipid vesicles are complementary in many aspects. While the coacervation process can efficiently concentrate molecules like enzymes but cannot sustain electrochemical gradients, vesicles on the other hand are physically defined, but they generally cannot concentrate essential molecules.[109] Therefore, the co-assembly of coacervates and vesicles is a promising route to construct more complete systems. To understand what principles lie behind such interactions and uptakes of vesicles by coacervates, Lin *et al*.[110] conducted a study to observe how different types of liposomes were assimilated and sequestered by single-stranded oligonucleotides and poly(L-lysine) coacervates. The liposomes were prepared using film hydration or microfluidic techniques. The primary driving force behind this uptake is electrostatic attraction, as the coacervate droplet exhibits varying affinities depending on the charges of the liposomes. In addition, under the influence of an electric field, the composite coacervates undergo internal fusion, redistribution of components, and may even release daughter cells with a similar composition, depending on the original structure and the types of liposomes used. The liposomes can either coat the surface of the droplet, unevenly distribute as fibrous structures, or evenly distribute inside the coacervate droplet. Incorporating liposomes into the composite droplet introduces new dynamic features that can be manipulated by applying an electric field. These electrostatic interactions also occurred in Mason *et al*.[111] experiments, who produced semipermeable poly(ethylene glycol)-*b*-poly-(caprolactone-gradient-trimethylene carbonate) (PEG_{22}-*b*-PCL_{38}g$PTMC_{32}$) polymersomes, loaded with enzymatic cargo, through the hydration method (Figure 23). The polymersomes were spontaneously uptaken by cell-sized coacervates, in a process comparable to protocellular endosymbiosis. Due to their low structural stability in time, the coacervates were coated using a terpolymer comprising poly(ethylene glycol), poly(caprolactone-gradient-trimethylene carbonate) and poly(glutamic acid) (PEG-*b*-PCL*g*PTMC-*b*-PGA), strategy developed in one of their previous works.[112] This hybrid system integrates several attributes of eukaryotic cells such as crowdedness,

hierarchical structure, spatial organization of enzymes, and compatibility with cellular media. Notably, it gives a broader understanding of the importance of compartmentalization in cells and their activity, as compartmentalization creates favorable microenvironments for enzymatic reactions whilst segregating and protecting incompatible components, mimicking localization of proteases into lysosomal organelles.

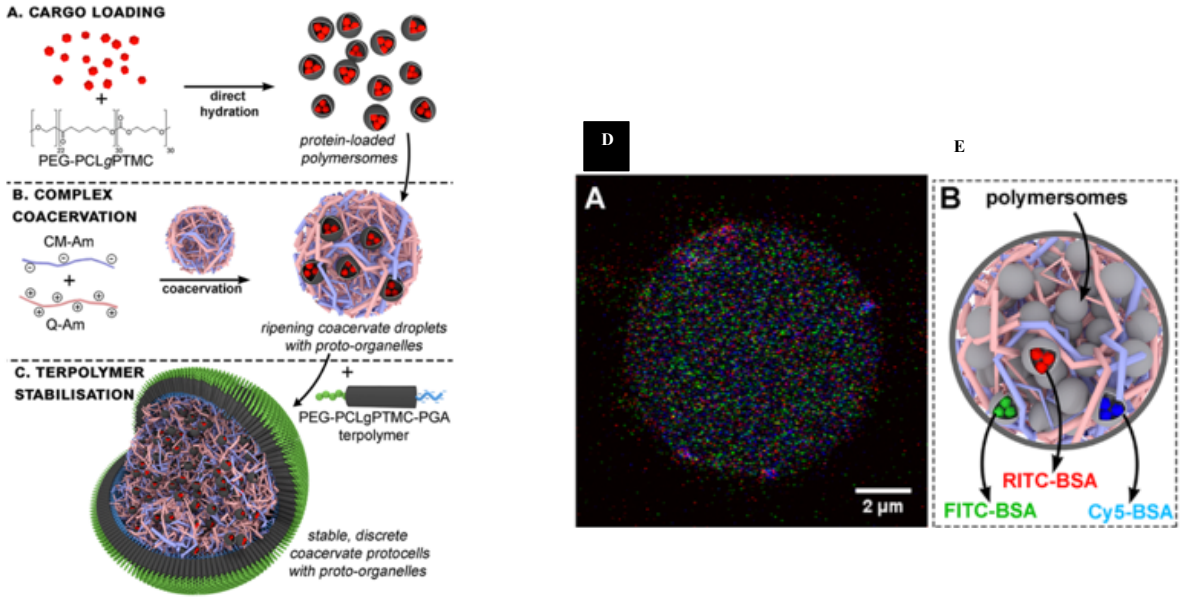

Figure 23: Formation of a hierarchical protocell through the spontaneous sequestration of polymersomal protoorganelles by a coacervate microdroplet (a) subsequent membranization with a synthetic terpolymer (b) provides stability to the overall construct, which was evaluated to demonstrate the advantageous properties of a spatially organized, subcompartmentalized system (c) that mimics the advanced properties of a eukaryotic cell (d) confocal micrograph of multicompartmentalized protocell (containing FITC-, RITC-, and Cy5-labeled succinylated bovine serum albumin (BSA) in separate vesicles) encapsulated within membranized coacervate protocells depicted in (e), which is not drawn to scale. [111]

3. New phase of multicompartmental systems – LLPS in artificial cells

As explained earlier, one of the main features of biological evolution at the cellular level is compartmentalization,[2,3,15,20,113] as it has most likely played an important role in bringing together the chemical blocks of life diluted in primordial ponds. In this next part of the state of the art, we will focus on membraneless organelles, which are compartments devoid of any surrounding membrane, facilitating their numerous exchanges with the cytoplasm. However, some fundamental questions remain unanswered: how do these systems concentrate molecules, maintain and regulate their structures, control their compositions, and modulate internal biochemical activities?[114,115] More and more, Liquid-Liquid Phase Separation (LLPS) is seen as the mechanism to explain the formation and function of membraneless organelles.[114,116] In 1899, Edmund Wilsonin first proposed that the cytoplasm of cells resembled and behaved like a mixture of different chemically suspended drops.[117] The discovery in 2009 of Brangwynne and coworkers on the existence of P bodies[118] and their liquid-like behaviours including fusion, dripping and wetting, has led to increasing attention to these particular types of membraneless organelles. Their formation is driven by rapid condensation and dissolution of various proteins and RNAs. From these findings, researchers started to understand that the organization of multiple membraneless organelles might rely on LLPS and reversible micro-comparmentalization of biomolecules within the aqueous lumen of cells, resulting in important cell structures and functions.[119] Similar droplet-like behaviours were furtherly observed in the assembly of other membraneless structures such as the nucleus in 2011[120] and the cytoplasm.[11,121] In 2012, Michael Rosen and coworkers[122] found that the interactions of multivalent proteins underwent a rapid phase transition from small complexes to large polymeric assemblies, as proteins highly concentrated. This phenomenon is accompanied by a macroscopic LLPS. In the same year, Steven McKnight and colleagues showed that LLPS determined the architecture of RNA granules in a cell-free in vitro reaction.[123] Since these discoveries, the LLPS field of research has widely expanded. However, it is still not yet clear why and how these structures are formed, what forces govern their assembly and how their physical characteristics contribute to biological functions,[124] but as research progresses, some of these answers are slowly beginning to be unveiled. It has, for example, been observed that a disturbance in the LLPS of proteins can create clogs or aggregates of molecules that form at the wrong time or place, and could be linked to neurodegenerative diseases, viral infections, cancers,

and age-related disorders.[119,125–128] Indeed, protein phase separation is suspected of causing cancer when mutated, as the droplets no longer form instead of sequestering and destroying cancer cells.[129]

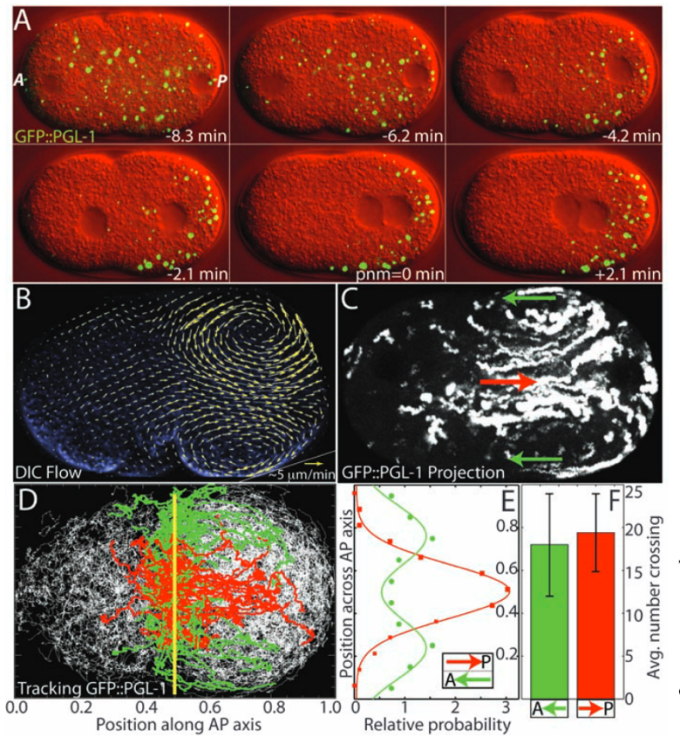

Figure 24: P granule localization is not due to cytoplasmic flow. (A) Fluorescent images of GFP::PGL-1 (green) superimposed on differential interference contrast (DIC) (red). Time relative to pronuclear meeting (pnm). A, anterior; P, posterior. (B and C) The movement of P granules is similar to the movement of yolk granules. (B) Cytoplasmic flow field from PIV analysis of a single embryo (blue DIC image) during symmetry breaking. Yellow arrows indicate flow direction and magnitude. (C) Maximum-intensity projection of confocal stacks of GFP::PGL-1 P granules in the one-cell embryo during symmetry breaking; first frame, –8min,7spnm;last frame, –3min,30spnm;Pgranulesincenterofembryo move posteriorly (red arrow), and P granules near cortex move anteriorly (green arrows). (D)Overlay of P granule trajectories (white) from five GFP::PGL-1 embryos. Trajectories crossing into the posterior are shown in red, and those crossing into the anterior are in green. (E) Probability distribution of the location perpendicular to the AP axis of P granules crossing the midpoint [yellow line in (D)] into anterior (green) versus posterior (red). (F) The average flux per embryo (mean T SEM, n = 5) indicates negligible net flux.[118]

3.1. Types of Liquid-Liquid Phase Separation

Most membraneless organelles found in Nature form through the LLPS of proteins and RNA, related to cellular structural organization and functions.[130,131] These types of organelles allow more dynamic and easier exchanges with their environment thanks to their lack of membrane, capable of selective sequestration of biomolecules and catalytic activity.[132] From a thermodynamics viewpoint, three types of LLPS are commonly distinguished: segregative, associative and simple phase separation (Figure 25a), driven by basic forces.

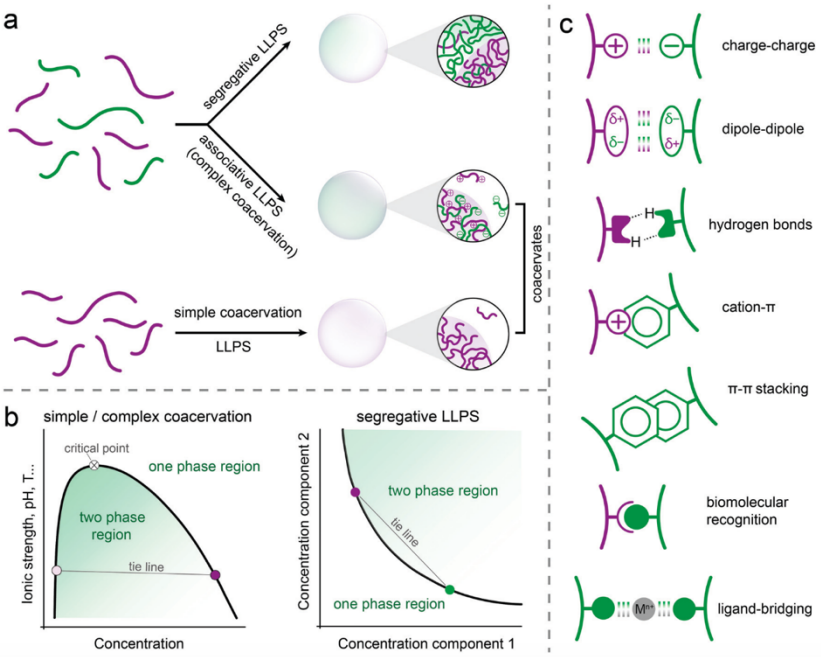

Figure 25: (a) Types of liquid–liquid phase separation and the formation of coacervates, (b) schematic phase diagrams of simple or complex coacervation and segregative phase separation, (c) possible interactions involved in the formation of peptide-based coacervates.[108]

The segregative phase separation of two soluble molecules such as peptides, polymers, or nucleotides, results in their phase separation into two isotropic solutions due to repulsive interactions between the compounds, despite favourable mixing entropy.[108] Each formed phase is enriched in one or the other molecule. Poly(ethylene glycol) (PEG) and dextran are commonly used as a polymer-polymer based aqueous two-phase system (ATPS) pairs, but polymer-salt systems like PEG with citrate, phosphate, or sulphate, have also been reported in the literature.[133]

The phase separation can be induced by controlling the temperature and/or the molecular weights and concentrations of the two components. To predict the occurrence of the phase separation and the composition of each phase, phase diagrams are used (Figure 25b). They are constructed by preparing solutions with varying compound concentrations and reporting their mixed or unmixed state after equilibration. The binodal, the boundary between these two regions, is then traced as the line that separates the one- and two-phase regions. At low polymer concentrations, below the binodal curve, the two polymers form a one-phase system. When shifting to higher polymer concentrations, above the binodal curve, demixing between the two polymers occurs, forming a two-phase system. The phenomenon can be described in terms of the Flory-Huggins[134–137] theory, which describes the polymer-polymer net repulsions and the polymer-solvent interactions[135] that drive the phase separation (Figure 25c). Keating and coworkers are one of the leading groups in this field of research.[138–141]

The associative phase separation consists in the formation of a dense polymer-rich phase, the coacervate, and a dilute polymer-poor phase.[142] Two types of associative coacervation exist, namely the complex and simple coacervation (Figure 25a). Complex coacervation was first reported by Tiebackx,[132] and subsequently investigated by Bungenberg de Jong and Kruyt in 1929 by mixing gelatin (polycation) and gum Arabic (polyanion).[143] Oparin's work later used complex coacervate droplets as primary metabolic cell models to study the origins of life due to their cell-like microcompartmentalization.[1] Complex coacervation[108,142,144,145] describes the phase separation occurring due to attractive electrostatic interactions of two oppositely charged polyelectrolytes, to form a dense, polyelectrolyte-rich phase (coacervate) and a more dilute solution.[146–148] Countless complex coacervate systems have been reported, which can be made of natural compounds (oligonucleotides,[149] oligopeptides,[150] proteins,[151] peptides,[152,153] small molecules,[154]) or synthetic polymers (modified polysaccharides, polypeptides, and synthetic polymers).[155,156] To predict the aggregation state, phase diagrams are constructed by tuning the temperature, pH, or ionic strength as a function of the ratio between the two interacting molecules (Figure 25b).[108] This type of phase separation is dominated by electrostatic interactions, hydrogen bonding, π-π interactions, density and charge distribution, long-range electrostatics, hydration effects, and is driven by the increase in entropy associated with the release of counterions and rearrangements of water molecules during the formation of macro-ion pairs (Figure 25c).[144] Finally, simple coacervation[108,142,144,145] occurs due to attractive interactions present in a single

component. It consists in its demixing from water at a certain solution temperature, pH and salt concentration, resulting in a condensed phase called a simple coacervate. Many proteins with disordered regions, known as Intrinsically Disordered Proteins (IDPs), have been found to undergo simple phase separation,[108] driven by a combination of the previously mentioned interactions. From a theoretical viewpoint, simple coacervation can be modelled using the Flory-Huggins theory, as a segregation between a polymer and a solvent.[108] Recently, Elastin Like Polypeptides (ELPs) have been proposed as a relevant simplified model of IDPs. They are sequences of (VPGXG) pentapeptides where the guest residue X can be any amino acid except for proline, and are recombinantly produced in Escherichia coli.[157] They exhibit a lower critical solubility temperature (LCST) in water, meaning that below their cloud point temperature (T_{cp}), they are miscible in water and above their cloud point temperature, they phase separate and form coacervates. The T_{cp} can be tuned mostly by controlling the amino acid repeat sequence and polymer length.[158] As such, they undergo simple coacervation above T_{cp}, driven by a preference for homotypic self-interactions over protein-solvent interaction, as opposed to charge-mediated complex coacervation, in which oppositely charged species form coacervates in solution.[159] One of the main leaders in the ELP field is the Professor A. Chilkoti, who focuses an important part of his research on these types of proteins.[160–162]

In the following paragraphs, we will see how these LLPS systems have been included within artificial cells to make subcompartmentalized systems, and the different stimuli used to induce the LLPS.

3.2. Membraneless organelles based on LLPS in artificial cells towards complex synthetic cells

Studying the LLPS process responsible for the formation of membraneless organelles presents challenges when investigated in living cells. Indeed, with numerous components present in eukaryotic cells, it becomes difficult to determine which molecules are truly involved in this process. However, valuable insights into this phenomenon can be gained by studying coacervation in minimal cell-mimicking systems that consist only of essential biological molecules.[163] These systems offer a controlled environment to identify the interactions that drive phase separation and

understand the key molecules and parameters involved. To create such minimal systems, micrometer-sized containers like droplets and liposomes are used, which are comparable to the volume of a eukaryotic cell. These containers can be efficiently synthesized, enabling high statistical analysis in a single experimental run, while allowing precise control over factors such as pH, temperature, and solute concentrations.[163] They especially benefit from the advances achieved in the microfluidic technique, offering high control over size, structure and content of these cell-mimic architectures.[164] Here, we present recent progress in LLPS, particularly coacervation, within artificial compartments ranging from water-in-oil droplets to cell-mimicking vesicles.

3.2.1. Coacervate-in-droplet

Droplets are often used as simple synthetic compartments to study and construct bottom-up biological systems. These compartments comprise an aqueous phase, mimicking the cytoplasm, dispersed within an immiscible oil phase. Sometimes enclosed by a lipid, polymer or protein membrane, the droplets create a distinct boundary between their internal environment and the external surroundings. Unlike vesicles, droplets do not possess a bilayer. They are straightforward to produce in bulk and can also be easily generated using microfluidic systems. We describe here their use as model containers for studying LLPS in confinement, especially focusing on their dynamic formation in response to different triggers.

3.2.1.1. Light triggering

Dynamic modulation of the phase transition can be done by using an environmental stimulus such as light, which can precisely be controlled spatially and temporally. For instance, Reed *et al.*[165] have engineered an intrinsically disordered arginine–glycine–glycine (RGG) domain, from the protein LAF-1, with an opto-responsive photocleavable protein (PhoCl) and a solubilizing maltose-binding protein (MBP). The former drives the coacervation, the second cleaves in response to 405 nm light, and the latter solubilizes the RGG protein and inhibits phase separation at room temperature. Following a single short pulse of light, cleavage of the PhoCl domain results into two fragments (Figure 26): the first fragment is an N-terminal fragment containing MBP and

most of the PhoCl protein. The second fragment is a C-terminal fragment containing the RGG protein. The removal of the solubilization domain causes the protein to phase separate and form coacervates rapidly. In their work, Seo *et al.*[166] have been using light as a mean to enhance the stability of their complex coacervates, made from the LLPS of negatively charged hyaluronic acid (HA) and positively charged poly(L-lysine) (PLL). They have been engulfing their coacervates within cross-linked PEG-diacrylate shells to improve their stability, without inhibiting their loading capacity.

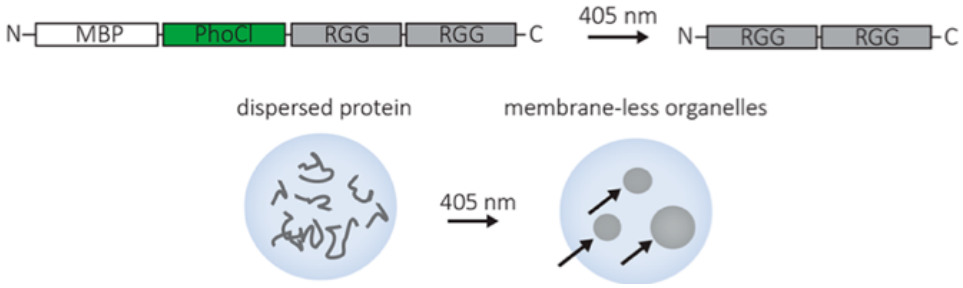

Figure 26: Schematic of the MBP-PhoCl-RGG-RGG molecule designed to cleave upon illumination with 405 nm light to form RGG-RGG, resulting in protein condensation. Experiments were performed inside cellular-sized water droplets. Arrows indicate coacervates formed inside a water droplet.[165]

3.2.1.2. Temperature triggering

Highly programmable and tuneable elastin-like polypeptides (ELPs) provide an alternative approach for designing LLPS assemblies within picolitre droplets. Particularly, their thermoresponsive properties due to their lower critical solubility temperature (LCST) can be harnessed for this purpose. In one of Chilkoti's group experiments, an engineered temperature sensitive RNA-ELP could regulate translation through the reversible sequestration of mRNA within droplet-based protocells.[167] Indeed, upon heating, translation and transcription were inhibited as mRNA was sequestered into biomolecular condensates, impeding the translation of sfGFP by protein machinery (Figure 27).

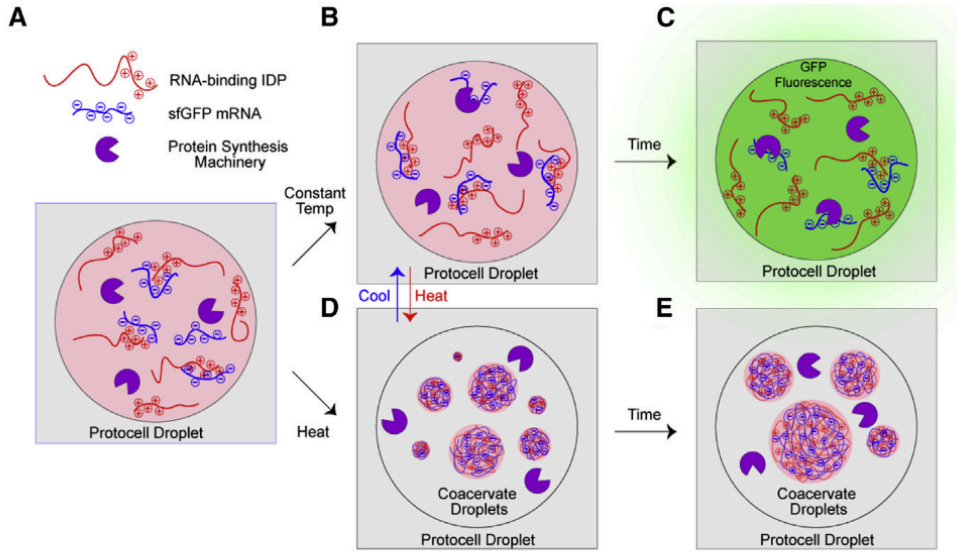

Figure 27: Engineered Ribonucleoprotein Granules for Inhibiting Translation within Droplet-Based Protocells (A) Schematic of microfluidic-generated droplets and the inhibition of translation with messenger ribonucleoprotein granules inside the microdroplet protocells (right). Artificial RNA-binding IDPs coacervate mRNA transcripts upon heating (B → D) and suppress translation (D → E), and coacervation is reversed by cooling (D → E), leading to resumption of translation (B → C).[167]

Even today, it is not fully understood how the complexity of the cell's interior can affect the structural and functional behaviour of IDPs. To mimic this intracellular organization, an ATPS system can be viewed as a simplified model to increase a system's complexity, and have a better understanding of how IDPs could act in more extreme conditions. This was for example done by Zhao *et al.*,[24] who integrated ELPs in a cytomimetic aqueous two-phase system (ATPS) and observed the phase separation and spatial distribution of the ELPs in this environment. Due to changes in the conformational states of the ATPS, they observed the dynamic formation and distribution of ELP-rich droplets into synthetic organelles upon heating above the T_{cp} of ELPs. Other types of proteins and enzymes were as well encapsulated with the ELPs to follow up their partitioning within this configuration (Figure 28). Overall, the phase separation and spatial distribution of artificial IDPs were investigated in a biomacromolecular crowded environment that mimics the cell cytoplasm. To furtherly deepen this work, thermally responsive ELPs were engineered with polymers like PEG and Dextran.[23] The highly selective partitioning of the ELP-conjugates was observed in the ATPS phase, as well as their self-assembly into coacervate-core micelles, closely mimicking membraneless organelles. Furthermore, an ELP monoblock was

encapsulated with the ELP-polymer conjugates. Both ELP-conjugates exhibited a surfactant-like property, compartmentalizing and stabilizing the monoblock ELP coacervates *via* temperature control. These findings are a step forward in constructing more complex and realistic synthetic organelles with a high degree of hierarchical complexity and dynamic behaviour.

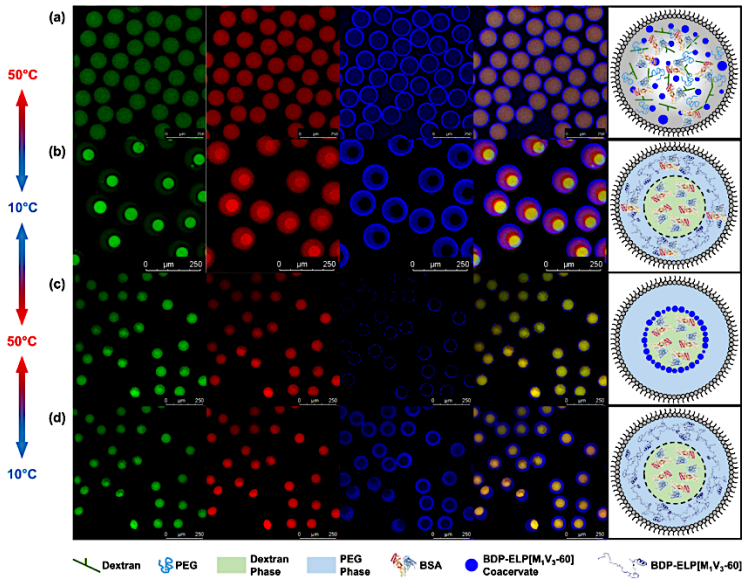

Figure 28: Representative confocal images of Rh-BSA, BDP-ELP[M1V3-60], and ATPS within microdroplets at different temperatures showing thermally induced dynamic organization and motion of the ELP-rich droplets and the spatial organization of protein and ELP. Microdroplets were initially imaged at 50°C (a), then at 10°C (b),then again at 50°C (c),and again at 10° C(d).[24]

Finally, Deng and coworkers[168] designed Y-shaped DNA nanostructures which encompass different sticky end sequences. Each Y-motif can self-assemble into DNA coacervates under temperature trigger. To demonstrate the potential of these DNA coacervates as artificial membraneless organelles, biomolecules were selectively partitioned within the coacervates. In addition, it was demonstrated that free exchange of molecules between the DNA coacervates occurred. This was done by introducing a photo switchable intracellular-like communication display using azobenzene-tethered DNA molecules, which can capture and release their complementary DNA strand upon visible/ultraviolet irradiation and the associated trans/cis photo-isomerization of azobenzene (Figure 29).

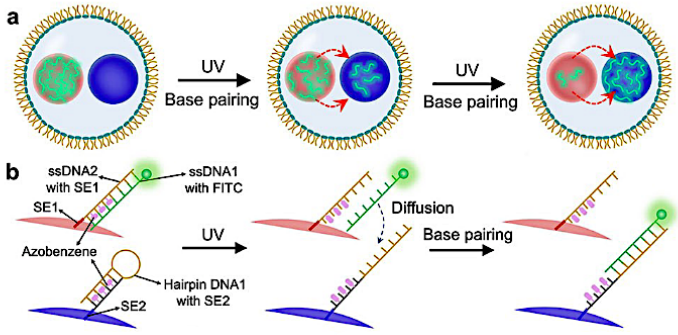

Figure 29: a) Schematics of one-way directional transport of molecules between DNA coacervates and b) the mechanism of photo-actuated transfer of ssDNA.[168]

3.2.1.3. Transmembrane diffusion

Phase transition can be achieved by diffusing molecules of interest, either through channel-forming transmembrane proteins,[169,170] DNA nanopores,[171] or by the diffusion of small molecules through porous membranes, like Booth *et al.*[172] demonstrated within their proteinosomes (Figure 30). They produced these latter by cross-linking a monolayer of bovine serum albumin and poly(N-isopropylacrylamide) nanoconjugates. Small molecules like ATP and chlorhexidine were able to diffuse through the proteinosome membrane and undergo coacervation with the encapsulated polymers. The coacervate structure could furtherly be spread onto the membrane in the form of a thin layer through simple electrostatic interactions and be redispersed back into the proteinosome lumen upon addition of monovalent salt. This allowed for spatial and diffusive coupling of simple enzymatic cascades, resulting in increased reaction rates.

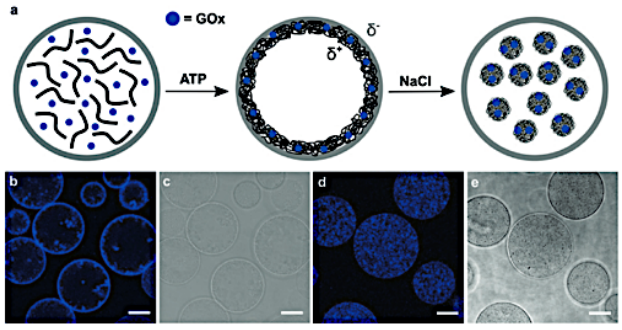

Figure 30: a) Scheme illustrating the spatial positioning and relocation of proteinosome-entrapped coacervates. Diffusion of ATP into preassembled proteinosomes (leftgraphic) containing PDDA (black lines) and GOx (filled blue circles) gives rise to the in situ assembly of a

positively charged (δ+) GOx-loaded ATP/PDDA coacervate phase against the negatively charged (δ^-) inner surface of the proteinosome membrane (centre graphic). Subsequent addition of NaCl results in transformation and relocation of the enzyme-containing coacervate shell into discrete GOx-loaded coacervate micro-droplets dispersed within the proteinosome lumen (right graphic); b,c) Confocal (b) and optical (c)microscopy images of PDDA-containing proteinosomes after addition of ATP showing formation of a thin sub-membrane coacervate layer. Blue fluorescence arises from DyLight 405-GOx sequestered into the coacervate phase; scale bars = 20 mm. d,e) As for b,c but after addition of NaCl showing relocation of the coacervate phase into micro-droplets dispersed throughout the lumen; scale bars = 20 mm. [172]

In another contribution, Huang and coworkers[173] also took advantage of the permeability of their proteinosomes to regulate the configuration of the sub compartments within their droplets. Quaternized dextran/succinyl dextran coacervate droplets were encapsulated within a dextran phase. Then, PEG with different molar masses was added through the permeable membranes of the proteinosomes. This impacted the spatial inner organization between the coexisting layers as the interfacial tensions between PEG and dextran evolved. Indeed, as the molar masses of PEG decreased, the inner configuration changed from nesting, to partial-engulfing, to petal-like morphologies (Figure 31). Furthermore, each phase showed a distinct microenvironment with selective hosting of various biomacromolecules.

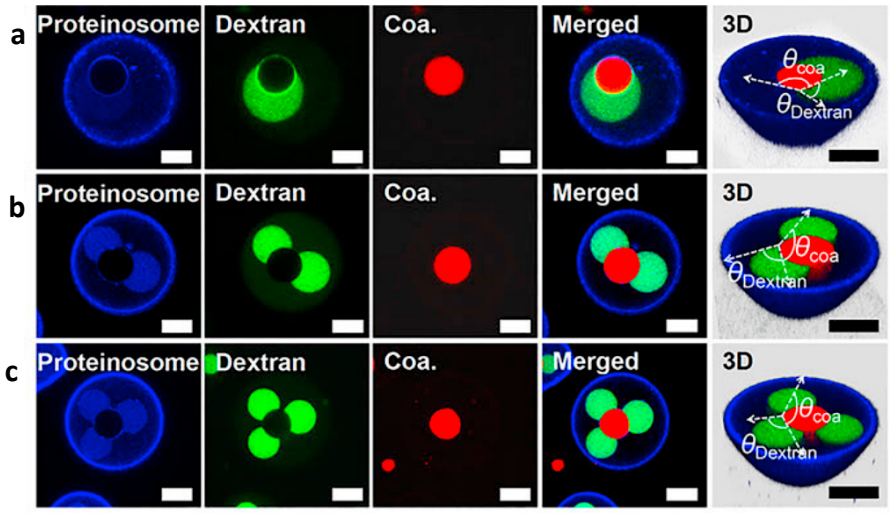

Figure 31: Molecular weight of PEG and salt concentration mediated the spatial organization of heterogeneous biomacromolecule-condensed phases inside proteinosomes (a-c) Confocal fluorescence images and 3D images of partial engulfing configuration and petal-like multi-microcompartments inside proteinosomes after the addition of PEG with MW 10, 8, and 2 kDa, respectively. Scale bars: 3 mm.[173]

Another droplet design was proposed by Rowland *et al.*,[25] who made liposome-stabilized droplets as artificial mineralizing vesicles for biomimetic mineralization (Figure 32a). The liposomes prevented droplet coalescence, without blocking the entry of small molecules. As urea was added to the external medium, the hydrolysis of urea by urease produced the carbonate anion (Ca_3^{2-}), which in the presence of calcium (Ca^{2+}) formed $CaCO_3$ (Figure 32b). Mineralization was restricted to the dextran-rich phase due to preferential urease partitioning to this phase, and to the coacervate phase which was containing the Ca^{2+}.

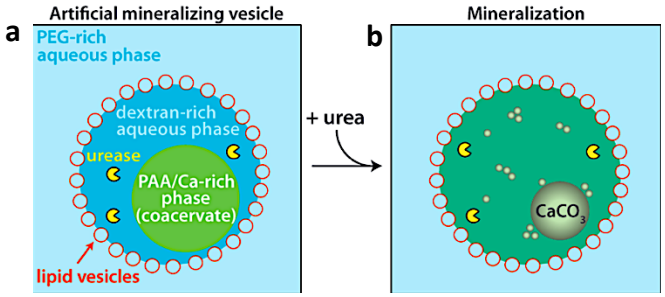

Figure 32: Illustration of Mineralization Inside Coacervate-Containing Artificial Mineralizing Vesicle (a) Illustration of individual AMV, which is a multiphase, catalytically active droplet in a vesicle-stabilized all-aqueous emulsion. Each droplet contains a coacervate phase rich in polyaspartic acid (PAA) and Ca^{2+} surrounded by a dextran-rich aqueous phase containing the enzyme urease. (b) Addition of urea results in localized hydrolysis by urease in the dextran-rich phase to produce carbonate, initiating mineral formation and displacing PAA from the coacervate.[25]

Finally, in their experiments, Kojima *et al.*[174] manually pipetted an adenosine triphosphate/poly(diallyldimethylammonium chloride) coacervate within a PEG/Dextran ATPS phase. They used salt-induced regulation with NaCl to disintegrate the coacervates, which released their inner content in biomolecules. They demonstrated that the kinetics of their enzymatic reaction could be modulated depending on the presence of coacervates within the ATPS phase. In addition, they showed the importance of segregation in the hierarchical organization of condensates, as it reduces the substrate inhibition of dextranase and improves the kinetics of the enzymatic cascade reactions.

3.2.2. Coacervate-in-vesicle

Compared to droplets, creating vesicles is a more demanding task. Nevertheless, they provide a stronger likeness to cells due to their semipermeable membranes, inner aqueous compartments, and intricate three-dimensional architecture. With their picolitre aqueous volumes that are enclosed within a phospholipid bilayer, liposomes stand out as the vesicles of choice and serve as ideal reaction vessels that emulate the cellular environment. In the upcoming sections, we will delve into various approaches employed to initiate and explore coacervation within these vesicles.

3.2.2.1. pH trigger

Although lipid membranes exhibit a very low permeability to charged ions, their native proton permeability is high enough to equilibrate a transmembrane pH gradient.[175] Hence, pH discards the need for membrane pores. It is also a parameter that can be easily changed during an experiment and is important to be controlled in many enzymatic reactions. Love *et al*.[176] exploited the pH responsiveness of polylysine (PLys) to drive LLPS and form single coacervate droplets within lipid vesicles (Figure 33). Indeed, above the pKa of PLys, coacervate formation with a counter polyanion is stopped, whereas it is triggered below the pKa of PLys. It was furtherly demonstrated that the formation of the coacervates activated the enzyme's activity by increasing its concentration and changing the local environment around the enzyme and reactants.

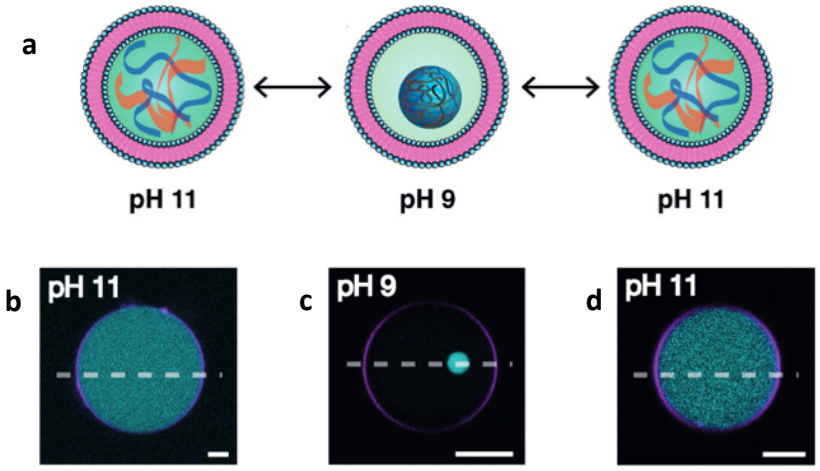

Figure 33: Reversible in situ formation of PLys/ATP coacervates in lipid vesicles by a reduction in pH (a) Cartoon depicting the pH-controlled formation of coacervate microdroplets within giant vesicles (b-d) Fluorescent confocal images of GUVs made from POPC/Cholesterol containing PLys and ATP at a 4:1 molar ratio. Scale bar = 5 mm. (b) At pH 11, after washing the outer solution with iso-osmolar pH 11 buffer solution, (c) at pH 9, after the addition of iso-osmolar pH 7.3 buffer, and (d) after returning the pH to pH 11.[176]

Last and al.[175] have also been using pH to control the assembly of their membraneless organelles within liposomes, by rendering either the ATP molecules neutral (using acidic pH in case of polylysine/ATP) or by rendering spermine molecules neutral (using basic pH in case of polyU RNA/spermine (Figure 34a). This strategy was furtherly used to induce and study the electrostatic and hydrophobic interactions between the coacervate and the lipid membrane. Electrostatic interactions were generated by doping the lipid membrane with a charged lipid, which efficiently recruited coacervates to the membrane and restricted their movement along the inner leaflet (Figure 34b). However, no morphological changes in the liposomes or coacervates were visible, which suggests that the interaction was of relatively low strength. To induce a stronger interaction, hydrophobic interactions were induced by physically anchoring one of the coacervate components into the lipid membrane: cholesterol (Figure 34c). Indeed, cholesterol is known to spontaneously insert into lipid bilayers. Then, spermine and cholesterol-tagged RNA were added within the liposomes. Due to such interactions, coacervates preferentially resided at the surface of the liposomes, lose their regular spherical shape by wetting the membrane, and even locally affect the structure of the lipid bilayer.

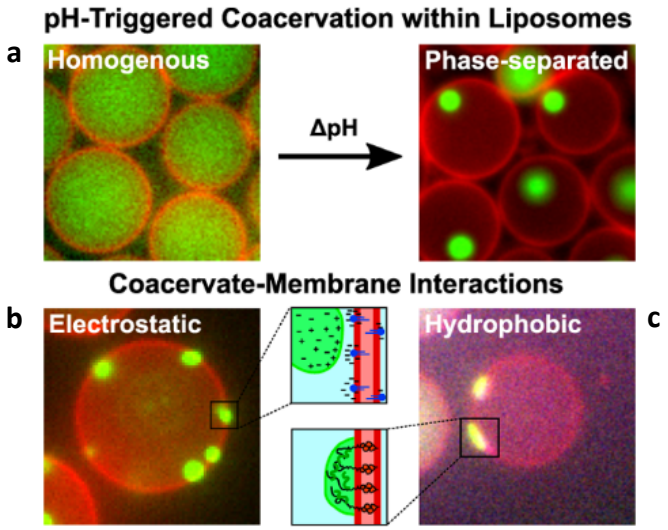

Figure 34: (a) pH-controlled coacervation of pLL/ATP within liposomes. Fluorescence time-lapse images of the liposomes. After the external pH is raised, the pH level inside the liposomes equilibrates to it over the course of minutes and coacervation begins to take place. t0 was chosen as the time just before the first coacervation event occurred. (b) Coacervate−membrane interactions in charged (using PIP3) liposomes. Conceptual sketch and fluorescence images showing coacervate formation for the case of charge-based interactions between the coacervate and lipid membrane, due to charge matching of the polyanionic PIP3 and polycationic pLL (c) conceptual sketch and images of the membrane wetted by cholesterol-RNA/spermine coacervates.[175]

3.2.2.2. Temperature trigger

Another trigger to assemble coacervate organelles within liposomes is temperature. Deng *et al.*[22] have been encapsulating poly U and spermine coacervates within liposomes using a microfluidic system, to ensure the production of monodisperse coacervates and liposomes. Within their experiments, they showed the dynamics of their system by controlling the assembly and disassembly of their coacervates using temperature, as they exhibit an LCST (Figure 35). In addition, a double-stranded DNA is encapsulated, which partitions efficiently within the coacervates due to electrostatic interactions. The DNA localization follows the dynamics of coacervation and dissolution and allows to build spatially functional artificial cells as in vitro transcription (IVTx) is achieved.

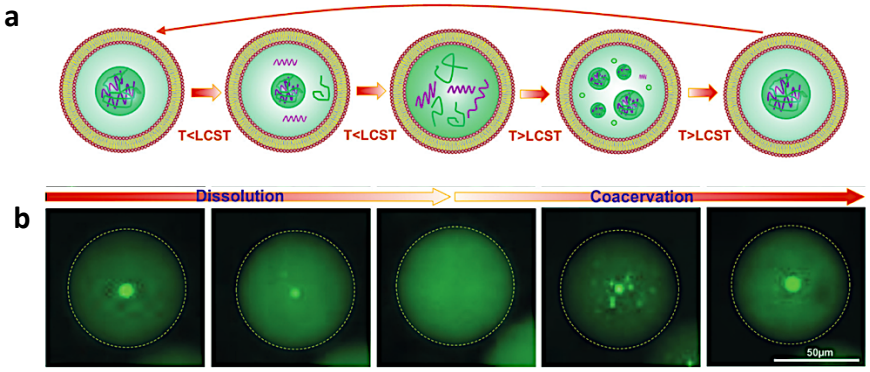

Figure 35: Thermal dynamics of the membraneless organelle-like compartment in liposomes (a) Illustration and (b) magnified views of a single liposome with dynamic artificial organelles. Polycation = spermine, polyanion = polyU RNA.[22]

3.2.2.3. Transmembrane diffusion

Lipid bilayer membranes are an important step towards exhaustive mimics of biological cells. However, these structures are sometimes challenging to produce and to induce functionality. Indeed, due to their impermeability to most macromolecules, lipid bilayers can be quite limiting when it comes to the use of giant vesicles for reactions in which substrate entry and product are necessary. In these cases, the insertion of protein pores such as alpha hemolysin is necessary.[177] In their paper, Deshpande *et al.*[27] proposed two strategies to induce coacervation within their liposomes. The first strategy was to encapsulate polylysine (pLL) as the polycation and insert alpha hemolysin pores with the liposome's membrane (Figure 36). Then, ATP was added to the external medium and let to diffuse through the selective pores. Protein-pore mediated permeation of small molecules into liposomes to trigger the LLPS passively. The second strategy consisted in inducing the LLPS via active mechanisms by inducing enzymatic polymerization of nucleic acids. This was done by allowing the diffusion of a substrate, here uridine diphosphate (UDP), through the pores. The substrate triggers the polymerization of RNA oligomers through the catalysis of PNPase, to form poly U polymers. Complex coacervation was subsequently induced into polyU/spermine coacervates. Finally, it was shown that the sequestration of proteins and the possibility to host metabolic reactions such as the enzymatic activity of β-galactosidase was possible within the coacervates.

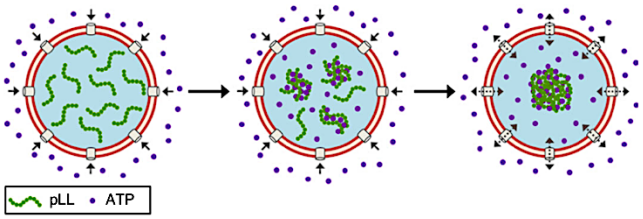

Figure 36: Schematic showing the formation of a pLL/ATP coacervate within a liposome. ATP from the environment diffuses inside the liposome through α-hemolysin pores. It interacts with pLL molecules present inside the liposome, initiating coacervation throughout the liposome. Over time, individual coacervates coalesce to form a single coacervate.[27]

3.2.2.4. Osmotic modulation

As a control parameter to induce coacervation, osmotic modulation is regularly used by eukaryotic cells to assemble membraneless organelles to regulate their metabolic activities. It is thus a relevant stimulus to use for in vitro experiments. Huck and coworkers[178] used a partially dewetted liposome structure to induce a hypertonic shock and control the phase separation of cell lysates to induce the formation of coacervates (Figure 37).

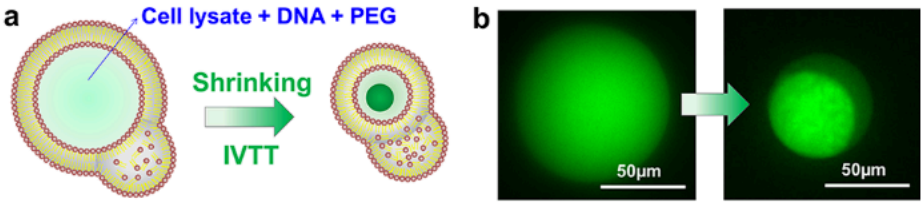

Figure 37: (a-b) Coacervate formation in liposomes induced by decrease of volume.[178]

3.2.3. Coacervate-in-coacervate

So far, we focused on how different containers have been used to induce and study coacervation within them in a controlled way. But coacervation itself can as well define the boundaries of the container. The key advantage of these coacervation-rich vesicles is the encapsulation and accumulation of biomolecules within the coacervate shells. In this manner, contents can preferentially concentrate and be exploited for spatial localization and coupling of enzyme cascade reactions.[163] Multiple phase-separated domains can coexist, differing in their properties and in the molecules they can segregate.

3.2.3.1. Complex coacervation

The first study that demonstrated the possible hierarchical organization of coexisting coacervate phases was achieved by Mountain *et al*.,[179] with a system combining synthetic polyelectrolytes, peptides and nucleic acids. They managed to form up to three coexisting macromolecule-rich liquid compartments through complex coacervation, by mixing several polyanions and polycations such as poly(acrylic acid), poly(L-glutamic acid), poly(allylamine hydrochloride) and protamine sulfate, to name a few of the tested combinations (Figure 38). They highlighted that in some systems, the order of addition of the polyelectrolytes could have an importance on the formation of multiphase coacervates. Similar experiments were conducted by Lu *et al*.,[180] who also formed hierarchically organized multiphase coacervates with up to three coexisting layers for a wide range of model coacervates. They used poly(3-sulfopropyl methacrylate) (PSPMA)/poly(diallyl dimethylamonium chloride) (PDDA), ATP/poly(allylamine hydrochloride) (PAH) and poly(acrylic acid) (PAA)/PDDA to form three coexisting layers. They notably demonstrated and explained how the interfacial tensions and critical salt concentration inputs were responsible for the hierarchical arrangements and the demixing transitions in multiphase droplets. Finally, Chen *et al*.[181] constructed coacervate-in-coacervate multi-compartment protocells to spatially control competitive enzyme cascade reaction in between the multi-compartment microstructures. Due to the dissimilar spatial organization, different signal generations and product outputs were observed as each phase demonstrated distinct physical and chemical properties such as density and partition coefficient.

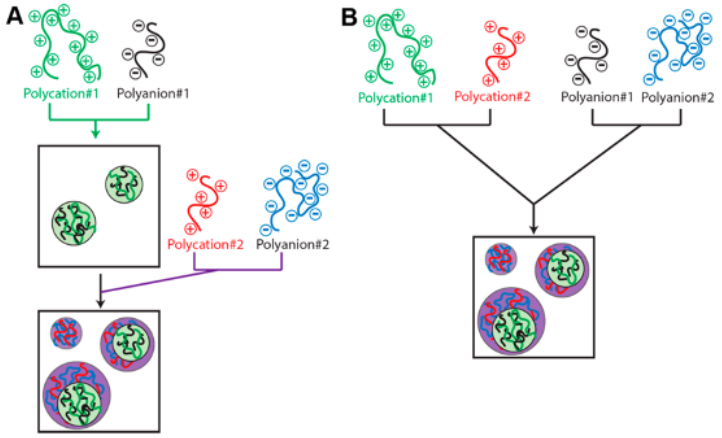

Figure 38: (a) Sequential formation of multiphase coacervates (b) like charge polymers are premixed and added to the sample simultaneously.[179]

3.2.3.2. Thermal-responsive phase separation

To mimic the capacity of cells to subtly change the amino acid composition and concentration of IDPs to control their coacervation and compartmentalization locally,[130,182] López and coworkers[183] designed a library of ELPs with multiple lengths, architectures, and sequence composition that can mimic in vitro such phenomena, which enables in-depth studies of the phase separation of minimal genetically encodable IDPs (Figure 39).

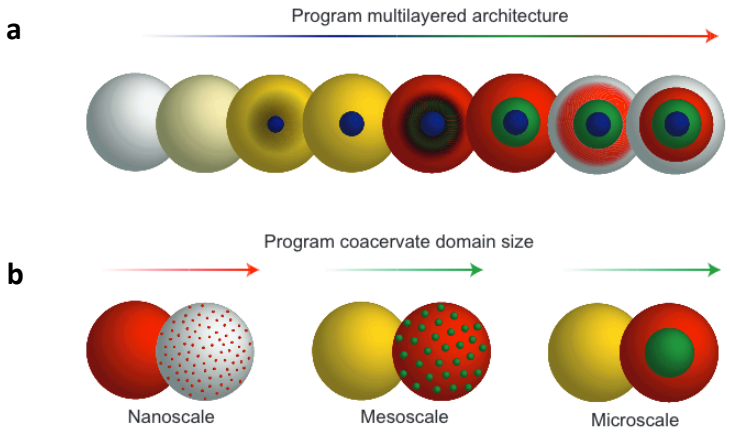

Figure 39: (a) Schematic of the temperature-triggered assembly of multilayered microscale coacervates (b) and coacervates with a programmable domain size generated within homogeneous microdrops that contain aqueous mixtures of ELPs encoded for coacervate self-assembly.[183]

To conclude on this part, LLPS *via* coacervation turns out to be an essential way by which cells organize their interiors. Advancing our understanding of this phenomenon can be significantly enhanced by using bottom-up minimal systems, which enable the spatiotemporal organization of synthetic coacervate microdroplets within compartmentalized chemical systems. This organization is controlled through various means such as the diffusion of specific chemical components, or the manipulation of the internal or external environment of the synthetic cells. The utilization of versatile microfluidic technology enables precise and controlled experimentation in this field.

4. Evolution of multicompartmentalization at the interface between living and non-living systems

Lately, there has been and increasing interest in constructing artificial cells combined to whole biological structures. While artificial cells have inherent limitations due to their simple nature and lack of evolved biochemical pathways, efforts have been made to address these shortcomings by developing hybrid systems that combine the biochemical richness of natural cells with the robustness and chemical versatility of synthetic chemistry.[16] This creates a symbiotic relationship between the elements involved, expanding the scope and possibilities of artificial cells. Three main hybridization routes have emerged.[113] Firstly, population hybridization involves communication and exchange of information and materials between biological and artificial cells across spatial

distances. Secondly, network hybridization refers to the physical linkage of artificial and biological cells in a network or tissue-like arrangement while maintaining their distinct identities. Lastly, embedded hybridization involves the embedding of living cells within synthetic ones or vice versa, where the encapsulated cells perform organelle-like functions within their host. Since this chapter specifically focuses on the compartmentalization structure of cells, only the embedded hybridization route will be discussed.

4.1. Biological cells encapsulated in synthetic cells

4.1.1. Living system-in-vesicle

Several living systems encapsulated in synthetic ones for the creation of hybrids organizations have been demonstrated. For example, Elani *et al.*[184] encapsulated within giant lipid vesicles engineered colon carcinoma cells using a microfluidic and emulsion phase transfer technique (Figure 40a-b). More specifically, the cells were modified to have an organelle-like function and express an enzyme which performed one step of a multi-step enzymatic cascade reaction. The enzymatic product was then further processed by a synthetic metabolism co-encapsulated in the vesicle, and an intense fluorescent signal could be detected (Figure 40c). The encapsulated cell acted as a bioreactor module within the synthetic cells.

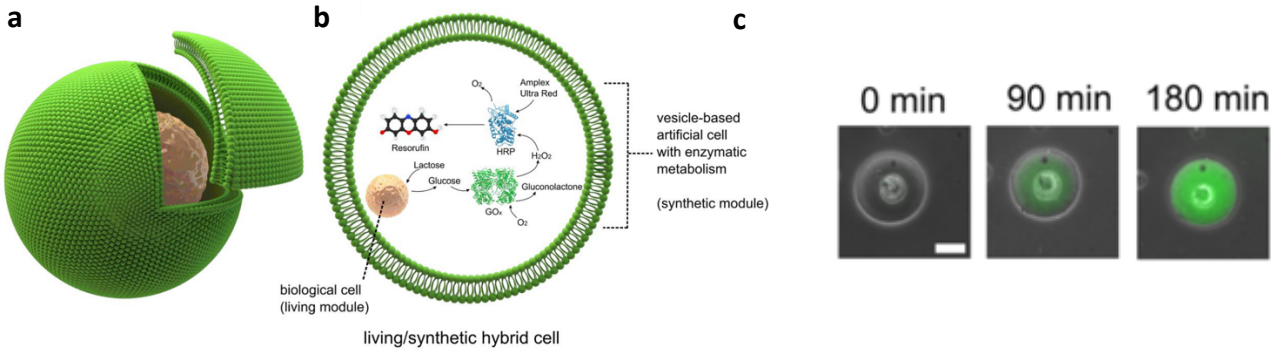

Figure 40: Living/Synthetic hybrid cells (a) Schematic of a biological cell encapsulated inside a vesicle-based artificial cell (b) The encapsulated cell serves an organelle-like function in the vesicle reactor, processing chemical elements which are then further metabolized downstream by a synthetic enzymatic cascade co-encapsulated in the vesicle (c) Representative

brightfield/fluorescence composite images of vesicles/cell hybrids at different time points, showing successful synthesis of reaction products over time compared to control experiments.[184]

This approach was furtherly extended by Tantridou *et al*.,[185] who encapsulated genetically engineered Escherichia coli within vesicles. The bacteria served as biosensors to monitor the lactate concentration within vesicles. In another study, intrinsically disordered regions were used to develop a Förster Resonance Energy Transfer (FRET) biosensor that could dynamically monitor the response of budding yeast to osmotic stress at the cellular level.[186] Finally, Jusková *et al*.[187] encapsulated bacteria within giant lipid unilamellar which were furtherly immobilized within a microfluidic platform to have a real-time monitoring of their microbial development (Figure 41). It has been demonstrated in these examples that, whilst the biological materials conferred functionality to the synthetic cells, these latter played the role of a shield by protecting the encapsulated cells from toxic exteriors, demonstrating a mutually beneficial relationship. Indeed, the shielding capacity of vesicles from chemicals in the surrounding medium such as Cu^{2+} led to a bacterial viability 11 times higher than bacteria in bulk.[184]

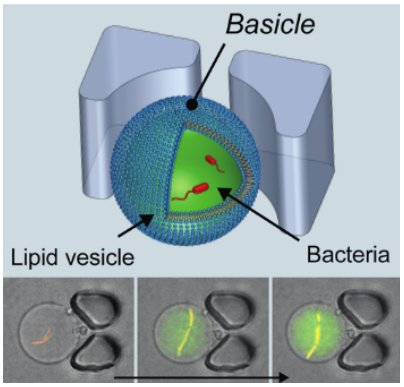

Figure 41: (a) Scheme of the basicles isolated by a microfluidic valve (b) Time-lapse images of a GUV encapsulating a riboflavin (red) producing bacterium (green). Scale bar =25µm.[187]

4.1.2. Living system-in-coacervate

Another way to encapsulate living systems within synthetic cells is by trapping biological structures in coacervates. Indeed, researchers have encapsulated mitochondria[188] (

Figure 42) and chloroplasts in coacervate-based synthetic cells,[189] which had rarely been done before as molecular and supramolecular components such as enzymes, genetic polymers and ribosomes are more commonly encapsulated.[113]

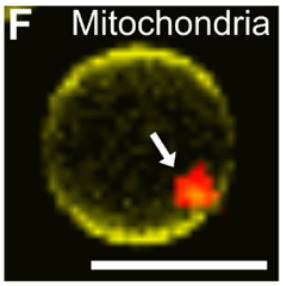

Figure 42: Confocal fluorescence images showing mitochondria isolated from HeLa cells and stained with MitoTracker Green.[188]

In more details, Kumar *et al*.[189] sequestered negatively charged chloroplasts into positively charged poly(diallyldimethylammonium chloride) (PDDA)/carboxymethyl-dextran (CMDX) coacervates through electrostatic interactions (Figure 43). They investigated the photosynthetic activity of the encapsulated organelles by adding 2,6-dichlorophenolindophenol (DPIP, Hill reagent), a dye that preferentially partitions into chloroplasts. The intermittent exposure to light resulted in the reduction of DPIP, observed as a change from blue colour to colourless, confirmed that the electron transport chain remained operational in the sequestered chloroplasts. These findings could lead to interesting applications such as biobattery modules to power encapsulated biochemical processes.[113]

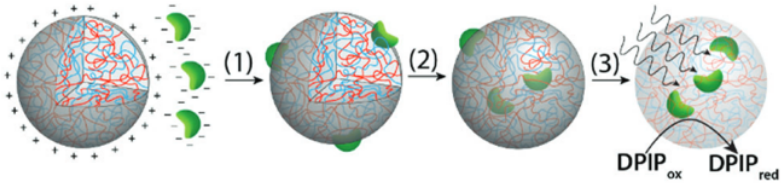

Figure 43: Scheme showing overall strategy for the preparation of photosynthetically active membrane-free protocells based on sequestration of negatively charged intact chloroplasts into positively charged PDDA/ CMDX coacervate micro-droplets. Favorable electrostatic interactions between the micro-droplets and chloroplasts induce the facile capture of the organelles by surface wetting (1), after which the chloroplasts are gradually internalized into the coacervate interior by mechanically induced droplet coalescence and fission (2). Exposure of the chloroplast-containing coacervate droplets to light triggers the photoreduction of DPIP (3).[189]

4.2. Synthetic cells encapsulated in biological cells

The previously described structures can be reversed, with synthetic organelles being introduced into living cells as a form of cellular implant. Thanks to its chemical versatility, synthetic chemistry can offer new and unlimited functions to natural cells, opening new possibilities and routes to complex and illimited compositions and functionality.

4.2.1. Vesicle-in-living system

Einfalt *et al.*[190] developed an impressive technique to encapsulate vesicles within cell-derived giant plasma membrane vesicles (GPMVs), in a close-to-nature environment. Indeed, through a bebbling process, they released hybrid cells with the unique property to be formed of the membrane and cytosolic composition of the donor cell. This confers to the hybrid cells the high biological complexity of natural cells, and allows accessibility to further understand how internalized artificial compounds behave within a reel, complex cytoplasm. It was furtherly demonstrated that in a zebrafish model, these cell mimics showed no apparent toxicity and retained their integrity and function. More recently, Spatz and colleagues[191] successfully introduced giant unilamellar vesicles (GUVs) into living cells, to create synthetic organelles capable of performing distinct tasks: one type of synthetic organelles encapsulated enzymes capable of carrying fundamental cellular metabolic processes, another exerted an intrinsic function to the host cell as a response to an external stimulus, and a third one equipped the host cell with an entirely new, non-intrinsic

functionality. The latter example is a powerful demonstration of the incorporation of entirely new, non-intrinsic functionalities in host cells, opening the infinite possibility to complex machinery with unprecedented functionalities.

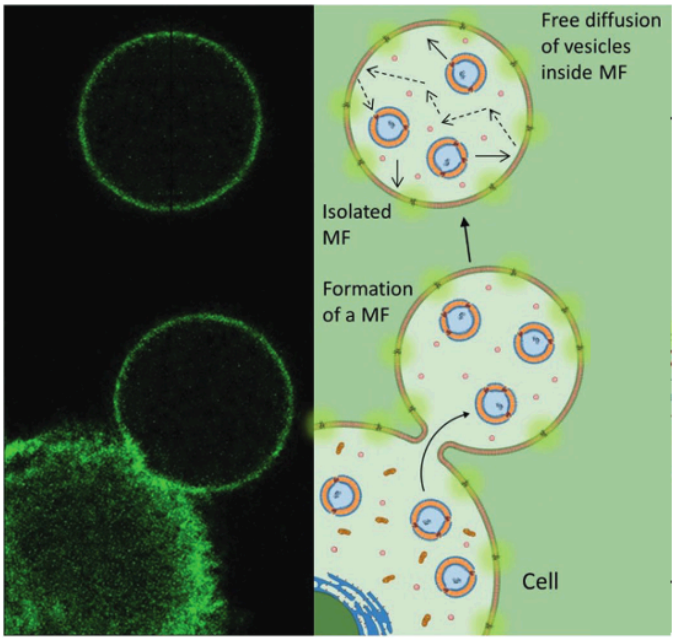

Figure 44: Strategy for creating bioinspired molecular factories. To create a molecular factory (MF) we start by internalizing artificial cargoes (specific molecules and preformed artificial organelles based on polymersomes loaded with active compounds) in the donor mammalian cell. The membrane of the donor cell can also be modified to contain proteins or receptors of interest. Once loaded with all the necessary components of the MF, a transfer of material from the donor cell cytoplasm and membrane is achieved during vesicle formation. After isolation, the MFs are completely independent of the donor cells.[190]

In another work, van Oppen *et al.*[192] designed enzyme-loaded, biodegradable poly(ethylene glycol)-block-poly(caprolactone-gradient-trimethylene carbonate) (PEG-*b*-PCLgTMC) polymersomal nanoreactors as synthetic organelles. Their role is to protect cells from oxidative damage by the action of the internalized catalase-loaded nanoreactors. By functionalizing their surface with cell-penetrating peptides, these nanoreactors were easily uptaken by HEK293T cells and human skin fibroblasts, and results showed effective protection against the toxicity of exogenous H_2O_2, showcasing this system in a therapeutically relevant context.

4.2.2. Coacervate-in-living system

Another route to make vesicles in living systems can be done by coating a synthetic substrates with biological membranes. The biological composition of the membranes imparts cell-like functionality and compatibility to the synthetic compartments, while the interior of the cells can be designed to perform a desired task.[16] Coacervate membraneless microdroplets are attractive and promising candidates towards protocell engineering as they allow easy exchange with the external environment and have high sequestration capacities. However, the absence of an enclosing membrane can still be a limitation in certain applications dues to their lack of long stability, needing an extra stabilization layer that can be obtained through different strategies.[193] In their research work, Zhao *et al.*[194] proposed to coat their quaternized amylose (QAm) and sodium hyaluronate (HA) coacervate microdroplets with yeast cells to obtain stabilized coacervates without hindering their inherent properties (Figure 45). This induced selective capture of Escherichia coli bacteria due the presence of surface proteins in yeast, followed by engulfment and death of the bacteria within these coated coacervates. This is a strategy for advancing coacervate-based protocell design as well as develop smart materials with on-demand functionalization and selective recognition.

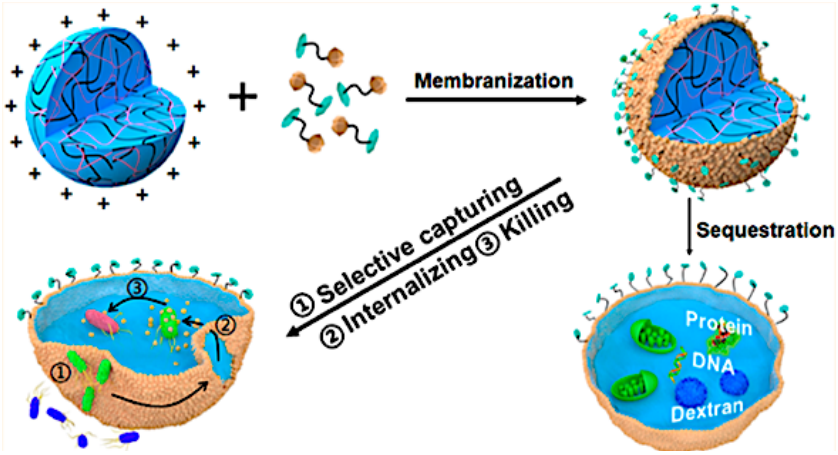

Figure 45: Scheme showing the design process of membrane-bound compartmentalized coacervate microdroplets by reconstitution of natural yeast cellular wall fragments at the interface of coacervate/water. Mannans-containing yeast cellular wall fragments were extracted from the yeast cell via mechanical disruption and then added to the suspension of positively charged Q-

Am/HA coacervate microdroplets. Spontaneous assembly of the fragments at the microdroplets surface results in the formation of yeast cellular wall-camouflaged, molecularly crowded compartmentalization coacervate microdroplets. Illustration showing the compartmentalization coacervate microdroplets could selectively sequester various biomacromolecules including BSA, Dextran and DNA and preload small inter organelles like chloroplast.[195]

With the same idea of developing artificial cells capable of establishing cognate chemical communication with living cells, Mann and coworkers[195] developed biomembrane-coated molecularly crowded hybrid protocells. They prepared positively charged diethylaminoethyl-dextran (DEAE-dextran) and double-stranded deoxyribonucleic acid (dsDNA), loaded with GOx enzyme (Figure 46a). The coacervates were then coated with negatively charged red blood cell membrane fragments, which highly improved their haemocompatibility and blood circulation times. The fragment cells had a high haemoglobin protein (Hb) content, exhibiting a high peroxidase-like activity. The bio-enclosed coacervate vesicles were exploited as a new type of synthetic protocells capable of generating nitric oxide (NO) in the presence of hydroxyurea and H_2O_2, which is exploited for in vitro and in vivo blood vessel vasodilation (Figure 46b). These results present new opportunities for the development of internally organized cell-like entities designed to actively interface with individual living cells and communities of cells.

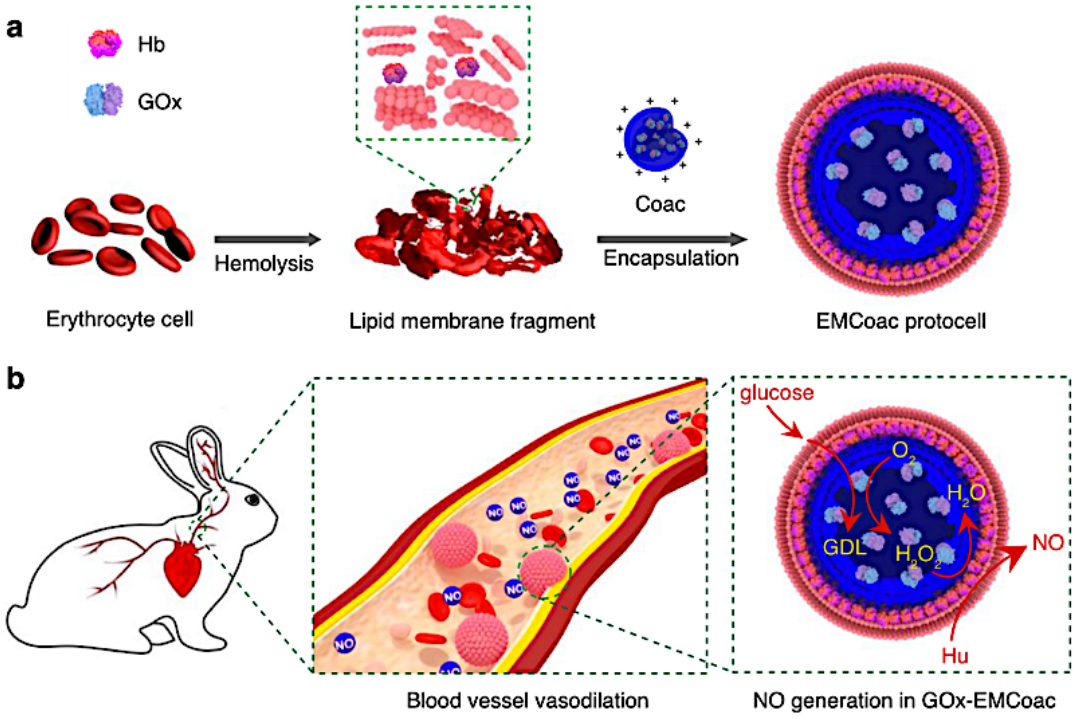

Figure 46: Structure and function of bio-derived hybrid protocells. (a) Scheme showing design and construction of enzymatically active erythrocyte membrane-encapsulated coacervate (EMCoac) protocells. Hemoglobin (Hb)-containing membrane fragments are extracted from fresh sheep blood via hypotonic hemolysis and then added to a suspension of positively charged DEAE-dextran/dsDNA coacervate micro-droplets containing glucose oxidase (GOx). Spontaneous assembly of the fragments at the droplet surface results in formation of biomembrane-coated molecularly crowded hybrid protocells. The bio-derived protocells exhibit enhanced hemocompatibility and display spatially confined peroxidaselike GOx/Hb cascade activity. (b) Illustration showing in vitro and in vivo GOx/Hb cascade generation of NO at micromolar concentrations in the presence of coacervate-sequestered enzyme substrates (glucose and hydroxyurea (Hu), respectively) as a step towards protocell-mediated blood vessel vasodilation. Hb and GOx are spatially positioned on the periphery and in the interior of the protocell bioreactor, respectively (GDL = gluconolactone).[194]

The strategic combination of synthetic cells with living cells holds great promises in the fields of cellular and molecular bioengineering. However, these significant advances do not come without any drawbacks. Indeed, the use of living cells as hosts or integrated systems need to demonstrate high resistance, and certain materials may require additional surface functionalization for efficient uptake by the cells. The potential biotechnological and biomedical applications are extensive and

diverse, ranging from cell therapies protected by artificial membrane delivery platforms to chemical microsystems fuelled by photosynthesis, and even self-healing materials.

5. Conclusion and Outlook

Over the past decade, significant progress has been made in the design and production of eukaryotic cell mimics. Complex synthetic structures increasingly resemble their biological counterparts, providing a deeper understanding of their mechanical, chemical, and physical properties. Particularly, remarkable breakthroughs have been made in integrating and mimicking liquid-liquid phase separation systems using different stimuli. However, an ongoing grand challenge and most probably the next to work on in this field, is to make self-sustainable synthetic cellular systems that can show functional dynamic behaviour.[196] To what degree will research on artificial cells progress until there is unanimous consensus among scientists that the ultimate objective has been achieved?[197]

In the frame of this thesis, we mainly interested ourselves to membraneless organelles, seeking how we could provide new tools to enrich the already existing toolbox for constructing biomimetic systems. A special focus was made on synthetically mimicking these membraneless structures using ELPs. As we have seen in the state of the art, ELPs offer a wide range of experimental possibilities depending on their length and the polymers or enzymes they are conjugated to. Hence, including them within liposome structures using a capillary microfluidic-based technique has opened new structural and functional unprecedented properties.

The first part of this manuscript will focus on the co-encapsulation of membranebound and membraneless organelles in a cell-like chassis, as step towards resembling natural cell structures. The second part will deepen our understanding on the dynamic assembly of intracellular membraneless organelles used to control an enzyme reactivity in response to using a biologically relevant stimulus, here, osmotic pressure modulation. In a third part, a more qualitative analysis of the uptakes and interactions between the coacervates and the enzymes will be done. Finally, we will finish with a general conclusion on this PhD work and will offer perspectives for future developments in this field.

6. References

[1] A. Oparin, *Nature* **1938**, *142*, 412–413.
[2] B. Ghosh, R. Bose, T.-Y. D. Tang, *Current Opinion in Colloid & Interface Science* **2021**, *52*, 101415.
[3] P. Stano, *Life* **2018**, *9*, 3.
[4] J. W. Szostak, D. P. Bartel, P. L. Luisi, *Nature* **2001**, *409*, 387–390.
[5] M. Marguet, C. Bonduelle, S. Lecommandoux, *Chem. Soc. Rev.* **2013**, *42*, 512–529.
[6] R. Roodbeen, van Hest J. C. M., *BioEssays* **2009**, *31*, 1299–1308.
[7] P. A. Beales, B. Ciani, S. Mann, *Interface Focus.* **2018**, *8*, 20180046.
[8] N.-N. Deng, M. Yelleswarapu, L. Zheng, W. T. S. Huck, *J. Am. Chem. Soc.* **2017**, *139*, 587–590.
[9] A. Peyret, E. Ibarboure, N. Pippa, S. Lecommandoux, *Langmuir* **2017**, *33*, 7079–7085.
[10] R. J. R. W. Peters, M. Marguet, S. Marais, M. W. Fraaije, J. C. M. van Hest, S. Lecommandoux, *Angew. Chem. Int. Ed.* **2014**, *53*, 146–150.
[11] D. M. Mitrea, R. W. Kriwacki, *Cell Commun Signal* **2016**, *14*, 1.
[12] W. Mu, Z. Ji, M. Zhou, J. Wu, Y. Lin, Y. Qiao, *Sci. Adv.* **2021**, *7*, eabf9000.
[13] N. G. Moreau, N. Martin, P. Gobbo, T.-Y. D. Tang, S. Mann, *Chem. Commun.* **2020**, *56*, 12717–12720.
[14] Z. Liu, W. Zhou, C. Qi, T. Kong, *Advanced Materials* **2020**, *32*, 2002932.
[15] B. C. Buddingh', J. C. M. Van Hest, *Acc. Chem. Res.* **2017**, *50*, 769–777.
[16] C. Guindani, L. C. Da Silva, S. Cao, T. Ivanov, K. Landfester, *Angew Chem Int Ed* **2022**, *61*, DOI 10.1002/anie.202110855.
[17] W. Jiang, Z. Wu, Z. Gao, M. Wan, M. Zhou, C. Mao, J. Shen, *ACS Nano* **2022**, *16*, 15705–15733.
[18] T. M. S. Chang, *Report of a research project for the BSc Honours, McGill University* **1957**.
[19] M. Preiner, S. Asche, S. Becker, H. C. Betts, A. Boniface, E. Camprubi, K. Chandru, V. Erastova, S. G. Garg, N. Khawaja, G. Kostyrka, R. Machné, G. Moggioli, K. B. Muchowska, S. Neukirchen, B. Peter, E. Pichlhöfer, Á. Radványi, D. Rossetto, A. Salditt, N. M. Schmelling, F. L. Sousa, F. D. K. Tria, D. Vörös, J. C. Xavier, *Life* **2020**, *10*, 20.
[20] S. Mann, *Acc. Chem. Res.* **2012**, *45*, 2131–2141.
[21] S. Cao, L. C. da Silva, K. Landfester, *Angewandte Chemie International Edition* **2022**, *61*, e202205266.
[22] N. Deng, W. T. S. Huck, *Angew. Chem. Int. Ed.* **2017**, *56*, 9736–9740.
[23] H. Zhao, E. Ibarboure, V. Ibrahimova, Y. Xiao, E. Garanger, S. Lecommandoux, *Advanced Science* **2021**, *8*, 2102508.
[24] H. Zhao, V. Ibrahimova, E. Garanger, S. Lecommandoux, *Angew. Chem. Int. Ed.* **2020**, *59*, 11028–11036.
[25] A. T. Rowland, D. N. Cacace, N. Pulati, M. L. Gulley, C. D. Keating, *Chem. Mater.* **2019**, *31*, 10243–10255.
[26] J. W. Hindley, D. G. Zheleva, Y. Elani, K. Charalambous, L. M. C. Barter, P. J. Booth, C. L. Bevan, R. V. Law, O. Ces, *Proc. Natl. Acad. Sci. U.S.A.* **2019**, *116*, 16711–16716.
[27] S. Deshpande, F. Brandenburg, A. Lau, M. G. F. Last, W. K. Spoelstra, L. Reese, S. Wunnava, M. Dogterom, C. Dekker, *Nat Commun* **2019**, *10*, 1800.
[28] C. Xu, N. Martin, M. Li, S. Mann, *Nature* **2022**, *609*, 1029–1037.
[29] H. Seo, H. Lee, *Nat Commun* **2022**, *13*, 5179.

[30] T. E. Miller, T. Beneyton, T. Schwander, C. Diehl, M. Girault, R. McLean, T. Chotel, P. Claus, N. S. Cortina, J.-C. Baret, T. J. Erb, *Science* **2020**, *368*, 649–654.
[31] S. Jagadevan, A. Banerjee, C. Banerjee, C. Guria, R. Tiwari, M. Baweja, P. Shukla, *Biotechnology for Biofuels* **2018**, *11*, 185.
[32] S. Ausländer, D. Ausländer, M. Fussenegger, *Angewandte Chemie International Edition* **2017**, *56*, 6396–6419.
[33] A. S. Khalil, J. J. Collins, *Nat Rev Genet* **2010**, *11*, 367–379.
[34] F. Lienert, J. J. Lohmueller, A. Garg, P. A. Silver, *Nat Rev Mol Cell Biol* **2014**, *15*, 95–107.
[35] K. Göpfrich, I. Platzman, J. P. Spatz, *Trends Biotechnol* **2018**, *36*, 938–951.
[36] W. C. Ruder, T. Lu, J. J. Collins, *Science* **2011**, *333*, 1248–1252.
[37] C. J. Paddon, J. D. Keasling, *Nat Rev Microbiol* **2014**, *12*, 355–367.
[38] R. A. Le Feuvre, N. S. Scrutton, *Synth Syst Biotechnol* **2018**, *3*, 105–112.
[39] J. H. Esensten, J. A. Bluestone, W. A. Lim, *Annu Rev Pathol* **2017**, *12*, 305–330.
[40] P. A. Bachmann, P. L. Luisi, J. Lang, *Nature* **1992**, *357*, 57–59.
[41] H. Kita, T. Matsuura, T. Sunami, K. Hosoda, N. Ichihashi, K. Tsukada, I. Urabe, T. Yomo, *Chembiochem* **2008**, *9*, 2403–2410.
[42] P. L. Luisi, F. Ferri, P. Stano, *Naturwissenschaften* **2006**, *93*, 1–13.
[43] C. Lebleu, Polymersomes Based on PEG-b-PTMC towards Cell-Mediated Delivery of Nanomedicines, Bordeaux, **2019**.
[44] P. Stano, *Chem. Eur. J.* **2019**, *25*, 7798–7814.
[45] B. M. Discher, Y. Y. Won, D. S. Ege, J. C. Lee, F. S. Bates, D. E. Discher, D. A. Hammer, *Science* **1999**, *284*, 1143–1146.
[46] J. S. Lee, J. Feijen, *J Control Release* **2012**, *161*, 473–483.
[47] X. Hu, Y. Zhang, Z. Xie, X. Jing, A. Bellotti, Z. Gu, *Biomacromolecules* **2017**, *18*, 649–673.
[48] F. Ahmed, P. J. Photos, D. E. Discher, *Drug Development Research* **2006**, *67*, 4–14.
[49] R. Rodríguez-García, M. Mell, I. López-Montero, J. Netzel, T. Hellweg, F. Monroy, *Soft Matter* **2011**, *7*, 1532–1542.
[50] L. Messager, J. Gaitzsch, L. Chierico, G. Battaglia, *Curr Opin Pharmacol* **2014**, *18*, 104–111.
[51] F. Meng, Z. Zhong, J. Feijen, *Biomacromolecules* **2009**, *10*, 197–209.
[52] S. Matoori, J.-C. Leroux, *Mater. Horiz.* **2020**, *7*, 1297–1309.
[53] S. Egli, M. G. Nussbaumer, V. Balasubramanian, M. Chami, N. Bruns, C. Palivan, W. Meier, *J. Am. Chem. Soc.* **2011**, *133*, 4476–4483.
[54] E. Rideau, R. Dimova, P. Schwille, F. R. Wurm, K. Landfester, *Chem. Soc. Rev.* **2018**, *47*, 8572–8610.
[55] E. Reimhult, M. M. Virk, *J Biomed Res* **2021**, *35*, 301–309.
[56] Y. Lu, G. Allegri, J. Huskens, *Mater. Horiz.* **2022**, *9*, 892–907.
[57] J. Siepmann, A. Faham, S.-D. Clas, B. J. Boyd, V. Jannin, A. Bernkop-Schnürch, H. Zhao, S. Lecommandoux, J. C. Evans, C. Allen, O. M. Merkel, G. Costabile, M. R. Alexander, R. D. Wildman, C. J. Roberts, J.-C. Leroux, *International Journal of Pharmaceutics* **2019**, *558*, 128–142.
[58] A. D. Bangham, R. W. Horne, *Journal of Molecular Biology* **1964**, *8*, 660-IN10.
[59] J. P. Reeves, R. M. Dowben, *Journal of Cellular Physiology* **1969**, *73*, 49–60.
[60] E. Rideau, F. R. Wurm, K. Landfester, *Adv. Biosys.* **2019**, *3*, 1800324.

[61] K. Shohda, K. Takahashi, A. Suyama, *Biochemistry and Biophysics Reports* **2015**, *3*, 76–82.
[62] M. I. Angelova, D. S. Dimitrov, *Faraday Discuss. Chem. Soc.* **1986**, *81*, 303–311.
[63] N. Rodriguez, F. Pincet, S. Cribier, *Colloids and Surfaces B: Biointerfaces* **2005**, *42*, 125–130.
[64] Y. Lu, W. C. de Vries, N. J. Overeem, X. Duan, H. Zhang, H. Zhang, W. Pang, B. J. Ravoo, J. Huskens, *Angew Chem Int Ed Engl* **2019**, *58*, 159–163.
[65] Q. Li, X. Wang, S. Ma, Y. Zhang, X. Han, *Colloids Surf B Biointerfaces* **2016**, *147*, 368–375.
[66] L.-R. Montes, A. Alonso, F. M. Goñi, L. A. Bagatolli, *Biophys J* **2007**, *93*, 3548–3554.
[67] H. Stein, S. Spindler, N. Bonakdar, C. Wang, V. Sandoghdar, *Frontiers in Physiology* **2017**, *8*.
[68] R. Xu, R. J. Simpson, D. W. Greening, *Methods Mol Biol* **2017**, *1545*, 91–116.
[69] Y. Elani, A. Gee, R. V. Law, O. Ces, *Chem. Sci.* **2013**, *4*, 3332–3338.
[70] A. Peyret, Biomimetic Polymer Vesicles: Towards Structural and Functional Cell Biomimicry, Université de Bordeaux, **2017**.
[71] K. Kamiya, R. Kawano, T. Osaki, K. Akiyoshi, S. Takeuchi, *Nature Chem* **2016**, *8*, 881–889.
[72] A. M. Gañán-Calvo, R. González-Prieto, P. Riesco-Chueca, M. A. Herrada, M. Flores-Mosquera, *Nature Phys* **2007**, *3*, 737–742.
[73] C. Martino, A. J. deMello, *Interface Focus* **2016**, *6*, 20160011.
[74] Y. Ai, R. Xie, J. Xiong, Q. Liang, *Small* **2020**, *16*, 1903940.
[75] H. Zhang, Y. Zhu, Y. Shen, *Small* **2018**, *14*, 1800360.
[76] C.-M. Svensson, O. Shvydkiv, S. Dietrich, L. Mahler, T. Weber, M. Choudhary, M. Tovar, M. T. Figge, M. Roth, *Small* **2019**, *15*, 1970021.
[77] T. Rossow, J. A. Heyman, A. J. Ehrlicher, A. Langhoff, D. A. Weitz, R. Haag, S. Seiffert, *J. Am. Chem. Soc.* **2012**, *134*, 4983–4989.
[78] G. Tang, R. Xiong, D. Lv, R. X. Xu, K. Braeckmans, C. Huang, S. C. De Smedt, *Advanced Science* **2019**, *6*, 1802342.
[79] R. J. Brea, A. Bhattacharya, R. Bhattacharya, J. Song, S. K. Sinha, N. K. Devaraj, *J. Am. Chem. Soc.* **2018**, *140*, 17356–17360.
[80] W. Li, L. Zhang, X. Ge, B. Xu, W. Zhang, L. Qu, C.-H. Choi, J. Xu, A. Zhang, H. Lee, D. A. Weitz, *Chem. Soc. Rev.* **2018**, *47*, 5646–5683.
[81] Y. Wang, Z. Shao, W. Zheng, Y. Xie, G. Luo, M. Ding, Q. Liang, *Biofabrication* **2019**, *11*, 045001.
[82] Q. Ma, Y. Song, W. Sun, J. Cao, H. Yuan, X. Wang, Y. Sun, H. C. Shum, *Advanced Science* **2020**, *7*, 1903359.
[83] R. Xiong, M. Bai, J. N. Chung, *J. Micromech. Microeng.* **2007**, *17*, 1002–1011.
[84] C. Cramer, P. Fischer, E. J. Windhab, *Chemical Engineering Science* **2004**, *59*, 3045–3058.
[85] Y. Hong, F. Wang, *Microfluid Nanofluid* **2007**, *3*, 341–346.
[86] A. Manz, P. Neužil, J. S. O'Connor, G. Simone, in *"Device Fabrication", Microfluidics and Lab-on-a-Chip*, Royal Society Of Chemistry, **2021**, pp. 23–42.
[87] P. Walde, *Bioessays* **2010**, *32*, 296–303.
[88] P. Walde, K. Cosentino, H. Engel, P. Stano, *Chem. Eur. J. of Chem. Bio.* **2010**, *11*, 848–865.
[89] S.-Y. Teh, R. Lin, L.-H. Hung, A. P. Lee, *Lab Chip* **2008**, *8*, 198.

[90] N. Nuti, P. E. Verboket, P. S. Dittrich, *Lab Chip* **2017**, *17*, 3112–3119.
[91] H. Song, D. L. Chen, R. F. Ismagilov, *Angewandte Chemie International Edition* **2006**, *45*, 7336–7356.
[92] P. S. Dittrich, M. Jahnz, P. Schwille, *Chembiochem* **2005**, *6*, 811–814.
[93] T. Beneyton, D. Krafft, C. Bednarz, C. Kleineberg, C. Woelfer, I. Ivanov, T. Vidaković-Koch, K. Sundmacher, J.-C. Baret, *Nat Commun* **2018**, *9*, 2391.
[94] C. B. Giuliano, N. Cvjetan, J. Ayache, P. Walde, *ChemSystemsChem* **2021**, *3*, DOI 10.1002/syst.202000049.
[95] S. Li, X. Wang, W. Mu, X. Han, *Analytical Chemistry* **n.d.**
[96] K. Suzuki, K. Machida, K. Yamaguchi, T. Sugawara, *Chem Phys Lipids* **2018**, *210*, 70–75.
[97] J. W. Hindley, Y. Elani, C. M. McGilvery, S. Ali, C. L. Bevan, R. V. Law, O. Ces, *Nat Commun* **2018**, *9*, 1093.
[98] K. Y. Lee, S.-J. Park, K. A. Lee, S.-H. Kim, H. Kim, Y. Meroz, L. Mahadevan, K.-H. Jung, T. K. Ahn, K. K. Parker, K. Shin, *Nat Biotechnol* **2018**, *36*, 530–535.
[99] S. Berhanu, T. Ueda, Y. Kuruma, *Nat Commun* **2019**, *10*, 1325.
[100] W. Zong, S. Ma, X. Zhang, X. Wang, Q. Li, X. Han, *J. Am. Chem. Soc.* **2017**, *139*, 9955–9960.
[101] H. C. Chiu, Y. W. Lin, C. K. Chuang, C. S. Chern, *NPG Asia Mater* **2008**, 1–1.
[102] S.-H. Kim, H. C. Shum, J. W. Kim, J.-C. Cho, D. A. Weitz, *J. Am. Chem. Soc.* **2011**, *133*, 15165–15171.
[103] M. Marguet, L. Edembe, S. Lecommandoux, *Angew. Chem.* **2012**, *124*, 1199–1202.
[104] S. Thamboo, A. Najer, A. Belluati, C. von Planta, D. Wu, I. Craciun, W. Meier, C. G. Palivan, *Advanced Functional Materials* **2019**, *29*, 1904267.
[105] A. F. Mason, P. Thordarson, *J. Polym. Sci. Part A: Polym. Chem.* **2017**, *55*, 3817–3825.
[106] D. McPhail, L. Tetley, C. Dufes, I. F. Uchegbu, *Int J Pharm* **2000**, *200*, 73–86.
[107] A. Peyret, E. Ibarboure, J.-F. Le Meins, S. Lecommandoux, *Advanced Science* **2018**, *5*, 1700453.
[108] M. Abbas, W. P. Lipiński, J. Wang, E. Spruijt, *Chem. Soc. Rev.* **2021**, *50*, 3690–3705.
[109] J. R. Vieregg, T.-Y. D. Tang, *Current Opinion in Colloid & Interface Science* **2016**, *26*, 50–57.
[110] Y. Lin, H. Jing, Z. Liu, J. Chen, D. Liang, *Langmuir* **2020**, *36*, 1709–1717.
[111] A. F. Mason, N. A. Yewdall, P. L. W. Welzen, J. Shao, M. Van Stevendaal, J. C. M. Van Hest, D. S. Williams, L. K. E. A. Abdelmohsen, *ACS Cent. Sci.* **2019**, *5*, 1360–1365.
[112] A. F. Mason, B. C. Buddingh', D. S. Williams, J. C. M. Van Hest, *J. Am. Chem. Soc.* **2017**, *139*, 17309–17312.
[113] Y. Elani, *Angew. Chem. Int. Ed.* **2021**, *60*, 5602–5611.
[114] S. F. Banani, H. O. Lee, A. A. Hyman, M. K. Rosen, *Nat Rev Mol Cell Biol* **2017**, *18*, 285–298.
[115] B. Wang, L. Zhang, T. Dai, Z. Qin, H. Lu, L. Zhang, F. Zhou, *Sig Transduct Target Ther* **2021**, *6*, 290.
[116] Y. Shin, C. P. Brangwynne, *Science* **2017**, *357*, eaaf4382.
[117] E. Wilson, *Science* **1899**, *10*, 33–45.
[118] C. P. Brangwynne, C. R. Eckmann, D. S. Courson, A. Rybarska, C. Hoege, J. Gharakhani, F. Jülicher, A. A. Hyman, *Science* **2009**, *324*, 1729–1732.
[119] S. Boeynaems, P. Tompa, L. Van Den Bosch, *Cell Div* **2018**, *13*, 1.

[120] C. P. Brangwynne, T. J. Mitchison, A. A. Hyman, *Proc. Natl. Acad. Sci. U.S.A.* **2011**, *108*, 4334–4339.
[121] V. N. Uversky, *Current Opinion in Structural Biology* **2017**, *44*, 18–30.
[122] P. Li, S. Banjade, H.-C. Cheng, S. Kim, B. Chen, L. Guo, M. Llaguno, J. V. Hollingsworth, D. S. King, S. F. Banani, P. S. Russo, Q.-X. Jiang, B. T. Nixon, M. K. Rosen, *Nature* **2012**, *483*, 336–340.
[123] M. Kato, T. W. Han, S. Xie, K. Shi, X. Du, L. C. Wu, H. Mirzaei, E. J. Goldsmith, J. Longgood, J. Pei, N. V. Grishin, D. E. Frantz, J. W. Schneider, S. Chen, L. Li, M. R. Sawaya, D. Eisenberg, R. Tycko, S. L. McKnight, *Cell* **2012**, *149*, 753–767.
[124] S. Boeynaems, S. Alberti, N. L. Fawzi, T. Mittag, M. Polymenidou, F. Rousseau, J. Schymkowitz, J. Shorter, B. Wolozin, L. Van Den Bosch, P. Tompa, M. Fuxreiter, *Trends in Cell Biology* **2018**, *28*, 420–435.
[125] T. M. Franzmann, M. Jahnel, A. Pozniakovsky, J. Mahamid, A. S. Holehouse, E. Nüske, D. Richter, W. Baumeister, S. W. Grill, R. V. Pappu, A. A. Hyman, S. Alberti, *Science* **2018**, *359*, eaao5654.
[126] A. Molliex, J. Temirov, J. Lee, M. Coughlin, A. P. Kanagaraj, H. J. Kim, T. Mittag, J. P. Taylor, *Cell* **2015**, *163*, 123–133.
[127] S. Wegmann, B. Eftekharzadeh, K. Tepper, K. M. Zoltowska, R. E. Bennett, S. Dujardin, P. R. Laskowski, D. MacKenzie, T. Kamath, C. Commins, C. Vanderburg, A. D. Roe, Z. Fan, A. M. Molliex, A. Hernandez-Vega, D. Muller, A. A. Hyman, E. Mandelkow, J. P. Taylor, B. T. Hyman, *The EMBO Journal* **2018**, *37*, e98049.
[128] G. Boulay, G. J. Sandoval, N. Riggi, S. Iyer, R. Buisson, B. Naigles, M. E. Awad, S. Rengarajan, A. Volorio, M. J. McBride, L. C. Broye, L. Zou, I. Stamenkovic, C. Kadoch, M. N. Rivera, *Cell* **2017**, *171*, 163-178.e19.
[129] J. J. Bouchard, J. H. Otero, D. C. Scott, E. Szulc, E. W. Martin, N. Sabri, D. Granata, M. R. Marzahn, K. Lindorff-Larsen, X. Salvatella, B. A. Schulman, T. Mittag, *Molecular Cell* **2018**, *72*, 19-36.e8.
[130] M. Feric, N. Vaidya, T. S. Harmon, D. M. Mitrea, L. Zhu, T. M. Richardson, R. W. Kriwacki, R. V. Pappu, C. P. Brangwynne, *Cell* **2016**, *165*, 1686–1697.
[131] D. T. Murray, M. Kato, Y. Lin, K. R. Thurber, I. Hung, S. L. McKnight, R. Tycko, *Cell* **2017**, *171*, 615-627.e16.
[132] F. W. Z. Tiebackx, *Chem. Ind. Kolloide* **1911**, *8*, 198–201.
[133] J. Huddleston, A. Veide, K. Köhler, J. Flanagan, S.-O. Enfors, A. Lyddiatt, *Trends in Biotechnology* **1991**, *9*, 381–388.
[134] T. Furuya, Y. Iwai, Y. Tanaka, H. Uchida, S. Yamada, Y. Arai, *Fluid Phase Equilibria* **1995**, *103*, 119–141.
[135] K. Bergfeldt, L. Piculell, P. Linse, *J. Phys. Chem.* **1996**, *100*, 3680–3687.
[136] Å. Gustafsson, H. Wennerström, F. Tjerneld, *Polymer* **1986**, *27*, 1768–1770.
[137] H.-O. Johansson, G. Karlström, F. Tjerneld, C. A. Haynes, *Journal of Chromatography B: Biomedical Sciences and Applications* **1998**, *711*, 3–17.
[138] M. S. Long, A.-S. Cans, C. D. Keating, *J. Am. Chem. Soc.* **2008**, *130*, 756–762.
[139] C. D. Crowe, C. D. Keating, *Langmuir* **2022**, *38*, 1811–1820.
[140] M. R. Helfrich, L. K. Mangeney-Slavin, M. S. Long, K. Y. Djoko, C. D. Keating, *J. Am. Chem. Soc.* **2002**, *124*, 13374–13375.
[141] C. D. Keating, *Acc. Chem. Res.* **2012**, *45*, 2114–2124.
[142] C. D. Crowe, C. D. Keating, *Interface Focus.* **2018**, *8*, 20180032.

[143] H. B. de Jong, H. R. Kruyt, *Proc. K. Ned. Akad. Wet.* **1929**, *32*, 849–856.
[144] N. Martin, *ChemBioChem* **2019**, *20*, 2553–2568.
[145] N. A. Yewdall, A. A. M. André, T. Lu, E. Spruijt, *Current Opinion in Colloid & Interface Science* **2021**, *52*, 101416.
[146] C. E. Sing, S. L. Perry, *Soft Matter* **2020**, *13*, 8368–8378.
[147] J. V. D. Gucht, E. Spruijt, M. Lemmers, M. A. Cohen Stuart, *Journal of Colloid and Interface Science* **2011**, *361*, 407–422.
[148] D. Priftis, M. Tirrell, *Soft Matter* **2012**, *8*, 9396–9405.
[149] J. R. Vieregg, M. Lueckheide, A. B. Marciel, L. Leon, A. J. Bologna, J. R. Rivera, M. V. Tirrell, *J. Am. Chem. Soc.* **2018**, *140*, 1632–1638.
[150] T.-Y. D. Tang, M. Antognozzi, J. A. Vicary, A. W. Perriman, S. Mann, *Soft Matter* **2013**, *9*, 7647.
[151] L. Faltova, A. M. Küffner, M. Hondele, K. Weis, P. Arosio, *ACS Nano* **n.d.**
[152] W. M. Aumiller, C. D. Keating, *Nature Chem* **2016**, *8*, 129–137.
[153] S. L. Perry, L. Leon, K. Q. Hoffmann, M. J. Kade, D. Priftis, K. A. Black, D. Wong, R. A. Klein, C. F. Pierce, K. O. Margossian, J. K. Whitmer, J. Qin, J. J. De Pablo, M. Tirrell, *Nat Commun* **2015**, *6*, 6052.
[154] G. Johansson, *J Chromatogr* **1978**, *150*, 63–71.
[155] Z. Lin, T. Beneyton, J. Baret, N. Martin, *Small Methods* **2023**, 2300496.
[156] A. B. Cook, S. Novosedlik, J. C. M. Van Hest, *Acc. Mater. Res.* **2023**, *4*, 287–298.
[157] R. Petitdemange, E. Garanger, L. Bataille, W. Dieryck, K. Bathany, B. Garbay, T. J. Deming, S. Lecommandoux, *Biomacromolecules* **2017**, *18*, 544–550.
[158] F. G. Quiroz, A. Chilkoti, *Nature Mater* **2015**, *14*, 1164–1171.
[159] C. W. Pak, M. Kosno, A. S. Holehouse, S. B. Padrick, A. Mittal, R. Ali, A. A. Yunus, D. R. Liu, R. V. Pappu, M. K. Rosen, *Molecular Cell* **2016**, *63*, 72–85.
[160] F. G. Quiroz, A. Chilkoti, *Nature Mater* **2015**, *14*, 1164–1171.
[161] D. E. Meyer, A. Chilkoti, *Nat Biotechnol* **1999**, *17*, 1112–1115.
[162] S. A. Costa, J. R. Simon, M. Amiram, L. Tang, S. Zauscher, E. M. Brustad, F. J. Isaacs, A. Chilkoti, *Advanced Materials* **2018**, *30*, 1704878.
[163] S. Deshpande, C. Dekker, *Current Opinion in Colloid & Interface Science* **2021**, *52*, 101419.
[164] M. Weiss, J. P. Frohnmayer, L. T. Benk, B. Haller, J.-W. Janiesch, T. Heitkamp, M. Börsch, R. B. Lira, R. Dimova, R. Lipowsky, E. Bodenschatz, J.-C. Baret, T. Vidakovic-Koch, K. Sundmacher, I. Platzman, J. P. Spatz, *Nature Mater* **2018**, *17*, 89–96.
[165] E. H. Reed, B. S. Schuster, M. C. Good, D. A. Hammer, *ACS Synth. Biol.* **2020**, *9*, 500–507.
[166] K. D. Seo, S. Shin, H. Y. Yoo, J. Cao, S. Lee, J.-W. Yoo, D. S. Kim, D. S. Hwang, *Biomacromolecules* **2020**, *21*, 930–938.
[167] J. R. Simon, S. A. Eghtesadi, M. Dzuricky, L. You, A. Chilkoti, *Molecular Cell* **2019**, *75*, 66-75.e5.
[168] Q. Zhao, F. Cao, Z. Luo, W. T. S. Huck, N. Deng, *Angew Chem Int Ed* **2022**, *61*, DOI 10.1002/anie.202117500.
[169] T. Einfalt, R. Goers, I. A. Dinu, A. Najer, M. Spulber, O. Onaca-Fischer, C. G. Palivan, *Nano Lett.* **2015**, *15*, 7596–7603.
[170] C. Nardin, S. Thoeni, J. Widmer, M. Winterhalter, W. Meier, *Chem. Commun.* **2000**, 1433–1434.

[171] L. Messager, J. R. Burns, J. Kim, D. Cecchin, J. Hindley, A. L. B. Pyne, J. Gaitzsch, G. Battaglia, S. Howorka, *Angewandte Chemie International Edition* **2016**, *55*, 11106–11109.
[172] R. Booth, Y. Qiao, M. Li, S. Mann, *Angew. Chem. Int. Ed.* **2019**, *58*, 9120–9124.
[173] J. Li, Z. Xu, M. Zhu, C. Zhao, X. Wang, H. Chen, X. Liu, L. Wang, X. Huang, *Chem* **2022**, *8*, 784–800.
[174] T. Kojima, S. Takayama, *ACS Appl. Mater. Interfaces* **2018**, *10*, 32782–32791.
[175] M. G. F. Last, S. Deshpande, C. Dekker, *ACS Nano* **2020**, *14*, 4487–4498.
[176] C. Love, J. Steinkühler, D. T. Gonzales, N. Yandrapalli, T. Robinson, R. Dimova, T. -Y. D. Tang, *Angew. Chem.* **2020**, *132*, 6006–6013.
[177] L. Song, M. R. Hobaugh, C. Shustak, S. Cheley, H. Bayley, J. E. Gouaux, *Science* **1996**, *274*, 1859–1866.
[178] N.-N. Deng, M. A. Vibhute, L. Zheng, H. Zhao, M. Yelleswarapu, W. T. S. Huck, *J. Am. Chem. Soc.* **2018**, *140*, 7399–7402.
[179] G. A. Mountain, C. D. Keating, *Biomacromolecules* **2020**, *21*, 630–640.
[180] T. Lu, E. Spruijt, *J. Am. Chem. Soc.* **2020**, *142*, 2905–2914.
[181] Y. Chen, M. Yuan, Y. Zhang, S. Liu, X. Yang, K. Wang, J. Liu, *Chem. Sci.* **2020**, *11*, 8617–8625.
[182] J. G. Gall, M. Bellini, Z. Wu, C. Murphy, *Mol Biol Cell* **1999**, *10*, 4385–4402.
[183] J. R. Simon, N. J. Carroll, M. Rubinstein, A. Chilkoti, G. P. López, *Nature Chem* **2017**, *9*, 509–515.
[184] Y. Elani, T. Trantidou, D. Wylie, L. Dekker, K. Polizzi, R. V. Law, O. Ces, *Sci Rep* **2018**, *8*, 4564.
[185] T. Trantidou, L. Dekker, K. Polizzi, O. Ces, Y. Elani, **n.d.**
[186] C. L. Cuevas-Velazquez, T. Vellosillo, K. Guadalupe, H. B. Schmidt, F. Yu, D. Moses, J. A. N. Brophy, D. Cosio-Acosta, A. Das, L. Wang, A. M. Jones, A. A. Covarrubias, S. Sukenik, J. R. Dinneny, *Nat Commun* **2021**, *12*, 5438.
[187] P. Jusková, Y. R. F. Schmid, A. Stucki, S. Schmitt, M. Held, P. S. Dittrich, *ACS Appl. Mater. Interfaces* **2019**, *11*, 34698–34706.
[188] K. Göpfrich, B. Haller, O. Staufer, Y. Dreher, U. Mersdorf, I. Platzman, J. P. Spatz, *ACS Synth. Biol.* **2019**, *8*, 937–947.
[189] B. V. V. S. Pavan Kumar, J. Fothergill, J. Bretherton, L. Tian, A. J. Patil, S. A. Davis, S. Mann, *Chem. Commun.* **2018**, *54*, 3594–3597.
[190] T. Einfalt, M. Garni, D. Witzigmann, S. Sieber, N. Baltisberger, J. Huwyler, W. Meier, C. G. Palivan, *Adv. Sci.* **2020**, *7*, 1901923.
[191] O. Staufer, M. Schröter, I. Platzman, J. P. Spatz, *Small* **2020**, *16*, 1906424.
[192] L. M. P. E. Van Oppen, L. K. E. A. Abdelmohsen, S. E. Van Emst-de Vries, P. L. W. Welzen, D. A. Wilson, J. A. M. Smeitink, W. J. H. Koopman, R. Brock, P. H. G. M. Willems, D. S. Williams, J. C. M. Van Hest, *ACS Cent. Sci.* **2018**, *4*, 917–928.
[193] N. Gao, S. Mann, *Acc. Chem. Res.* **2023**, *56*, 297–307.
[194] C. Zhao, J. Li, S. Wang, Z. Xu, X. Wang, X. Liu, L. Wang, X. Huang, *ACS Nano* **2021**, *15*, 10048–10057.
[195] S. Liu, Y. Zhang, M. Li, L. Xiong, Z. Zhang, X. Yang, X. He, K. Wang, J. Liu, S. Mann, *Nat. Chem.* **2020**, *12*, 1165–1173.
[196] X. Wang, S. Wu, T.-Y. D. Tang, L. Tian, *Trends in Chemistry* **2022**, *4*, 1106–1120.
[197] S. Mann, *Interface Focus.* **2023**, *13*, 20230034.

Chapter II - Encapsulation of synthetic membrane-bound and membraneless organelles in a cell-like chassis

1. Introduction

Constructing protocells with life-like properties has been one of the challenges of the past decades, as the first artificial cell attempt was made in 1957 by Chang.[1,2] The cell, the basic unit of life, common to any living organism, has fascinated scientists for its highly complex and multi-compartmentalized structure.[3] This feature allows eukaryotic cells to spatiotemporally control and drive key biological events without interfering with one another.[4–6] Each of these sub-compartments is an organized and specialized functional unit. Two distinct sub-compartments, called organelles in cellular biology, can be found. Membrane-bound organelles,[4][7–9] such as lysosomes and the nucleus, are self-assembled structures containing a subcellular aqueous environment surrounded by a fluidic unilamellar (phospho)lipid membrane. Membraneless organelles[10,11] like the nucleolus and P-bodies, are devoid of any lipid boundary. They have become the focus of research in cell biology since their discovery by Brangwynne et al. in 2009.[12] These compartments form through the liquid-liquid phase separation (LLPS) of RNA and intrinsically disordered proteins (IDP), under biological changes in cytoplasmic pH, temperature, and osmotic stress.[13–15] Each of these sub-compartments stores, protects, and controls the release of bio(macro)molecules through selective transport processes, crucial for the cell's development and survival. The bottom-up construction of a synthetic cell using non-living materials represents an important challenge in science and technology today. Because of their structural similarity to cell membranes, liposomes[16–23] and polymersomes[24–28] have widely been used as synthetic cell-like compartments, as well as proteinosomes,[29–31] (inorganic) colloidosomes,[32] and membrane-free coacervate microdroplets,[33–35] commonly prepared using microfluidics,[18,36] film-rehydration,[37] and emulsion-centrifugation[9], to cite a few. To further increase the complexity of these prototypes, multi-compartmentalized architectures were developed by encapsulating sub-

compartments within these larger ones. Membrane-bound encapsulated systems were for example made by encapsulating liposomes-in-liposome,[38–42], liposomes in layer-by-layer capsules,[43] polymersomes-in-polymersome,[44] capsosomes,[45–47] and liposomes-in-polymersomes.[9] Membraneless systems were made by encapsulating coacervates-in-vesicle,[36,48–51] coacervates-in-ATPS,[52,53] coacervates-in-droplet,[54–57] and coacervate-in-coacervate.[58] Chemical and biochemical components are usually integrated within these systems, capable of accomplishing increasingly intricate functions[59,60] following an external stimulus such light triggering,[57] pH,[49] temperature[54,55] and osmolarity (cite our paper) variations. A variety of cellular processes like cell division[61] and self-sustainability[62] can be achieved, the latter being the next important challenge of this field. Despite significant progress in constructing complex artificial cells, it has been observed that bottom-up constructions systematically separate the two main types of organelles, which does not accurately represent the structure and biological functioning of a cell. Zhao et al. recently reported how these condensates intimately interact in eukaryotic cells and regulate various of their activities.[63] In this study, we design a multicompartmental artificial cell chassis co-encapsulating two synthetic types of organelles in a cytoplasm-like core. We incorporate PEG_{22}-*b*-$PTMC_{51}$-Cy5.5 nanovesicles, representing membrane-bound organelles, and temperature-sensitive Elastin-Like Polypeptides (ELPs), representing membraneless organelles, into a PEG crowded lumen. ELPs are intrinsically disordered protein (IDP) models that can undergo phase separation and form coacervates in response to temperature changes. We demonstrate that the synthetic organelles coexist and perform their designated tasks within the cell-like chassis. We believe that our prototype is unique as it combines multiple vital cell components, and has the potential to pave the way for developing advanced artificial cells that emulate the behaviours of living cells.

2. Results and discussion

2.1. Formation of a cell-like chassis and assembly of synthetic membraneless organelles

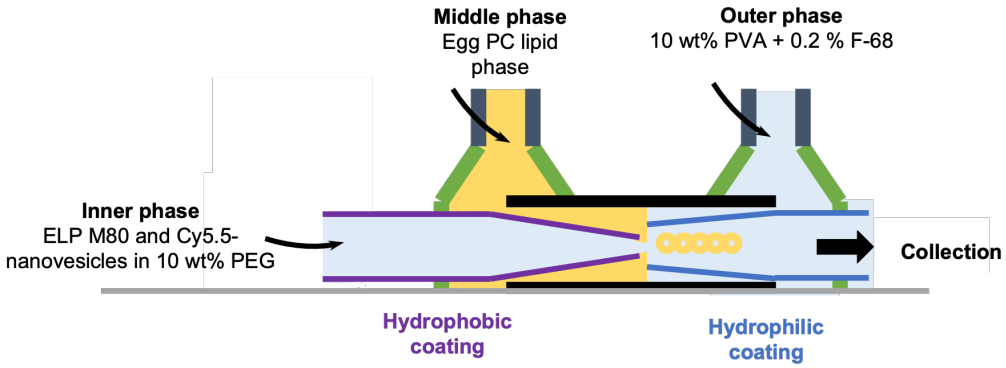

Figure 1: Water-in-oil-in-water double emulsion production using a glass capillary-based microfluidic device.

A thick-shell microfluidic system was used to generate water-in-oil-in-water double emulsions (Figure 1). Liposomes, which bear a resemblance to cellular membranes in terms of their structure, are frequently utilized to construct synthetic cell-like compartments. In this study, Egg PC lipids self-assembled to form the membrane of the liposomes, while the external phase was composed of a 0.2% Pluronic F-68 surfactant, that was added to a continuous aqueous phase of 10 wt% poly(vinyl alcohol) (PVA). By using this technique, partially dewetted liposomes were produced, as described in our prior research, which we use as an artificial cell-like chassis.

Once the liposomes were collected, a temperature-trigger was used to assemble the synthetic membraneless organelles within the crowded lumen (Figure 2a). Indeed, a methionine-containing temperature-sensitive ELP, with a primary structure of 80 repeat units of a pentapeptide presenting Val/Met as guest residues in a 3:1 ratio, was selected. The protocol for this ELP[M_1V_3-80] production was reported elsewhere. ELPs are repeat units of a Val-Pro-Gly-Xaa-Gly (VPGXG) pentapeptide sequence, produced recombinantly in *Escherichia coli* (*E. coli*) bacteria,[15] and serve as IDP models. They exhibit a lower critical solubility temperature (LCST) behaviour in water: below their cloud point temperature (T_{cp}), ELP chains are soluble in water and present random coil chains. Above their T_{cp}, they dehydrate and form ELP-rich coacervates (Figure 2b).[15-16] The T_{cp}

can be tuned by varying the nature of amino acid residues of the pentapeptide sequence, in particular at the Xaa position, the number of repeat sequences, and the ELP concentration.

To study the capacity of ELP[M1V3-80] to undergo liquid-liquid phase separation (LLPS) and assemble into membraneless organelles within partially dewetted liposomes, several ELP[M1V3-80] concentrations were encapsulated in a 8 wt% PEG solution, mimicking the macromolecular crowded environment of a cell.[18] The T_{cp} of 0.25 mg mL^{-1}, 1 mg mL^{-1}, 2 mg mL^{-1} and 3 mg mL^{-1} ELP[M_1V_3-80] was determined by Dynamic Light Scattering (DLS), each exhibiting a T_{cp} of 21°C, 18°C, 15°C and 7°C respectively (Figure 2c). It could be noted that the T_{cp} was inversely proportional to their concentration in the solution (Figure 2d).

Each of these ELP[M_1V_3-80] solutions was then encapsulated within the partially dewetted liposomes, and their phase separation was induced. Higher concentrations of the proteins made the membraneless organelles much bigger, contrasted, and easier to observe (Figure 2g,h), but their low T_{cp} was a limit to conducting the experiments. On the contrary, 0.25 mg mL^{-1} concentration was too low to distinctly observe the phase separation of the ELP[M_1V_3-80] within the vesicles (Figure 2e). The 1 mg mL^{-1} ELP concentration (Figure 2f) was a good compromise as the artificial membraneless organelles were still quite distinct within the lumen under the confocal microscope, with a high enough T_{cp} to experimentally control the phase separation of the ELP[M_1V_3-80]. Temperature-trigger was hence used to induce the LLPS of 1 mg mL^{-1} ELP[M_1V_3-80] within the lumen of the liposomes. By tuning the temperature of the sample, the state of the ELP could be controlled, transiting from a liquid phase when the temperature of the sample was below the T_{cp}, to an aggregated state when heating the sample above the T_{cp} of the ELP.

In Figure 2i, a ramp temperature from 10°C to 25°C was applied to a sample of partially dewetted microdroplets encapsulating 1 mg mL^{-1} ELP[M_1V_3-80]. At 10°C and 15°C, the solution inside the lumen of the vesicle was translucid; no organelles were formed (Figure 2i_{1-2}). As the temperature of the sample reached 19°C, slightly above the T_{cp} of the system, the phase separation and assembly of the membraneless organelles slowly appeared (Figure 2i_3). This phenomenon is completed and intensified at 25°C (Figure 2i_4, SI 1), denoted by the numerous black spots inside the liposomes. Furtherly, the reversibility of the process was investigated. As the sample was cooled below the T_{cp}, fewer organelles were present within the liposomes as ELPs returned to their liquid state (Figure 2i_5). Their complete disappearance, denoted by the lack of black spots in the artificial cytoplasm, was seen at 10°C (Figure 2i_6).

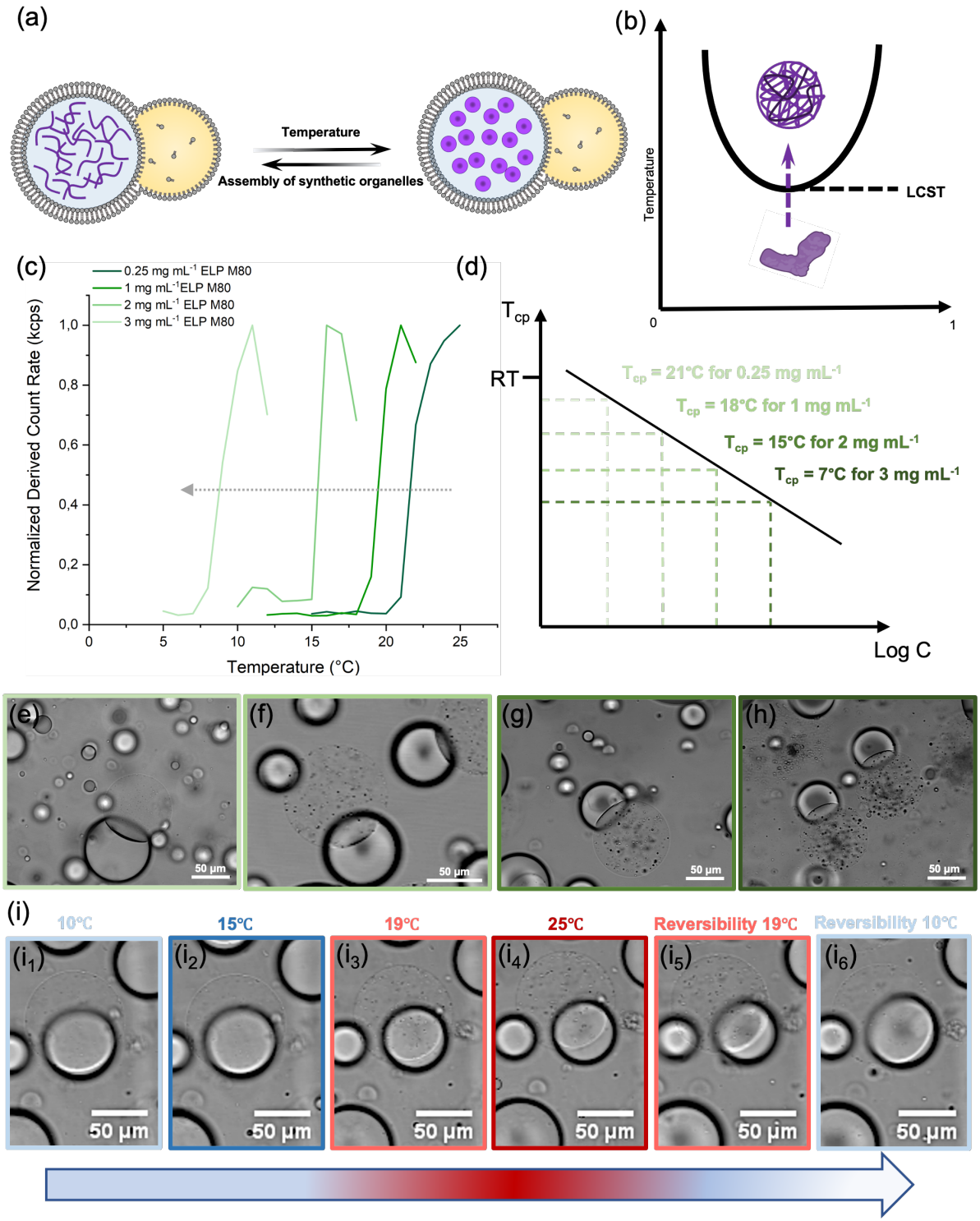

Figure 2: Temperature-triggered assembly of synthetic organelles within partially dewetted liposomes. a) Schematic illustration of ELP[M_1V_3-80] synthetic organelles assembly inside cytomimetic lipid compartments in response to temperature trigger b) Schematic phase diagram of ELP phase separation c) DLS analysis (measurement of the scattered light intensity, also referred to as the normalized derived count rate, DCR) to determine the T_{cp} of 0.25 mg mL^{-1}, 1 mg

mL^{-1}, 2 mg mL^{-1} and 3 mg mL^{-1} ELP[M_1V_3-80]in a cell-like crowded environment d) Schematic illustration of the ELP[M_1V_3-80] T_{cp} evolution as a function of concentration e-h) Confocal images of partially dewetted liposomes encapsulating 0.25 mg mL^{-1}, 1 mg mL^{-1}, 2 mg mL^{-1} and 3 mg mL^{-1} of ELP[M_1V_3-80] respectively, in their phase separated state i_{1-6}) Confocal images of partially dewetted liposomes encapsulating 1 mg mL^{-1} ELP[M_1V_3-80]. A temperature ramp is exerted onto the sample from 10°C to 25°C. The apparition of synthetic membraneless organelles is denoted by the black dots in the vesicles. A reverse temperature ramp is then applied from 25°C to 10°C.

2.2. Synthetic membrane-bound organelles in partially dewetted vesicles

Synthetic membrane-bound organelles were mimicked using Cy5.5-tagged PEG_{22}-*b*-$PTMC_{51}$ vesicles, which were produced using a dolomite microfluidic system. 0.20 mg mL^{-1} of these nanovesicles were dissolved in a 10 wt% PEG solution and encapsulated within partially dewetted liposomes using the thick-shell microfluidic system (Figure 1 and 4a). These systems were homogeneously spread within the partially dewetted liposomes, as observed using the confocal microscope (Figure 4b and 4c).

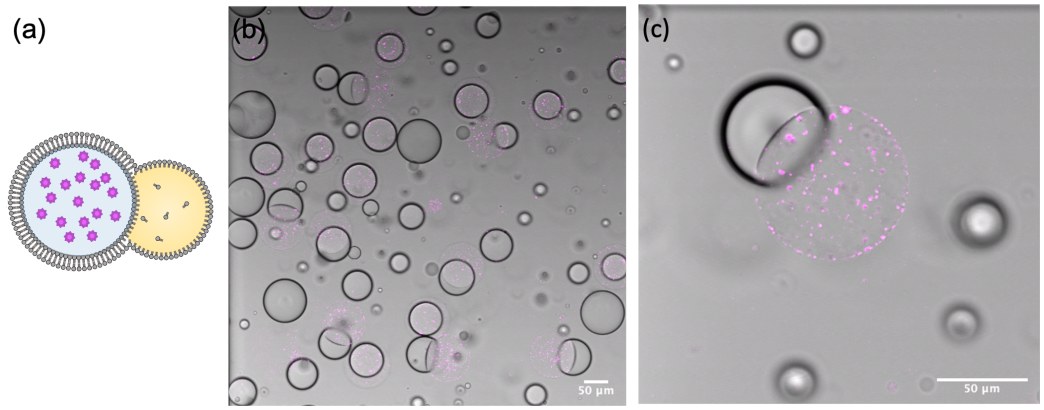

Figure 4: Encapsulation of Cy5.5-tagged PEG_{22}-b-$PTMC_{51}$ nanovesicles in partially dewetted microdroplets. (a) Scheme illustration of PEG_{22}-b-$PTMC_{51}$-Cy5.5 nanovesicles denoted by the pink stars encapsulated in partially dewetted vesicles. (b) Overview and (c) zoom of microdroplets embedding Cy5.5-tagged PEG_{22}-b-$PTMC_{51}$ nanovesicles in a 10 wt% PEG solution.

2.3. Co-encapsulation of membrane-bound and membraneless organelles

The co-encapsulation of the two previously described synthetic organelles within a same vesicle was performed. 1 mg mL^{-1} of ELP[M1V3-80] was enclosed with 0.20 mg mL^{-1} of PEG_{22}-*b*-$PTMC_{51}$-Cya5.5 nanovesicles, in a 8 wt% PEG solution. Temperature was used as described earlier, to trigger the phase-separation of ELP[M1V3-80] and assemble the synthetic membraneless organelles (Figure 5a). A ramp temperature was performed from 10°C to 25°C upon the vesicles (SI 2). At 10°C and 15°C, only the Cy5.5-tagged nanovesicles were observed within the liposomes, as the experiments were carried below the T_{cp} of the ELPs. Hence, no phase separation of the ELP[M1V3-80] occurred. (Figure $5b_{1\text{-}2}$). As the experimental temperature increased and crossed the T_{cp} of the ELP[M1V3-80], the assembly of the membraneless organelles was observed, as dark black spots started to appear in the lumen (Figure $5b_3$), until full completion at 25°C (Figure $5b_4$, SI 3). The phenomenon was reversible as the heating stage was cooled to 10°C (Figure $5b_{5\text{-}6}$). The membraneless organelles went back to their liquid state, only the nanovesicles remained. However, it was observed that the nanovesicles dropped to the bottom of the partially dewetted liposomes during the experiment, as it can be seen in the z-stack reconstruction of the vesicles (SI 4). The heating and cooling processes did not have any impact upon the nanovesicles structures.

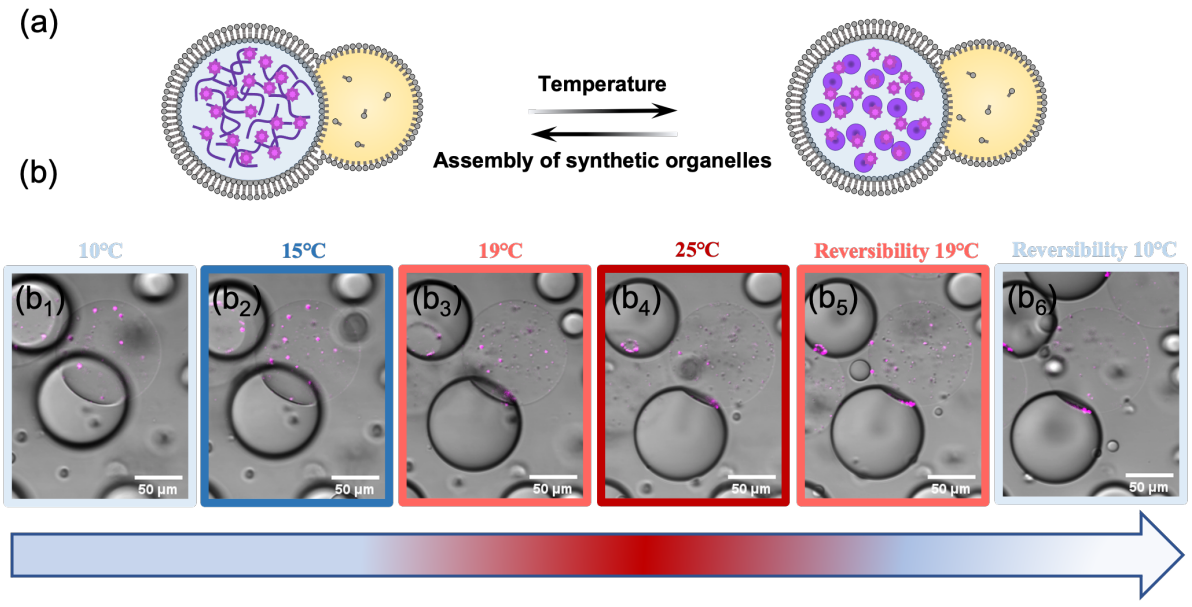

Figure 5: Encapsulation of membranebound and membraneless synthetic organelles (a) Scheme illustration of vesicles encapsulating Cy5.5-tagged PEG_{22}-b-$PTMC_{51}$ nanovesicles and ELP[M1V3-80] before and after undergoing a phase separation as the T_{cp} is crossed. (b) Temperature ramp exerted on a sample of partially dewetted microdroplets. The presence of of PEG_{22}-b-$PTMC_{51}$-Cy5.5 organelles with membrane is denoted by the pink dots. The self-assembly and dismantling of ELP[M1V3-80] membraneless organelles is denoted by the black dots.

3. Conclusion

To conclude, we have demonstrated that it is feasible to co-encapsulate two primary components of eukaryotic cells using a microfluidic system. These components can co-exist without interfering, as the presence of membrane-bound organelles did not hinder the LLPS and coacervation of ELP[M1V3-80] as a model of membraneless organelle These last ELP[M1V3-80] organelles can dynamically assemble and disassemble in the presence of PEG_{22}-*b*-$PTMC_{51}$ polymersomes. This breakthrough creates exciting opportunities for developing artificial cells from the bottom-up assembly and for exploring novel functions and interactions between these two types of organelles, much like a natural eukaryotic cell would do.

4. Materials and Methods

Materials: Poly(ethylene glycol) (PEG, 6 kDa) polymer was purchased from Alfa Aesar. Poly(vinyl alcohol) (PVA, 13-23 kDa, 87-89% hydrolyzed) polymer was obtained from Sigma-Aldrich. L-α-phosphatidylcholine (Egg PC, 25 mg ml^{-1} in chloroform) was bought from Avanti Polar Lipids. Pluronic® F-68 was obtained from Gibco. All compounds were used without further purification. The following solvents were purchased from Sigma-Aldrich and used without further purification: chloroform (anhydrous, 99%), hexane (anhydrous, 95%), dimethyl sulfoxide (DMSO, 99.9%). Acetone was purchased from VWR. Water with a resistivity of 18.2 MΩ cm^{-1} was prepared using a Millipore Milli-Q system.

Microfluidics: The protocol to make the microfluidics device can be found elsewhere.[64]

Formation of double emulsion microdroplets: The protocol describing the formation of double emulsion microdroplets can be found here.[64] Briefly, to encapsulate two types of organelles in

water-in-oil-in-water double-emulsion microdroplets, an aqueous 8 wt% PEG phase containing 1 mg mL^{-1} of ELP[M1V3-80] and 0.20 mg mL^{-1} of Cy5.5-tagged PEG_{22}-*b*-$PTMC_{51}$ nanovesicles was flowed in the injection capillary as the innermost solution. An organic mix of chloroform and hexane (36:64 vol%) containing 5 mg mL^{-1} of Egg PC was used as the middle phase and was injected through the interstices between the injection and square capillaries. The continuous phase of 8 wt% PVA with 0.2% F-68 was pumped through the interstices between the collection and square capillaries.

Bioproduction, isolation and purification of ELP[M_1V_3-80]: ELP[M_1V_3-80] was produced by recombinant DNA and protein engineering techniques in *E. coli* and isolated using previously reported procedures.[65]

Confocal microscopy imaging: Microdroplets were collected on a glass slide with a single cavity and sealed using a coverslip for the dewetting process to take place. 10 µl of vesicles were then injected into an imaging chamber (Ibidi GmbH, Germany). Images and videos were acquired by a confocal laser scanning microscopy (Leica, SP5 AOBS) through an HCX PL APO 10× dry objective. To assess the spatial distribution of Cy5.5-tagged PEG_{22}-*b*-$PTMC_{51}$ nanovesicles inside the partially dewetted microdroplets, a helium-neon diode laser (633 nm) was used to excite the Cy5.5. To observe and monitor the assembly of membraneless organelles, ramp temperatures were performed from 10°C to 25°C under the bright field mode.

Determination of transition temperature (T_{cp}) of several ELP[M1V3-80] concentrations by dynamic light scattering (DLS): To determine the cloud point temperatures of 0.25 mg mL^{-1}, 1 mg mL^{-1}, 2 mg mL^{-1} and 3 mg mL^{-1} ELP[M1V3-80] in a 8 wt% PEG solution, the protocol described in [ref paper] was followed. Temperature ramps were performed from 5 °C to 50 °C for all conditions.

PEG_{22}-b-PTMC51-Cy5.5 synthesis and characterization: The protocol to synthesize and characterize PEG_{22}-*b*-PTMC51-Cy5.5 can be found elsewhere[66]

Cy5.5-tagged PEG_{22}-b-$PTMC_{51}$ nanovesicles formation and characterization: A dolomite microfluidic system was used to induce the microfluidic assisted self-assembly of PEG_{22}-*b*-PTMC51-Cy5.5. The system was composed of two Mitos pressure pumps (3200175) equipped with flowmeters (3200097), allowing flows to run in a micromixer chip of twelve mixing stages (3200401). Pumps and chip were connected with fluorinated ethylene propylene tubing (1/16" x 0.25mm, 3200063). All DMSO solutions were filtered with polytetrafluoroethylene (PTFE) syringe filter 0.45 µm, and aqueous solutions were filtered with cellulose acetate (CA) syringe filters 0.22 µm. To avoid dust entering the chip, filters were connected to the pump outlets, between the pumps and the chip. The pump containing the organic solution was fixed to the first and third inputs using a T-connector. The aqueous solvent pump was connected to the second input of the chip. A camera was used to ensure that the chip was dust and air bubble free before sample production. Flow rates were controlled using the Mitos Flow Control Center 2.5.17 software. As water is already a solvent entered in the software, water calibration was used. For organic solvent such as DMSO and acetone, calibrations were performed. Self-assembly was performed as follow: 10 mg mL^{-1} of PEG_{22}-*b*-$PTMC_{51}$ was dissolved in DMSO with 2 wt% of PEG_{22}-*b*-$PTMC_{51}$-Cy5.5. Ratios of solvent running into the microfluidic chip were 20/80 vol% organic/aqueous and 50/50 vol%, with the aqueous solvent being osmosed water. The total flow rate was of 1000 µL min^{-1}. After microfluidics, dynamic light scattering (DLS) measurements were performed on Nano-SZ-90 instrument (Malvern U.K.) at a 90° angle, running 5 measurements of 8 runs of 8 s. D_H and PDI were calculated from autocorrelation functions using cumulant methods and were averaged. Samples were dialyzed against water for 24 h, 3 baths of 2 L each using a 25 kDa pre-wetted dialysis membrane. DLS 90°C were done the same way as previously reported after samples were filtrated with a 0.45 µm cellulose acetate syringe filter.

Funding sources

ITN MARIE CURIE PROJECT

This project has received funding from the European Union's Horizon 2020 research and innovation program under the Marie Skłodowska-Curie Grant Agreement N° 859416

5. Supporting information

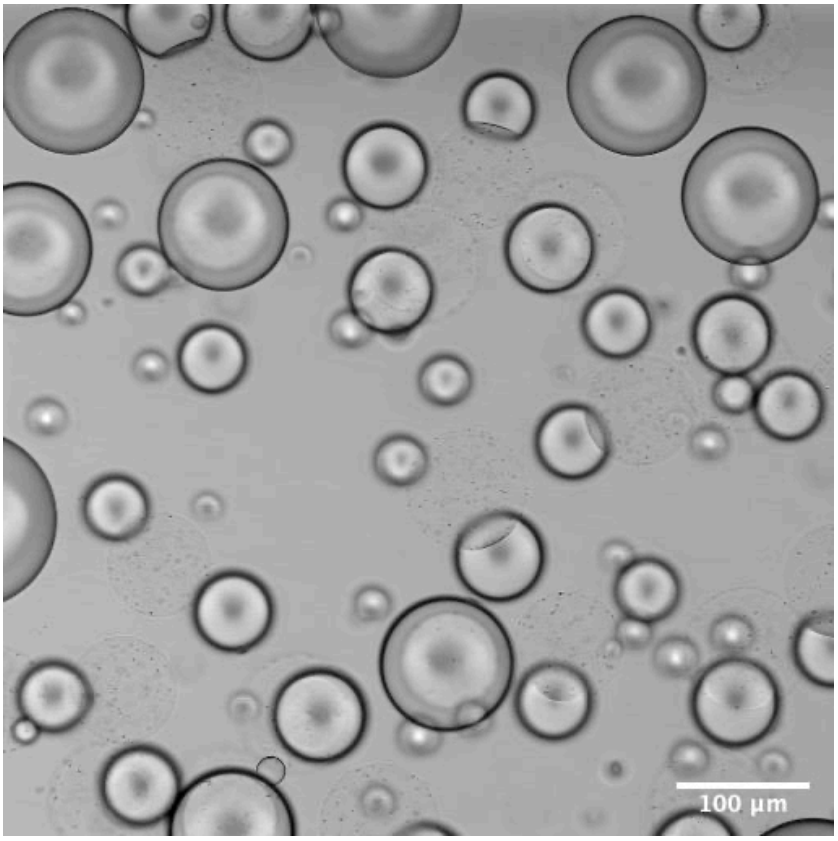

Supporting information 1: Video of synthetic membraneless organelles assembled within partially dewetted microdroplets taken under confocal microscope in the bright field mode. Plate heater set at 25°C.

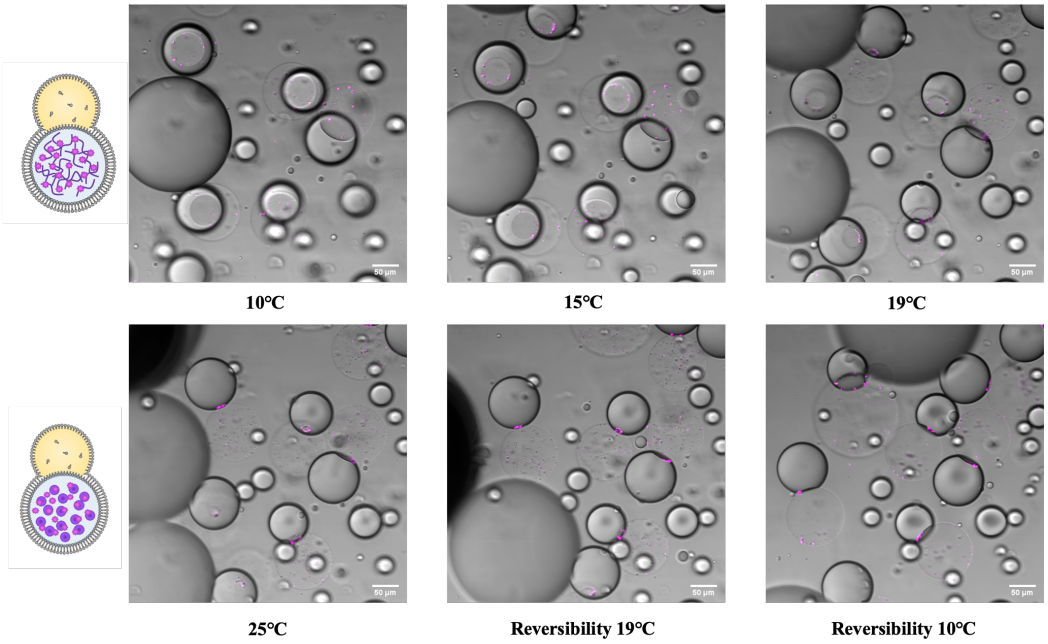

Supporting information 2: Overview of the sample where Figure 5b$_{1-6}$ was extracted from. Plate heater set at 25°C.

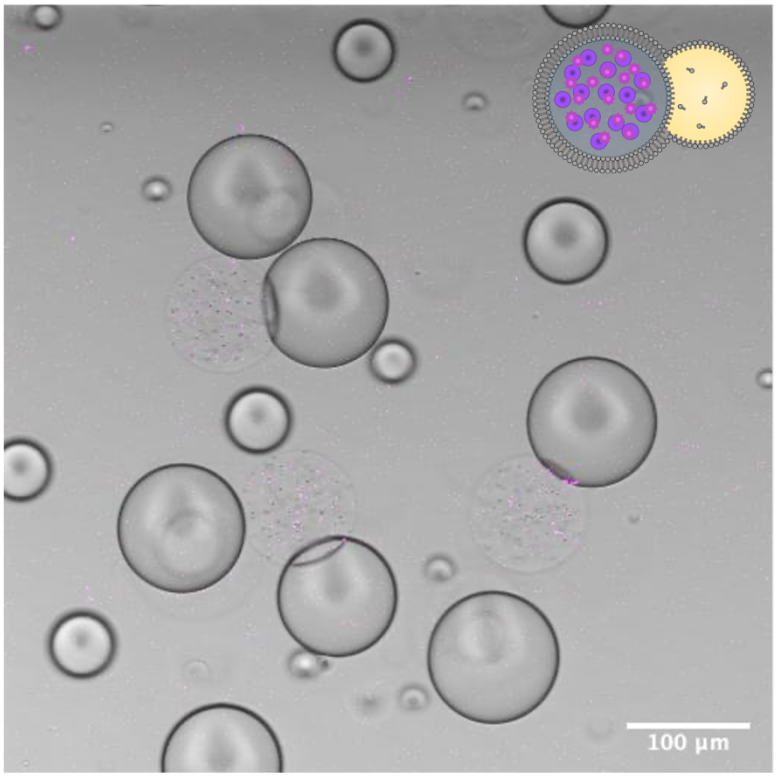

Supporting information 3: Video of Cy5.5-tagged PEG$_{22}$-b-PTMC$_{51}$ nanovesicles encapsulated with phase separated ELP[M1V3-80] inside of partially dewetted vesicles. Video was taken at 25°C under the bright field mode.

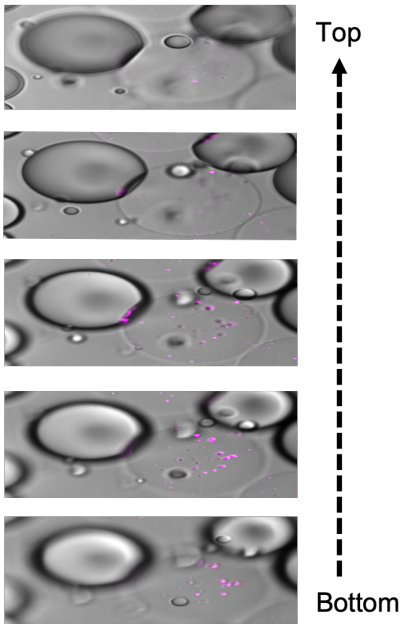

Supporting information 4: Bottom-up view of the inside of a partially dewetted liposome, where it can be observed that the Cy5.5-tagged nanovesicles dropped to the bottom of the vesicle.

6. References

[1] T. M. S. Chang, *Science* **1964**, *146*, 524–525.
[2] T. M. S. Chang, *Report of a research project for the BSc Honours, McGill University* **1957**.
[3] J. W. Szostak, D. P. Bartel, P. L. Luisi, **2001**, *409*.
[4] M. Marguet, C. Bonduelle, S. Lecommandoux, *Chem. Soc. Rev.* **2013**, *42*, 512–529.
[5] R. Roodbeen, J. C. M. Van Hest, *BioEssays* **2009**, *31*, 1299–1308.
[6] P. A. Beales, B. Ciani, S. Mann, *Interface Focus.* **2018**, *8*, 20180046.
[7] R. J. R. W. Peters, M. Marguet, S. Marais, M. W. Fraaije, J. C. M. van Hest, S. Lecommandoux, *Angew. Chem. Int. Ed.* **2014**, *53*, 146–150.
[8] P.-Y. Bolinger, D. Stamou, H. Vogel, *Angewandte Chemie International Edition* **2008**, *47*, 5544–5549.
[9] A. Peyret, E. Ibarboure, N. Pippa, S. Lecommandoux, *Langmuir* **2017**, *33*, 7079–7085.
[10] W. Mu, Z. Ji, M. Zhou, J. Wu, Y. Lin, Y. Qiao, *Sci. Adv.* **2021**, *7*, eabf9000.
[11] N. G. Moreau, N. Martin, P. Gobbo, T.-Y. D. Tang, S. Mann, *Chem. Commun.* **2020**, *56*, 12717–12720.
[12] C. P. Brangwynne, C. R. Eckmann, D. S. Courson, A. Rybarska, C. Hoege, J. Gharakhani, F. Jülicher, A. A. Hyman, *Science* **2009**, *324*, 1729–1732.

[13] A. A. Hyman, C. A. Weber, F. Jülicher, *Annu. Rev. Cell Dev. Biol.* **2014**, *30*, 39–58.
[14] S. F. Banani, H. O. Lee, A. A. Hyman, M. K. Rosen, *Nat Rev Mol Cell Biol* **2017**, *18*, 285–298.
[15] D. Bracha, M. T. Walls, C. P. Brangwynne, *Nat Biotechnol* **2019**, *37*, 1435–1445.
[16] Y. Elani, R. V. Law, O. Ces, *Nat Commun* **2014**, *5*, 5305.
[17] P. Walde, K. Cosentino, H. Engel, P. Stano, *Chem. Eur. J. of Chem. Bio.* **2010**, *11*, 848–865.
[18] M. Weiss, J. P. Frohnmayer, L. T. Benk, B. Haller, J.-W. Janiesch, T. Heitkamp, M. Börsch, R. B. Lira, R. Dimova, R. Lipowsky, E. Bodenschatz, J.-C. Baret, T. Vidakovic-Koch, K. Sundmacher, I. Platzman, J. P. Spatz, *Nature Mater* **2018**, *17*, 89–96.
[19] T. F. Zhu, J. W. Szostak, *J. Am. Chem. Soc.* **2009**, *131*, 5705–5713.
[20] W. Zong, S. Ma, X. Zhang, X. Wang, Q. Li, X. Han, *J. Am. Chem. Soc.* **2017**, *139*, 9955–9960.
[21] X. Wang, L. Tian, Y. Ren, Z. Zhao, H. Du, Z. Zhang, B. W. Drinkwater, S. Mann, X. Han, *Small* **2020**, *16*, 1906394.
[22] X. Wang, L. Tian, H. Du, M. Li, W. Mu, B. W. Drinkwater, X. Han, S. Mann, *Chem. Sci.* **2019**, *10*, 9446–9453.
[23] K. Kurihara, Y. Okura, M. Matsuo, T. Toyota, K. Suzuki, T. Sugawara, *Nat Commun* **2015**, *6*, 8352.
[24] H. Che, S. Cao, J. C. M. van Hest, *J. Am. Chem. Soc.* **2018**, *140*, 5356–5359.
[25] N. P. Kamat, J. S. Katz, D. A. Hammer, *J. Phys. Chem. Lett.* **2011**, *2*, 1612–1623.
[26] W. Jiang, Y. Zhou, D. Yan, *Chem. Soc. Rev.* **2015**, *44*, 3874–3889.
[27] C. LoPresti, H. Lomas, M. Massignani, T. Smart, G. Battaglia, *J. Mater. Chem.* **2009**, *19*, 3576.
[28] R. S. M. Rikken, H. Engelkamp, R. J. M. Nolte, J. C. Maan, J. C. M. van Hest, D. A. Wilson, P. C. M. Christianen, *Nat Commun* **2016**, *7*, 12606.
[29] S. Matoori, J.-C. Leroux, *Mater. Horiz.* **2020**, *7*, 1297–1309.
[30] X. Huang, M. Li, D. C. Green, D. S. Williams, A. J. Patil, S. Mann, *Nat Commun* **2013**, *4*, 2239.
[31] X. Huang, A. J. Patil, M. Li, S. Mann, *J. Am. Chem. Soc.* **2014**, *136*, 9225–9234.
[32] M. Li, R. L. Harbron, J. V. M. Weaver, B. P. Binks, S. Mann, *Nature Chem* **2013**, *5*, 529–536.
[33] L. Tian, N. Martin, P. G. Bassindale, A. J. Patil, M. Li, A. Barnes, B. W. Drinkwater, S. Mann, *Nat Commun* **2016**, *7*, 13068.
[34] S. Koga, D. S. Williams, A. W. Perriman, S. Mann, *Nature Chem* **2011**, *3*, 720–724.
[35] W. M. Aumiller, C. D. Keating, *Nature Chem* **2016**, *8*, 129–137.
[36] N. Deng, W. T. S. Huck, *Angew. Chem. Int. Ed.* **2017**, *56*, 9736–9740.
[37] A. Belluati, S. Thamboo, A. Najer, V. Maffeis, C. Planta, I. Craciun, C. G. Palivan, W. Meier, *Adv. Funct. Mater.* **2020**, *30*, 2002949.
[38] J. W. Hindley, D. G. Zheleva, Y. Elani, K. Charalambous, L. M. C. Barter, P. J. Booth, C. L. Bevan, R. V. Law, O. Ces, *Proc. Natl. Acad. Sci. U.S.A.* **2019**, *116*, 16711–16716.
[39] N.-N. Deng, M. Yelleswarapu, L. Zheng, W. T. S. Huck, *J. Am. Chem. Soc.* **2017**, *139*, 587–590.
[40] C. Boyer, J. A. Zasadzinski, *ACS Nano* **2007**, *1*, 176–182.
[41] S. Li, X. Wang, W. Mu, X. Han, *Anal. Chem.* **2019**, *91*, 6859–6864.

[42] J. W. Hindley, Y. Elani, C. M. McGilvery, S. Ali, C. L. Bevan, R. V. Law, O. Ces, *Nat Commun* **2018**, *9*, 1093.
[43] O. Kreft, M. Prevot, H. Möhwald, G. B. Sukhorukov, *Angew. Chem. Int. Ed.* **2007**, *46*, 5605–5608.
[44] M. Marguet, L. Edembe, S. Lecommandoux, *Angew. Chem.* **2012**, *124*, 1199–1202.
[45] B. Städler, R. Chandrawati, K. Goldie, F. Caruso, *Langmuir* **2009**, *25*, 6725–6732.
[46] X. Huang, B. Voit, *Polym. Chem.* **2013**, *4*, 435–443.
[47] J. W. Maina, J. J. Richardson, R. Chandrawati, K. Kempe, M. P. Van Koeverden, F. Caruso, *Langmuir* **2015**, *31*, 7776–7781.
[48] D. Garenne, L. Beven, L. Navailles, F. Nallet, E. J. Dufourc, J.-P. Douliez, *Angew. Chem.* **2016**, *128*, 13673–13677.
[49] C. Love, J. Steinkühler, D. T. Gonzales, N. Yandrapalli, T. Robinson, R. Dimova, T. -Y. D. Tang, *Angew. Chem.* **2020**, *132*, 6006–6013.
[50] S. Deshpande, F. Brandenburg, A. Lau, M. G. F. Last, W. K. Spoelstra, L. Reese, S. Wunnava, M. Dogterom, C. Dekker, *Nat Commun* **2019**, *10*, 1800.
[51] M. G. F. Last, S. Deshpande, C. Dekker, *ACS Nano* **2020**, *14*, 4487–4498.
[52] T. Kojima, S. Takayama, *ACS Appl. Mater. Interfaces* **2018**, *10*, 32782–32791.
[53] J. Li, Z. Xu, M. Zhu, C. Zhao, X. Wang, H. Chen, X. Liu, L. Wang, X. Huang, *Chem* **2022**, *8*, 784–800.
[54] H. Zhao, E. Ibarboure, V. Ibrahimova, Y. Xiao, E. Garanger, S. Lecommandoux, *Advanced Science* **2021**, *8*, 2102508.
[55] H. Zhao, V. Ibrahimova, E. Garanger, S. Lecommandoux, *Angew. Chem. Int. Ed.* **2020**, *59*, 11028–11036.
[56] R. Booth, Y. Qiao, M. Li, S. Mann, *Angew. Chem. Int. Ed.* **2019**, *58*, 9120–9124.
[57] Q. Zhao, F. Cao, Z. Luo, W. T. S. Huck, N. Deng, *Angew Chem Int Ed* **2022**, *61*, DOI 10.1002/anie.202117500.
[58] Y. Chen, M. Yuan, Y. Zhang, S. Liu, X. Yang, K. Wang, J. Liu, *Chem. Sci.* **2020**, *11*, 8617–8625.
[59] C. Wang, J. Yang, Y. Lu, *Front. Mol. Biosci.* **2021**, *8*, 781986.
[60] C. Guindani, L. C. Da Silva, S. Cao, T. Ivanov, K. Landfester, *Angew Chem Int Ed* **2022**, *61*, DOI 10.1002/anie.202110855.
[61] M.-Y. Chang, H. Ariyama, W. T. S. Huck, N.-N. Deng, *Chem. Soc. Rev.* **2023**, 10.1039.D2CS00985D.
[62] X. Wang, S. Wu, T.-Y. D. Tang, L. Tian, *Trends in Chemistry* **2022**, *4*, 1106–1120.
[63] Y. G. Zhao, H. Zhang, *Developmental Cell* **2020**, *55*, 30–44.
[64] C. Schvartzman, H. Zhao, E. Ibarboure, V. Ibrahimova, E. Garanger, S. Lecommandoux, *Advanced Materials* **2023**, 2301856.
[65] R. Petitdemange, E. Garanger, L. Bataille, K. Bathany, B. Garbay, T. J. Deming, S. Lecommandoux, *Biomacromolecules* **2017**, *18*, 544.
[66] C. Lebleu, Polymersomes Based on PEG-b-PTMC towards Cell-Mediated Delivery of Nanomedicines, Bordeaux, **2019**.
[67] R. Petitdemange, Chemoselective Modifications of Recombinant Elastin-like Polypeptides: Tuning Thermosensitivity and Bioactivity, Bordeaux, **2016**.
[68] J. R. Kramer, R. Petitdemange, L. Bataille, K. Bathany, A.-L. Wirotius, B. Garbay, T. J. Deming, E. Garanger, S. Lecommandoux, *ACS Macro Lett.* **2015**, *4*, 1283–1286.

Chapter III - Control of Enzyme Reactivity in Response to Osmotic Pressure Modulation Mimicking Dynamic Assembly of Intracellular Organelles

1. Introduction

The cell is the common basic structural and functional unit of every living organism and has fascinated the scientific world for centuries due to its highly complex and multi-compartmentalized structure.[1] Through compartmentalization, cells segregate bio(macro)molecules and control their exchange through selective transport processes, allowing them to modulate the metabolic reactions in time and space that are essential for their function and survival. Each sub-compartment can perform a specific activity without interfering with each other, providing the cell with the unique ability to produce and degrade simultaneously different essential components.[2] Particularly in eukaryotic cells, two distinct types of sub-compartments, called organelles in cellular biology, can be found: one is a subcellular aqueous environment surrounded by a fluidic unilamellar lipid membrane (*e.g.* endosomes, liposomes),[3] while the other is devoid of a lipid boundary and defined as membraneless organelle.[4] The discovery by Brangwynne and co-workers in 2009 of these membraneless organelles has opened a new field of study in cell biology.[5] The existence of membraneless organelles, known as P granules, was evidenced by the interactions between RNA and protein-containing bodies in embryo through a process of liquid-liquid phase separation (LLPS), showing liquid-like characteristics of fusion, dripping and wetting.[5] The underlying mechanism of membrane-free organelle assembly in living cells was associated to the LLPS of RNA and intrinsically disordered proteins (IDPs) under biological signals, such as changes in cytoplasmic pH, temperature, and osmotic stress.[6] These organelles are consequently able of selective sequestration of biomolecules and catalytic activity, allowing more dynamic and facilitated exchanges with their environment thanks to their lack of membrane.[7] Among biological signals, hyperosmotic stress is a ubiquitous environmental fluctuation in cells, as the number of dissolved molecules in the extracellular environment changes

regularly.[8] When subjected to hyperosmotic stress, cells rapidly adapt to volume reduction and simultaneously concentrate internal biomolecules, which can promote the assembly of membraneless organelles capable of guiding and controlling biological responses at the cellular level, which are closely related to neurodegenerative disorders, viral infections, cancers and age-related disorders.[9]

Over the past decade, scientists have made tremendous progress in building, from a bottom-up approach, complex multicompartmental artificial cells as compartments and primitive cells, in order to unveil the origins of life and the mechanisms behind these highly sophisticated systems.[3a, 4b, 10] To understand the assembly of the aforementioned structures and their importance in the proper functioning of natural cells, some research has been carried out to build artificial structures of organelles-in-cells to observe how they assemble, respond to different stimuli and influence the distribution and reactions of biomolecules.[10b, g, 11] However, most of the reported stimuli for organelle assembly so far have generally been easily controlled inducers, such as temperature and electrostatic interactions, and not always biologically relevant. To date, the design of biomimetic systems of biocatalytic membraneless organelles from the LLPS of stimuli-responsive biological materials in artificial cells *via* hyperosmotic stress has not yet been achieved.

To tackle this challenge, hyperosmotic modulation was chosen as a biologically relevant stimulus for our cytomimetic cellular assemblies. Following a hypertonic shock, we demonstrated the capacity of partially dewetted lipid vesicles to shrink and induce the assembly of synthetic organelles in their crowded lumen. These synthetic organelles resulted from the assembly of specifically designed elastin-like polypeptide (ELP) conjugates where ELP serves as an IDP model and are either ELP-polymer conjugates or ELP-enzyme conjugates. Horseradish peroxidase (HRP) was selected as a model enzyme because it readily catalyzes the oxidation of amplex red by hydrogen peroxide (H_2O_2) to fluorescent resorufin, allowing easy monitoring of the reaction kinetics. Our approach has the advantage to be applied in isothermal conditions, avoiding possible artifacts due to temperature change and circumventing any disruption of biological components. We believe our system represents a unique prototype to understand the capacity of cells to respond to osmotic variations, the importance of membraneless organelles towards the activity of cells and the sequestration of biomolecules, and will help to further understand the mechanisms leading to disruptions in LLPS processes.

2. Results and Discussion

2.1. Formation of partially dewetted lipid vesicles and synthetic organelles

Lipid vesicles have been extensively exploited as simplified bottom-up artificial chassis towards cell mimicking.[12] Despite the similarity in their bilayer composition and compartmentalization with those of living cells, lipid vesicles exhibit extremely uncontrollable stability and deformation under hyperosmotic stress, which impairs the accurate estimation of encapsulated components in shrunken vesicles.[13] To this end, we developed liposomes with an attached oil pocket that acts as a lipid reservoir to adjust the volume of the artificial cell compartment, allowing us to study the dynamic process of intracellular LLPS induced by hypertonicity inside these synthetic liposome-based cells.[14] To form the cytomimetic protocellular models, water-in-oil-in-water (W/O/W) double emulsions were prepared using a glass capillary-based microfluidic device (**Figure 1**a). The membranes of liposomes were made from self-assembled Egg PC lipids. To achieve the partially dewetted configuration of as-formed liposomes, 0.2% Pluronic F-68 surfactant was added to the continuous aqueous phase composed of 10 wt% poly(vinyl alcohol) (PVA). This helped to tune and minimize the total interfacial energies between the oil and the external aqueous medium.[10b] Consequently, the oil phase underwent dewetting, but partially remained attached to the vesicles, creating a lipid reservoir that will prevent the vesicles from wildly deforming after an applied hypertonic shock (Figure 1b). As such, stable and partially dewetted liposomes could be observed 15 min after their collection, as seen in Figure 1c.

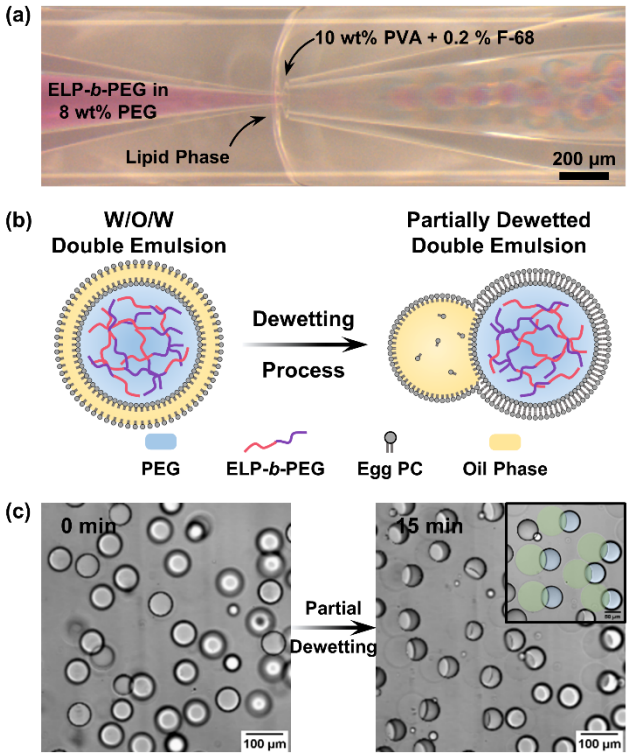

Figure 1: Preparation of W/O/W microdroplet-templated partially dewetted liposomes. (a) Optical image of microfluidic preparation of W/O/W double emulsion microdroplets. (b) Schematic illustration of the transformation of as-formed microdroplets to partially dewetted liposomes. (c) Bright field images observed at t = 0 min showing the freshly collected double emulsion microdroplets, and at t = 15 min revealing the partially dewetted liposomes. Inset: lipid reservoirs are false colored in blue and the lipid vesicles in green. Scale bars denote 100 µm.

To implement the hypertonicity-induced assembly of synthetic organelles within partially dewetted liposomes, a thermosensitive elastin-like polypeptide (ELP) was selected as a core component, which has emerged as a building block to form membraneless organelles mimicking IDPs.[10d, 11a] ELPs are composed of repeating units of a Val-Pro-Gly-Xaa-Gly (VPGXG) pentapeptide sequence and are produced recombinantly in *Escherichia coli* (*E. coli*) bacteria.[15] ELPs exhibit a lower critical solubility temperature (LCST) behavior in water: below their cloud point temperature (T_{cp}), ELP chains are soluble in water, and above the T_{cp} they phase separate and form ELP-rich coacervates.[15-16] Interestingly, the T_{cp} can be tuned mainly by varying the nature of amino acid residues of the pentapeptide sequence, in particular at the Xaa position, the number of repeat sequences, and the ELP concentration. Here, we specifically focused on a methionine-containing ELP with a primary structure of 40 repeat units of a pentapeptide presenting Val/Met as guest residues in a 3:1 ratio, namely ELP[M_1V_3-40] as reported elsewhere.[17] We chemically

conjugated the ELP[M_1V_3-40] to a 2 kDa polyethylene glycol (PEG) yielding the ELP[M_1V_3-40]-*b*-PEG bioconjugate (ELP-*b*-PEG) to form colloidally stable organelle-like compartments.[10c] The ELP-*b*-PEG bioconjugate was fluorescently labeled with rhodamine to enable observation of the spatial distribution of the bioconjugate by fluorescence imaging . To study the dynamic organelle assemblies, the ELP-*b*-PEG bioconjugate (0.25 mg·mL^{-1}) was encapsulated in partially dewetted liposomes together with an 8 wt% PEG solution, mimicking the macromolecular crowded environment of a cell (Figure 1a).[18] A hyperosmotic stress was preferred to a heating system to induce assembly of the synthetic organelles in the newly formed partially dewetted liposomes (Figure 2a). This indeed ensured the possibility of assembling synthetic organelles at room temperature inside the cell-mimicking entities, and avoided the inactivation of the future-to-use enzyme. In a first step, we examined the capacity of LLPS of the ELP-*b*-PEG bioconjugate within partially dewetted liposomes by a strong hyperosmotic stress with the addition of a 1 $_M$ sucrose hypertonic solution. Prior to the hypertonic shock, a uniform distribution of ELP-*b*-PEG was observed within the freshly collected lipid compartments (Figure 2b-d). After the hypertonic stress induced by the addition of 1 $_M$ sucrose, partially dewetted liposomes exhibited a rapid reduction in volume to balance the difference in osmotic pressure between the inner and outer environment, instantaneously resulting in the LLPS of the ELP-*b*-PEG bioconjugate into ELP-rich coacervate core micelles as evidenced by the fluorescent aggregates (Figure 2e,f; Figure S1, Supporting Information). As seen in Figure 2g, synthetic membraneless organelle-like constructs spatially distributed in an even manner in the artificial cellular compartment. Significantly, being hit by the hyperosmotic stress, partially dewetted lipid vesicles collectively shrank in volume while maintaining their initial shape, rather than deforming into star-like vesicles or elongated lipid tubes.[13] This confirmed that additional lipids from the shrunken lipid vesicles were fully collected into the lipid reservoirs, offering a new route to precisely govern lipid vesicle size under hypertonic shock. It is noteworthy that the shrunken partially dewetted lipid vesicles are able to reversibly de-shrink in the condition of hypoosmotic stress, swelling closely back to their initial sizes and simultaneously disassemble the organelle-like constructs (Figure S2, Supporting Information).

The effect of hyperosmotic stress upon LLPS of the ELP-*b*-PEG bioconjugate was also investigated at room temperature (23 °C). Hypertonic solutions with increasing concentrations in sucrose (0.25, 0.5, and 1 $_M$) to shrink the partially dewetted liposomes to different extents were explored respectively. The 0.25 $_M$ solution decreased by 35% the initial volume of the lipid vesicles

and therefore locally increased the concentration of the ELP-*b*-PEG bioconjugate by a factor of 1.5 (Figure 2h). This condition scarcely assembled synthetic organelles in the lipid vesicles as fluorescently labeled bioconjugates did not show any major aggregation (Figure 2j). The 0.5 M sucrose solution shrank by 52% the original volume of the lipid compartments, therefore doubling the local concentration in ELP-*b*-PEG, (Figure 2h) which assembled into organelle-like architectures inside the lipid cellular constructs as indicated by fluorescently brighter aggregates of ELP-*b*-PEG conjugates (Figure 2k). Last, the 1 M sucrose solution was able to reduce by 62% the initial volume of the liposomes and *in situ* surged the local concentration of ELP-*b*-PEG conjugate by 2.6 (Figure 2h). Expectedly, upon hyperosmotic stress with 1 M sucrose solution, all ELP-*b*-PEG bioconjugates underwent LLPS, assembling a significant population of synthetic membraneless organelles (Figure 2l). These results confirmed that the higher the concentration of the hypertonic sucrose solution, the stronger the hyperosmotic stress exerted on the partially dewetted liposomes, resulting in a higher water efflux that leads to a decrease in vesicle volume. Consequently, the concentration of ELP-*b*-PEG increases locally, inducing the formation of many synthetic subcellular organelles. Indeed, since ELP's cloud point temperature T_{cp} is inversely proportional to their concentration, it can be assumed that the higher the concentration of the hypertonic solution, the greater the shift of T_{cp} of the ELPs to lower temperatures, explaining the observed coacervate formation in isothermal condition as a response to increased concentration (Figure S3, Supporting Information). Noteworthy, hyperosmotic shrinking concentrates not only ELP-*b*-PEG bioconjugates, but also increases the concentration of the macromolecular crowding agent (PEG) which also impacts the shift of T_{cp} to lower temperatures.[10c, d] Considering the combined effect of concentration and macromolecular crowder upon T_{cp} of the ELP-*b*-PEG conjugate, we thus determined the transition temperatures of the resulting three osmotically concentrated ELP-*b*-PEG in their own solution conditions respectively. As evidenced by light scattering experiments (Figure 2i; see experimental details in Supporting Information), ELP-*b*-PEG bioconjugates exhibited a T_{cp} of 34.3 °C for the situation with no hyperosmotic shock, that was shifted back to 30 °C for a hypertonic shock induced with a 0.25 M sucrose solution. Since still clearly above ambient temperature, this validated why no synthetic organelle were observed in Figure 2j. With a further increase in sucrose concentration to 0.5 M, the transition temperature shifted to 22.6 °C, and continued shifting to below 10 °C for a 1 M sucrose solution. These measurements are fully consistent with observations from confocal microscopy imaging (Figure

2k,l), attesting the approach of shrinking partially dewetted liposomes is a powerful way to *in vitro* recreate and study the formation of membraneless organelles *via* LLPS in isothermal condition.

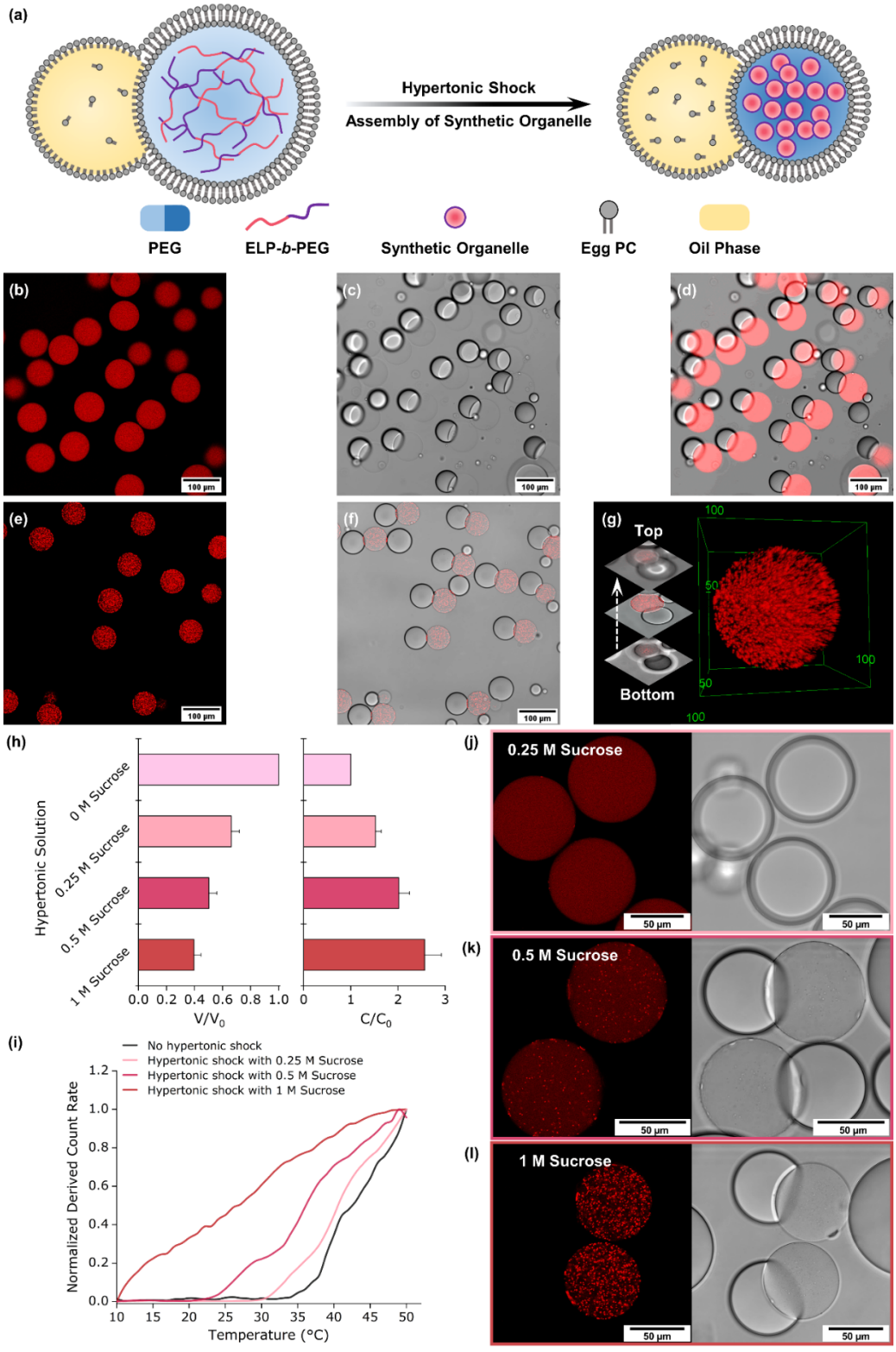

Figure 2: Hypertonicity-triggered assembly of synthetic organelles within partially dewetted liposomes. (a) Schematic illustration of formation of ELP-b-PEG synthetic organelles inside cytomimetic lipid compartments in response to hyperosmotic stress. (b-d) Representative confocal images of partially dewetted liposomes with ELP-b-PEG encapsulated prior to hypertonic shock, as shown in (b) red channel, (c) bright field and (d) merged channels, respectively. (e-f) Confocal images of as-formed ELP-b-PEG synthetic organelles after a 1 $_M$ sucrose hypertonic shock; (e) red channel and (f) merged channels. (g) 3D reconstruction of z-stack confocal images of a partially dewetted lipid vesicle inside of which the ELP-b-PEG synthetic organelles are homogeneously distributed. (h) Volume and corresponding concentration ratios of liposomes respectively, depending on the osmolarity of the hypertonic sucrose solutions (n > 30 vesicles). (i) DLS analysis (measurement of the scattered light intensity, also referred to as the normalized derived count rate, DCR) before and after inducing a hypertonic shock allowing the determination of the T_{cp} of ELP-b-PEG bioconjugate in different hypertonic conditions. (j-l) Confocal microscopy images represent the efficiency of the various hypertonic sucrose solutions to assemble ELP-b-PEG synthetic organelles inside partially dewetted lipid vesicles; (j) 0.25 $_M$, (k) 0.5 $_M$ and (l) 1 $_M$ sucrose.

2.2. Synthetic organelle constructs from co-assembly of ELP-based multicomponent systems

Given that ELP-*b*-PEG bioconjugates are capable of compartmentalizing an ELP-rich hydrophobic coacervate by heating an ELP-based multicomponent system,[10c] we have further here evaluated the potential of hyperosmotic stress to induce similarly the assembly of colloidally stable ELP-based multicomponent systems in partially dewetted lipid vesicles (Figure 3a). Similar to our previous report, a BODIPY-labeled monoblock ELP of similar sequence and longer length (BDP-ELP[M_1V_3-60], noted thereafter as BDB-ELP) was chosen to phase-separate and form the ELP-rich coacervate core. An ELP-based multicomponent system of BDP-ELP at 0.5 mg·mL^{-1} and ELP-*b*-PEG at 0.25 mg·mL^{-1} was encapsulated inside partially dewetted lipid compartments. The two fluorophores were found evenly distributed, indicating that both BDP-ELP and ELP-*b*-PEG were in soluble state, as illustrated in Figure 3b1. Shrinking of synthetic cellular compartments *via* a hypertonic solution (1 $_M$ sucrose) gave rise to immediate assembly of ELP-based multicomponent organelle-like structures as evidenced by a clear colocalization of rhodamine and BODIPY dyes grafted onto the ELP-*b*-PEG bioconjugate and monoblock ELP[M_1V_3-60], respectively (Figure 3b2). These observations of co-assembled complex synthetic organelles from an ELP-based multicomponent system (Figure 3b; Figure S4, Supporting Information) are in good agreement with our previous findings.[10c] To further assess the co-assembly of the system, we also performed dynamic light scattering measurements (DLS) for the three different solutions (BDP-ELP alone;

ELP-*b*-PEG alone; and physical mixture of BDP-ELP and ELP-*b*-PEG). As illustrated in Figure 3c, the ELP-*b*-PEG bioconjugate exhibited a cloud point temperature around 33 °C, whereas the T_{cp} of both BDP-ELP and ELP-based multicomponent system were remarkably identical (≈ 23 °C), revealing a high degree of co-assembly of the monoblock ELP and the ELP-*b*-PEG bioconjugate. As such, by means of engaging hyperosmotic stress to shrink our partially dewetted artificial cells, a complex ELP-based multicomponent system can co-assemble into highly organizational and hierarchical subcellular organelle-mimics.

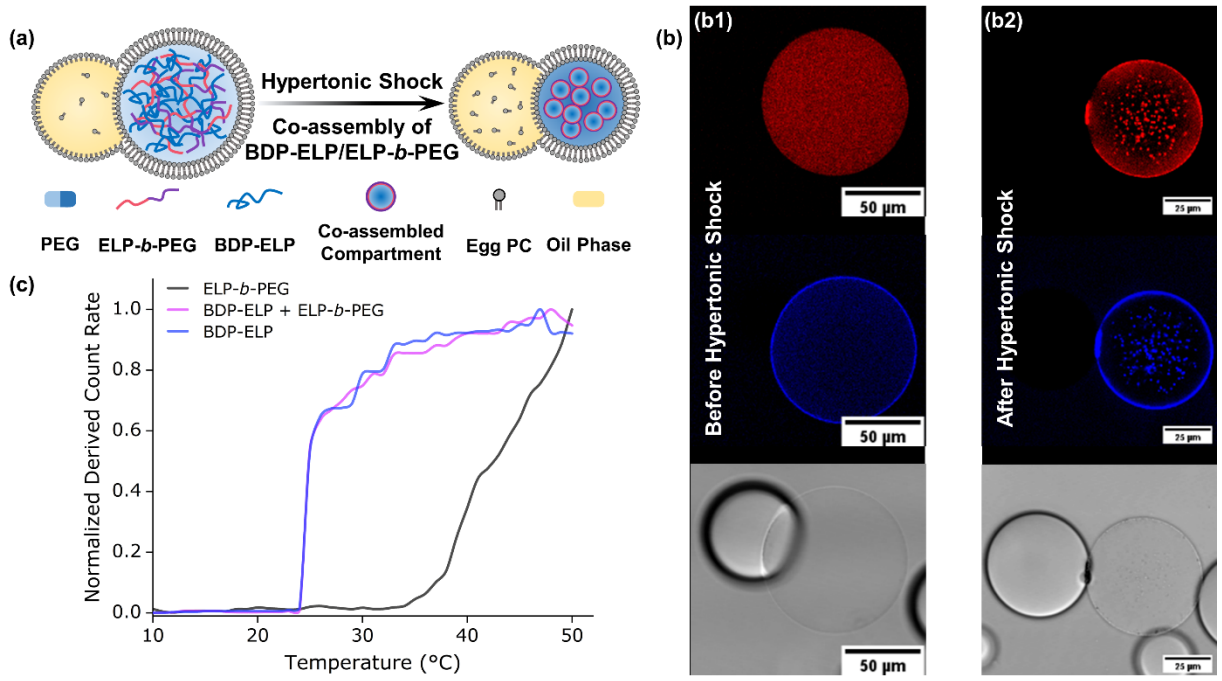

Figure 3: Synthetic organelle constructs from co-assembly of ELP-based multicomponent system. (a) Scheme of co-assembly of the monoblock BDP-ELP and the ELP-b-PEG bioconjugate into complex synthetic organelles within shrinking liposomes. (b) Representative confocal microscopy images of ELP-based multicomponent system (BDP-ELP/ELP-b-PEG)-containing partially dewetted liposomes before and after hypertonic shock; (b1) no synthetic organelles formed before hypertonic shock and (b2) co-assembled BDP-ELP/ELP-b-PEG into synthetic organelles after hypertonic shock. (c) DLS measurements for the three separate systems verifying the co-assembly mechanism established for the ELP-based multicomponent system.

2.3. Design of synthetic biocatalytic organelles to modulate the kinetics of enzymatic reactions

After assembling complex and colloidally stable synthetic organelles from the ELP-based multicomponent system, we sought to reconstitute a higher level of complexity and functionality (Figure 4a). To achieve this, we have designed an ELP-bioconjugate with horseradish peroxidase (HRP) as a model enzyme. A bioengineered ELP[M_1V_3-40] containing a *C*-terminal cysteine group was produced in *E. coli* and coupled to HRP using an heterobifunctional cross-linker 4-(*N*-maleimidomethyl)cyclohexane-1-carboxylic acid 3-sulfo-*N*-hydroxysuccinimide ester (Figure 4b; Figure S5, S6 and S7 and see experimental details in Supporting Information). In order to evaluate the co-assembly ability of biofunctional conjugate ELP-*b*-HRP with the monoblock ELP, we first performed DLS measurements by detecting the cloud point temperatures of the following three solutions in 8 wt% PEG: BDP-ELP alone, ELP-*b*-HRP and BDP-ELP/ELP-*b*-HRP. As seen in Figure 4c, the bioconjugate ELP-*b*-HRP evidenced a transition temperature at 26 °C. However, both transition temperatures of BDP-ELP and BDP-ELP/ELP-*b*-HRP shifted towards the same cloud point temperature around 23 °C, confirming the successful co-assembly of the monoblock ELP and the biofunctional ELP-*b*-HRP conjugate, similar to previous experiments (Figure 3c). We have then used this approach to design a system that combined the three ELP-derived elements, namely the monoblock ELP, the ELP-*b*-PEG and the biofunctional ELP-*b*-HRP conjugate. We could then anticipate conditions where the ELP-*b*-HRP conjugate could be free in solution (before hypertonic shock) or co-assembled in the tripartite coacervate (after hypertonic shock with 1 $_M$ sucrose) at the same ambient temperature (defined as 23 °C). This now allowed us to measure the HRP enzymatic kinetics in these different situations at same temperature and enzyme concentration, both in bulk solution and in partially dewetted liposomes, and evaluate the effect of confinement of the enzyme in organelle-like system, thus mimicking very closely cells' behavior. This kinetics analysis was conducted using the following enzymatic reaction: amplex red was oxidized by H_2O_2 through the catalysis of HRP to produce resorufin as a fluorescent probe (Figure 4a,b). It was ensured that the same concentration of HRP was used between free HRP and ELP-*b*-HRP for further experiments. The kinetic analysis of ELP-*b*-HRP and HRP was first assessed in bulk solution, in water and in 8 wt% PEG as a crowding agent, which are conditions similar to those in our artificial cells. The co-factor H_2O_2 concentration was first varied. The Michaelis-

Menten kinetics for each of these conditions could be determined using equations (Equation S3 and S4, Supporting Information), as well as the Lineweaver Burk plots (Figure S8, see experimental methods in Supporting Information).[19] All calculated values are reported in Table 1. In 8 wt% PEG conditions, the K_m of ELP-*b*-HRP decreased 5.7 times compared to water, and 2.9 times for free HRP. This reflected a higher affinity between the substrate and the enzyme, attributed to the increased probability of an interaction between the enzyme and the substrate due to the crowded PEG environment, in agreement with previous reports.[19-20] However, the enzyme's specific activity (*S.A.*) and V_{max} decreased. The *S.A.*, referring to the mole of substrate converted by the enzyme per unit time per mg of the total enzyme,[21] decreased by 9 folds for ELP-*b*-HRP and 5.5 times for free HRP in PEG conditions compared to water. This could be associated with the limited diffusion of the substrate and the enzyme considering the complexity of the PEG solution and its potential interaction with the substrate and/or the enzyme and/or the coacervates.[19, 22] Hence, the crowding capacity of PEG slowed down the kinetics of enzymatic reactions compared to water, but enhanced the affinity between the substrate and the enzyme.

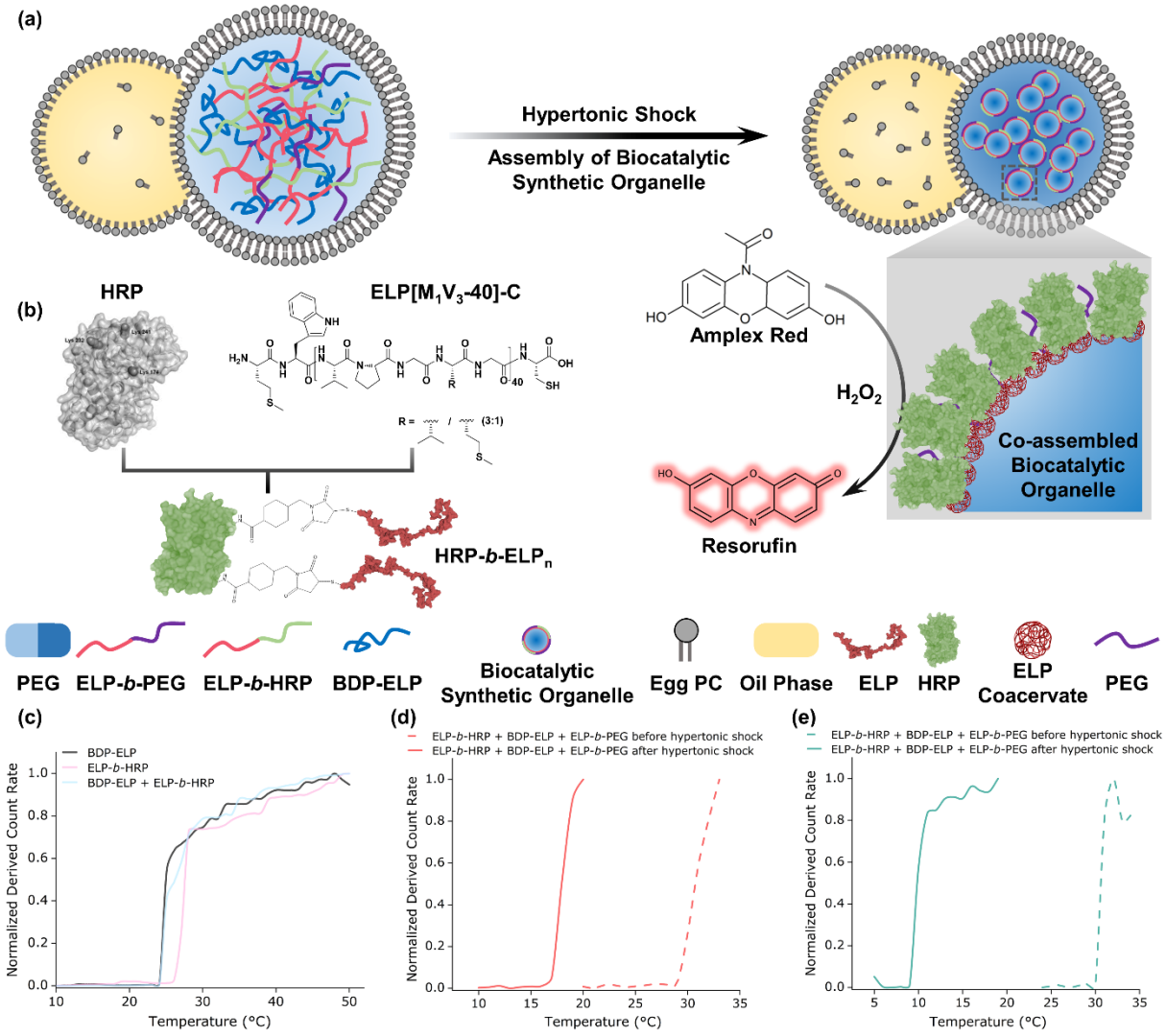

Figure 4: Synthetic catalytic organelles built from co-assembly of a complex ELP-based multicomponent system. (a) Scheme illustrating the shrinking-induced co-assembly of BDP-ELP, ELP-b-PEG and ELP-b-HRP forming synthetic organelles that are able to catalyze a chemical substrate, amplex red, to a product, resorufin, upon exposure to a chemical fuel of H_2O_2 in the surrounding environment. (b) Schematic representation of the ELP-b-HRP bioconjugate design. (c) Determination of co-assembled performance of the ELP-based multicomponent system including BDP-ELP, ELP-b-PEG and ELP-b-HRP in the solution of 8 wt% PEG. (d) Determination of cloud point temperatures via DLS measurements of the ELP-based multicomponent system reproduced the condition in bulk solution before and after in response to hypertonic stress. (e) Determination of cloud point temperatures via DLS measurements of the ELP-based multicomponent system reproduced in the condition occurring inside partially dewetted liposomes before and after in response to hypertonic stress.

Table 1: Michaelis Menten constant (K_m), V_{max}, S.A. of ELP-b-HRP and HRP in water and 8 wt% PEG, respectively.

Solutions	K_m (μmol·L^{-1})	V_{max} (μmol·L^{-1}·s^{-1})	*S.A.* (mmol·g^{-1}·s^{-1})
HRP in water	12.5	0.72	0.33
HRP in 8 wt% PEG	4.37	0.13	0.06
ELP-*b*-HRP in water (no coacervates)	22.59	0.71	0.18
ELP-*b*-HRP in 8 wt% PEG (no coacervates)	3.95	0.09	0.02

The kinetics between free HRP and ELP-*b*-HRP were further compared before and after inducing a hyperosmotic stress, to demonstrate the ability of the synthetic organelles to drag and locally increase the concentration of the enzyme and the fluorescent probe. Experiments were first carried out in bulk solution to determine the enzymatic kinetics by fluorescence spectroscopy (see experimental details in Supporting Information). We evaluated the initial and final concentrations of the different compounds as described in the experimental part to mimic the internal environment of vesicles during osmotic variations (Table S1, Supporting Information). DLS analyses were conducted to determine the T_{cp}s of the ELP-based multicomponent system before and after inducing a hypertonic shock. As seen in Figure 4d, the T_{cp}s were detected at 29 °C and 16 °C respectively, meaning that when performing experiments at 23 °C, the ELP-based multicomponent system will be homogeneously dispersed in initial conditions and will phase separate after a hypertonic shock. Enzymatic reactions were initiated as soon as H_2O_2 was injected into the cuvettes and the increase of fluorescence intensity was monitored (Figure 5a). It was observed that, before inducing the hypertonic shock, the kinetics of the reactions were comparable between the system composed of ELP-*b*-HRP and HRP as the slopes of the curves were similar (Table 2). Also, the final fluorescence intensity of the reaction was equivalent in both cases, proving that an equivalent concentration of HRP was used. In the conditions following the hypertonic shock, the slope of the ELP-*b*-HRP curve was much steeper (25.07 ± 3.59 a.u.·s^{-1}) than the one of free HRP (18.26 ± 0.14 a.u.·s^{-1}), suggesting that the formation of synthetic organelles locally concentrated the enzyme and the amplex red, ensuring a faster enzymatic reaction. As a control, an experiment was conducted using the ELP-*b*-PEG conjugate (Figure 5a). No fluorescence could be detected,

attesting that no uncontrolled oxidation occurred in our experimental conditions and the presence of HRP was mandatory for a fluorescence signal to be detected. To further support our findings, an alternative chemical substrate 2,2'-azino-bis(3-ethylbenzothiazoline-6-sulphonic acid) (ABTS) was used for the enzymatic reaction with assistance of the enzyme HRP and H_2O_2. The kinetics of ABTS oxidation into its radical cationic blue-colored $ABTS^{\cdot+}$ was determined using UV-Vis spectrophotometer (see experimental details in Supporting Information). Similar enzymatic reaction rates were observed where both ELP-*b*-HRP and free HRP (after hyperosmotic shock) can faster catalyze the oxidation process of ABTS to $ABTS^{\cdot+}$ than conditions with both enzymes freely dispersed in the 8 wt% PEG solution (Figure S9, Supporting Information). Significantly, after hypertonic shock, the ELP-based multicomponent system exhibited a remarkably higher reaction kinetics than that of the free HRP-containing system, reaffirming as-formed biocatalytic synthetic organelles can powerfully enhance the rate of enzymatic reaction.

Table 2: Slope of the fluorescence intensity curves versus time.

Solution	Slope (a.u.·s^{-1}) from (t = 0)
ELP-*b*-HRP after hypertonic shock	25.07 ± 3.59
HRP after hypertonic shock	18.26 ± 0.14
ELP-*b*-HRP before hypertonic shock	12.19 ± 0.79
HRP before hypertonic shock	11.04 ± 0.85

Experiments were then conducted inside partially dewetted vesicles obtained from a microfluidic system and under confocal microscopy. Prior to investigating the performance of enzymatically active synthetic organelles, we examined the permeability of the eventual product (resorufin) to membranes of partially dewetted liposomes (Figure S10, Supporting Information). Partially dewetted liposomes were incubated with resorufin within the same observation chamber. No significant fluorescence intensity increase inside liposomes was observed after monitoring the diffusion of resorufin for 20 min. Thus, this finding validated that the fluorescence intensity changes resulted from the enzymatic reaction within liposomes and not by possible resorufin diffusion due to vesicle bursting in the surrounding environment. A ten times higher concentration of the enzyme was used for both ELP-*b*-HRP-containing multicomponent system and HRP alone system due to intrinsic differences in device sensitivity. This greatly shifted the T_{cp} from 30 °C to

9 °C before and after hyperosmotic stress, respectively (Figure 4e). As can be seen in Figure 5b, in conditions of non-shrinking, the increase of fluorescence was very slow and visually imperceptible for both free HRP and the ELP-*b*-HRP system, even 950 s after H_2O_2 injection (Figure S11, Supporting Information). In this case, the HRP that was freely dispersed in the vesicle lumen behaved consistently in both cases, with a slow kinetics as averaged on 14 vesicles (Figure 5b). After a hypertonic shock and a resulting shrinking of partially dewetted vesicles, the production of the fluorescent resorufin could be detected and measured over time (Figure 5b). For free HRP, the resulting increase of enzymatic concentration accelerated the reaction kinetics and a plateau was reached about 1,000 s after H_2O_2 injection (Figure 5b,c; Video S1, Supporting Information). In the case of the ELP-*b*-HRP-containing system, the enzymatic reaction was much faster, with a maximum fluorescence obtained after 250 s only (Figure 5b,c; Video S1, Supporting Information). In the latter case, HRP was confined on the surface of biocatalytic organelle constructs, inducing an increased local concentration of enzyme that enhanced the reaction kinetics. Concomitantly, coacervate formation offered a more hydrophobic environment for amplex red that can also be responsible of a local increased concentration of both enzyme and reactant that can also favor the reaction.[23]

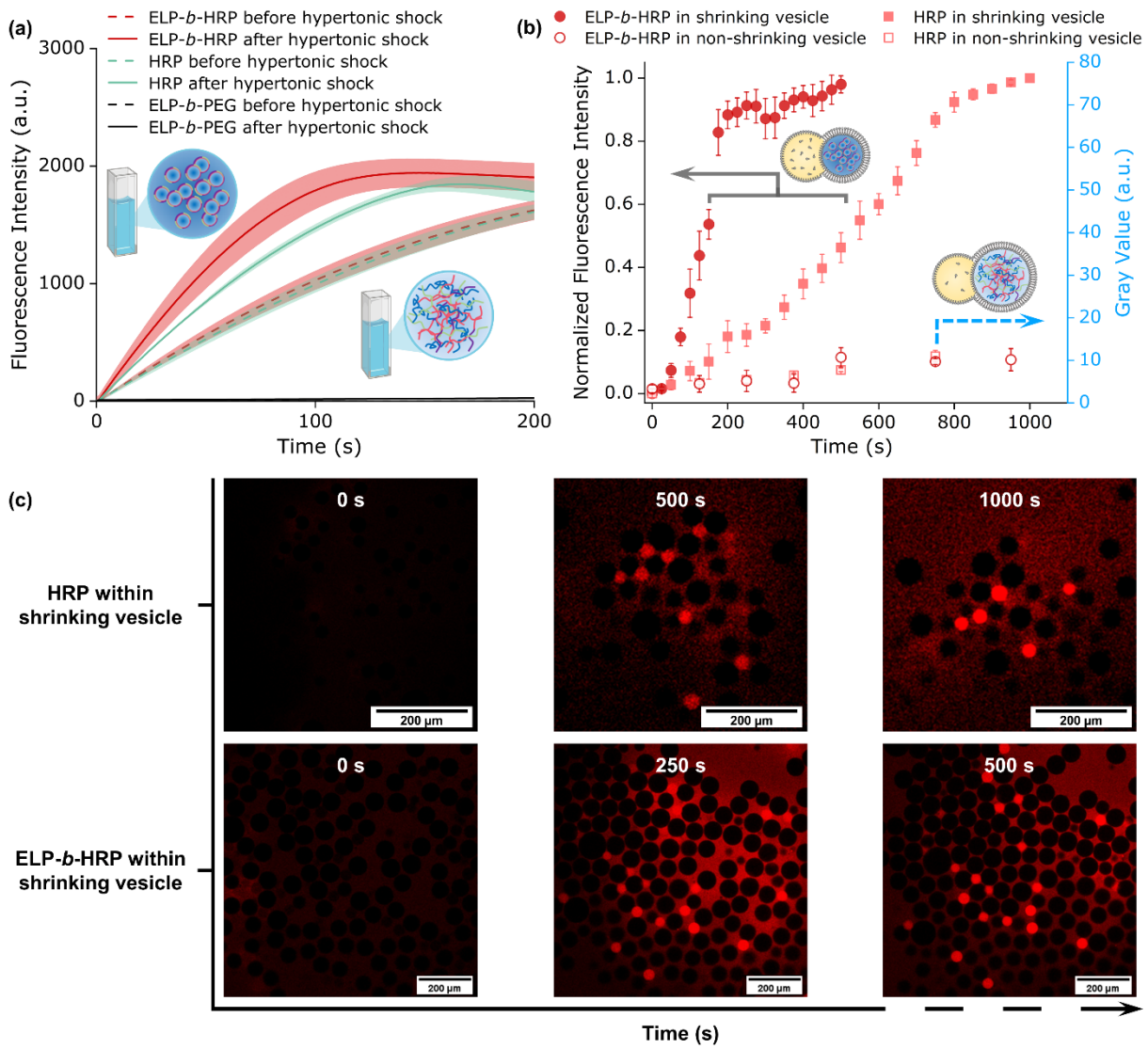

Figure 5: Kinetics of the enzymatic reaction from ELP-based multicomponent system and free HRP system before and after a hypertonic shock, respectively. (a) Kinetics of enzymatic reactions monitored by the increase of fluorescence intensity detected with spectroflurometer. (b) Enzymatic reaction occurring in shrinking and non-shrinking vesicles from ELP-b-HRP system and HRP system. (c) Time series of confocal microscopy images in the red channel to follow the formation of resorufin after the hypertonic shock in vesicles encapsulating free HRP and ELP-b-HRP system, respectively.

3. Conclusion

A partially dewetted liposome strategy has been developed to investigate the ability of phase separation of enzyme-functionalized elastin-like polypeptides into a crowded biomacromolecule's environment mimicking the cell cytoplasm. Thanks to osmotic pressure modulation, the characteristic cloud point temperature (T_{cp}) of ELPs could be tuned so that synthetic organelle compartments of an ELP-based multicomponent system with HRP as a model enzyme could be formed as a response to hyperosmotic stress. Such dynamic formation of membraneless organelles in a liquid-liquid phase separation mechanism represents an advance towards synthetic cell research as it brings together LLPS, compartmentalization and enzymes. The importance of the assembly of such synthetic organelles has been demonstrated to accelerate enzymatic reactions by locally increasing the enzyme concentration. This work proposes a unique approach to create protocellular systems with a new osmotic trigger to dynamically assemble intracellular synthetic organelle formation. It also represents a significant advance towards the construction and induction of complex cascade reactions in more realistic synthetic cells, promising to further our understanding of the importance and role of membraneless organelles in biological enzymatic reactions.

4. Materials and Methods

Materials: Poly(ethylene glycol) (PEG, 6 kDa) polymer was purchased from Alfa Aesar. Poly(vinyl alcohol) (PVA, 13-23 kDa, 87-89% hydrolyzed) polymer, sucrose (GC, 95.5%), sigmacote, 3-aminopropyltriethoxysilane (APTES, 98%), ampliflu™ red (HPLC grade, 96%), 2,2'-azino-bis(3-ethylbenzothiazoline-6-sulfonic acid (ABTS, HPLC grade, 98%), resorufin (95%), the enzyme of horseradish peroxidase (HRP, hydrophilized powder, 150 U mg^{-1}), the heterobifunctional cross-linker 4-(*N*-maleimidomethyl)cyclohexane-1-carboxylic acid 3-sulfo-*N*-hydroxysuccinimide ester sodium salt (sulfo-SMCC) and *N*,*N*-diisopropylethylamine (DIPEA) were purchased from Sigma-Aldrich. L-α-phosphatidylcholine (Egg PC, 25 mg ml^{-1} in chloroform) was bought from Avanti Polar Lipids. Pluronic® F-68 was obtained from Gibco. Hydrogen peroxide (H_2O_2, 35%) was purchased from Acros. All compounds were used without further purification. The following solvent were purchased from Sigma-Aldrich and used without

further purification: chloroform (anhydrous, 99%), hexane (anhydrous, 95%) and dimethyl sulfoxide (DMSO, 99.9%). Water with a resistivity of 18.2 MΩ cm^{-1} was prepared using a Millipore Milli-Q system.

Statistical Analysis: For the determination of volume and corresponding concentration ratios of liposomes respectively, depending on the osmolarity of the hypertonic sucrose solutions, results were displayed as mean ± standard deviations. The sample sizes (*n*) were provided in the figure legends. The kinetics of enzymatic reactions from ELP-*b*-HRP and HRP respectively that were determined by the slope of the fluorescence intensity curves versus time were shown as mean ± standard deviations (n = 3 replicates). Concerning the measurements of T_{cp}, all data of derived count rate and the fluorescence intensity increase for both ELP-*b*-HRP and HRP in shrinking vesicles were respectively normalized from 0 to 1 by using the software Origin (OriginLab Corp).

Microfluidics: To generate water-in-oil-in-water double emulsions, a capillary-based microfluidic device was utilized.[1] To make the co-flow microfluidic device, two cylindrical capillaries of inner diameter 580 μm and outer dimension 1 mm (World precision instruments, 1B100-4) were tapered by a micropipette puller (Sutter instrument, P-97) followed by polishing the orifices with sand papers into 60 μm and 120 μm, respectively. The capillary with smaller orifice treated by sigmacote into hydrophobic was used for injection innermost aqueous phase, while surface of the larger-sized capillary was rendered into hydrophilic by APTES and used as the collection channel. A square capillary (VitroCom, 2956C1) was used to nest both cylindrical capillaries that were inserted in opposite direction. Lastly, dispensing needles used as inlets of fluids were connected at the junctions between capillaries by using a transparent 5 min Epoxy (Devcon). The devices were connected to high-precision syringe pumps (Chemyx, Fusion 100) *via* polyethylene tubing (Scientific Commodities Inc., BB31695-PE/4) to ensure reproducible, stable flows.

Formation of double-emulsion microdroplets and their transformation to partially dewetted liposomes: Typically, to create water-in-oil-in-water double-emulsion microdroplets for studying hyperosmotic stress-induced formation of synthetic organelles, an aqueous phase - 8 wt% PEG phase containing 0.25 mg ml^{-1} of rhodamine-labelled ELP-*b*-PEG was flowed in the injection capillary as innermost solution. An organic mixture of chloroform and hexane (36:64 vol%)

containing 5 mg mL^{-1} of Egg PC was used as middle phase and was injected through the interstices between the injection and square capillaries, whereas the continuous phase of 10 wt% PVA with 0.2% F-68 was pumped through the interstices between the collection and square capillaries. Typical flow rates were set to 500, 1000 and 8000 µL h^{-1} for inner, middle and outer phases, respectively. These three phases produced double-emulsion microdroplets at the junction, which then flowed along the collection capillary and were collected and sealed with a cover slip in a cavity glass slide (BRAND®). Observations of transformation of W/O/W double emulsions to partially dewetted liposomes were made after 15 mins since fresh microdroplets were collected. The oil phase that initially surrounds the inner aqueous lumen gradually underwent dewetting process with the assistance of F-68, forming a lipid reservoir which remained attach to the lipid vesicles.

Bioproduction, isolation and purification of ELP[M_1V_3-40], ELP[M_1V_3-40]-Cysteine, ELP[M_1V_3-60] and ELP-b-PEG bioconjugate: ELP[M_1V_3-40], ELP[M_1V_3-40]-Cysteine and ELP[M_1V_3-60] were produced by recombinant DNA and protein engineering techniques in *E. coli* and isolated using previously reported procedures.[2] The bioconjugate of ELP-*b*-PEG was produced and isolated as previously presented by our group elsewhere.[3]

Synthesis of ELP-b-HRP conjugate: **Step 1** - 0.2 µl of DIPEA (1.2 µmol, 2 equiv.) was added to a solution of HRP (23 mg, 0.6 µmol, 1 equiv.) in phosphate buffer saline (PBS) pH 7.4 (10 mg ml^{-1}) and stirred for 15 min. 3 mg of cross-linker sulfo-SMCC (6 µmol, 10 equiv.) was dissolved in 100 µl of DMF and added dropwise to the reaction mixture. The reaction mixture was stirred at ambient temperature for 4 hours. The excess sulfo-SMCC was afterwards removed by washing (5 times) the solution with PBS pH 7.4 in centrifuge filters (Amicon Ultra-15, 10kDa); **Step 2** - ELP[M_1V_3-40]-Cysteine (20 mg, 1.2 µmol, 2 equiv.), presenting a *C*-terminal cysteine residue (Figures S4b, Figure S5), was dissolved in PBS pH 7.4 at 10 mg ml^{-1} at 4 °C. The solution of HRP-Mal from Step 1 was added. The mixture was incubated in a thermomixer at 10 °C for 24 hrs. The reaction mixture was transferred into 0.5 ml centrifuge filters (Amicon Ultra, 10kDa) and washed (5 times) with ultrapure water. The final solution was lyophilized to yield 35 mg of ELP-*b*-HRP conjugate. The conjugate was analyzed by MALDI-MS to estimate the average number of ELP chains conjugated to the HRP. Since HRP contains 4 primary amine groups (*N*-terminal end and

^{174}Lys, ^{232}Lys and ^{241}Lys residues),[4] (Figure S4a) the ELP-*b*-HRP conjugate may contains up to 4 ELPs. The molar masses of all possible conjugates are provided in the table below:

Compound	Molar mass (kDa)
ELP	17
HRP	40
ELP-*b*-HRP	57
ELP_2-*b*-HRP	74
ELP_3-*b*-HRP	91
ELP_4-*b*-HRP	109

From the relative intensity of the different species detected on the mass spectrum of the ELP-*b*-HRP conjugate, it was estimated that HRP was conjugated to 2 ELPs on average (Figure S6).

Mass-spectrometry analyses: MALDI-MS spectra were performed by the CESAMO (Bordeaux, France) on an AutoflexmaX TOF mass spectrometer (Bruker Daltonics, Bremen, Germany) equipped with a frequency tripled Nd:YAG laser emitting at 355 nm. Spectra were recorded in the positive-ion mode and with an accelerating voltage of 19 kV. Samples were dissolved either in a mixture of water and acetonitrile (1:1) or in pure water at 10 mg ml^{-1}. Sinapinic acid matrix was prepared as a supersaturated solution (ca.10 mg ml^{-1}) in a mixture of water/acetonitrile/trifluoroacetic acid (49.9:50:0.1). The solutions were combined in a 20:2 or 18:2 volume ratio of matrix to sample. 1.5 to 2 µl of the resulting solution were deposited onto the sample target and vacuum-dried.

Confocal microscopy imaging: Microdroplets were collected on a glass slide with a single cavity and subsequently sealed with a coverslip for the dewetting process to take place. Then, 7 µl of vesicles and the solution of 1 $_M$ sucrose and 0.2% F-68 solution were injected into an imaging chamber (Ibidi GmbH, Germany) to induce the assembly of the synthetic organelles. To validate the dynamic reversibility of organelle-like constructs, a water phase of 0.2% F-68 was carefully added to the imaging chamber. Regarding the enzymatic reaction, a following 225 μ_M H_2O_2 solution was injected in the imaging chamber to start the reaction. Images and videos were acquired by a confocal laser scanning microscopy (Leica, SP5 AOBS) through an HCX PL APO 10× dry objective. To assess localization of ELP-*b*-PEG and ELP[M_1V_3-60] and monitor their coacervation

and spatial distribution, they were labeled with spectrally different fluorophores. A diode laser (561 nm) and He-Ne (633 nm) ion laser were used to excite rhodamine and BODIPY, respectively. To avoid an artifact of visualizing rhodamine-labeled ELP-*b*-PEG and BODIPY-labeled ELP[M_1V_3-60], sequential imaging mode was used to reduce fluorescence crosstalk among various fluorophores. In addition, the diode laser (561 nm) was also used to excite the product – resorufin from the enzymatic reaction. All imaging acquisitions were made at room temperature (23 ℃).

Measurement of the diameter of lipid vesicles and determination of concentrations after hyperosmotic stress: The diameter of shrunken and normal lipid vesicles was analyzed by a software ImageJ.[5] The initial diameter and encapsulant concentration are denoted as D_i and C_i, respectively; the eventual diameter and encapsulant concentration are D_{ii} and C_{ii}. Because salt (or polymer) cannot transfer across the bilayer membrane, the total amount of salt (or polymer) molecules keeps the same inside the inner water compartment. Therefore, we can get

$$\frac{4}{3}\pi\left(\frac{D_i}{2}\right)^3 \times C_i = \frac{4}{3}\pi\left(\frac{D_{ii}}{2}\right)^3 \times C_{ii} \qquad \text{(Equation S1)}$$

$$C_{ii} = C_i \times \left(\frac{D_i}{D_{ii}}\right)^3 \qquad \text{(Equation S2)}$$

Consequently, the final dimension of liposomes can be easily predicted and tuned via changing the applied hyperosmotic pressure. The volumes were then determined, and shrinkage factor was calculated. The initial concentrations were then multiplied by the shrinkage factor to determine concentrations in shrunken liposomes.

Determination of transition temperature (T_{cp}) of ELP-based derivatives by dynamic light scattering (DLS): To determine the transition temperature (T_{cp}) of several ELP-based conjugates in solution, dynamic light scattering (DLS) measurements were performed on NanoZS instrument (Malvern, U.K.) at a 173° angle, at a constant position in the cuvette (constant scattering volume). The derived count rate (DCR) was defined as the mean scattered intensity normalized by the

attenuation factor. The DCR was plotted against temperature and the T_{cp} is defined as the temperature corresponding to the point where the DCR starts increasing on the plot. Measurements were carried out simulating both the inside environment of a vesicle and the conditions before/after a hypertonic shock. Temperature ramps were typically performed from 5 °C to 50 °C for all conditions.

Crowding effect of the macromolecule PEG on the Michaelis-Menten parameters: To show the crowding effect of PEG, the kinetics analysis upon systems containing either ELP-*b*-HRP or free HRP were assessed in water and PEG respectively by varying the cofactor concentration, H_2O_2. Experiments were carried out in bulk, at 23 °C. Solutions were prepared and reached final concentrations of 0.054 n_M HRP, 75 μ_M amplex red and 8 wt% PEG. The enzymatic reactions were initiated using H_2O_2 with final concentrations reaching [15 μ_M], [10 μ_M], [7.5 μ_M], [5 μ_M] and [2.5 μ_M] respectively. The fluorescence intensity *vs* time plot was obtained. Then, a calibration curve of the average fluorescence intensity *vs* the resorufin concentration was constructed. The fluorescence intensity could therefore be replaced by its equivalence in resorufin concentration over time. From this graph, the initial rates of reaction were determined by measuring the slope of the curve. By plotting the initial reaction rates *vs* the cofactor concentration, the Michaelis-Menten curves were obtained. Finally, the Lineweaver-Burk plots were constructed by taking 1/reaction rate *vs* 1/[H_2O_2]. From these graphs, the Michaelis-Menten constant K_m was determined using the following equation:

$$\frac{1}{V_0} = \frac{K_m}{V_{max}} \times \frac{1}{[S]} + \frac{1}{V_{max}} \qquad \text{(Equation S3)}$$

Where V_0 is the initial velocity of the enzyme, K_m is the Michaelis-Menten constant, V_{max} is the maximum velocity at saturating concentration, [*S*] is the concentration of the substrate. The Specific Activity (*S.A.*) of the enzyme was determined using the following equation:

$$S.A. = \frac{\text{moles of substrate transformed}}{\text{min} \times \text{total weight of enzyme}} \qquad \text{(Equation S4)}$$

All value were presented in Table 1 in the manuscript.

Determination of kinetics of enzymatic reactions in bulk by fluorescence spectrofluorometer: Measurements were carried out in bulk, in a high precision quartz glass cell from Hellma Analytics, simulating both the inside environment of a vesicle and the conditions before/after a hyperosmotic stress. As the initial and final volumes of the vesicles were known, it was possible to determine the final concentration of each of the components in the vesicles after shrinking. Experiments were conducted at 23 °C. All the compounds constituting the solutions were thoroughly mixed in an Eppendorf tube and pipetted into the cuvette. Lastly, 1 m_M H_2O_2 stock solution was added and quickly mixed through the solution, before starting running the measurement of monitoring increase of fluorescence intensity. Each experiment was repeated three times. To conduct these experiments, the fluorescence spectrometer (Jasco FP-8500) was used in the course measurement mode. To detect the produced resorufin, excitation and emission wavelength were set at 470 and 590 nm respectively.

Determination of kinetics of enzymatic reactions in bulk via using UV-Vis spectrophotometer: To reinforce the results observed using the spectrofluorometer, the same experiments were conducted in an Agilent Cary 100 UV-Vis spectrophotometer, using ABTS as an alternative reagent. In the presence of H_2O_2 and the enzyme HRP, ABTS can be oxidized to a radical cation with absorption at 405 nm. This method is however less sensitive than the spectrofluorometer, and ABTS is readily oxidized and has a slow fluorescence response compared to amplex red.

Kinetics of enzymatic reactions in partially dewetted liposomes followed by confocal microscopy: Once the protocol and parameters were established in the quartz cuvette, the experiments were conducted inside the lipid vesicles, which were achieved via the microfluidics system. The production of resorufin was followed by confocal microscopy. A ten-fold higher concentration of both ELP-*b*-HRP and HRP (compared to bulk phase analysis) was encapsulated in the vesicles due to sensitivity differences between the spectrofluorometer and the confocal microscope. A time-series imaging mode was set for monitoring the production of resorufin over time.

5. Supporting information

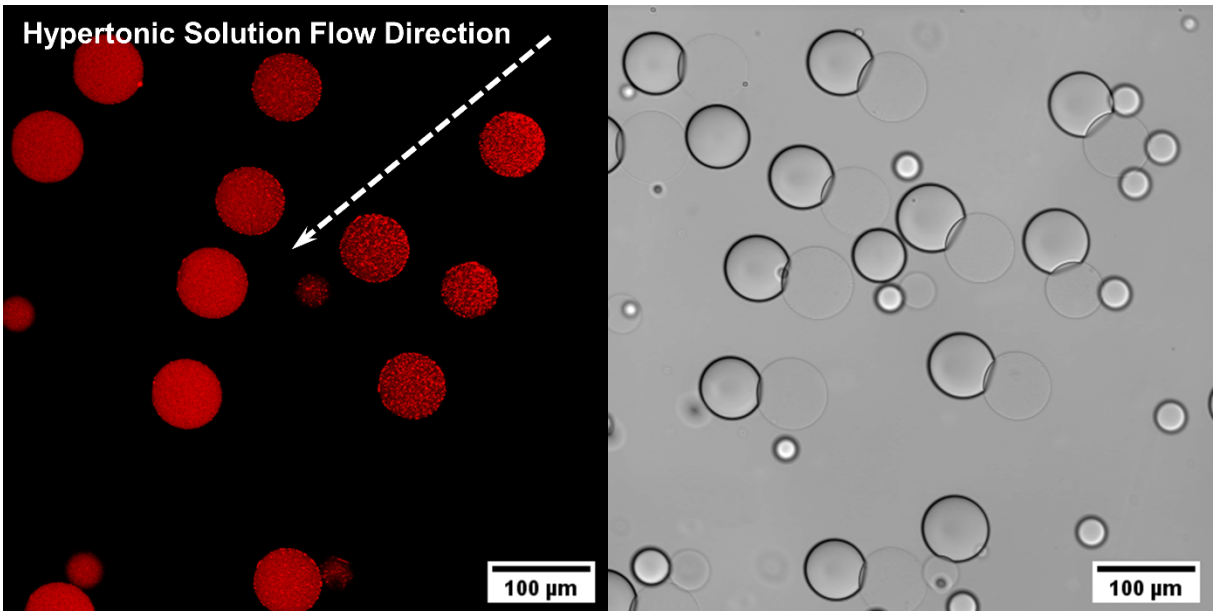

Figure S1: Gradual assembly of synthetic organelles from ELP-b-PEG bioconjugates as soon as the hypertonic solution diffuses across partially dewetted liposomes.

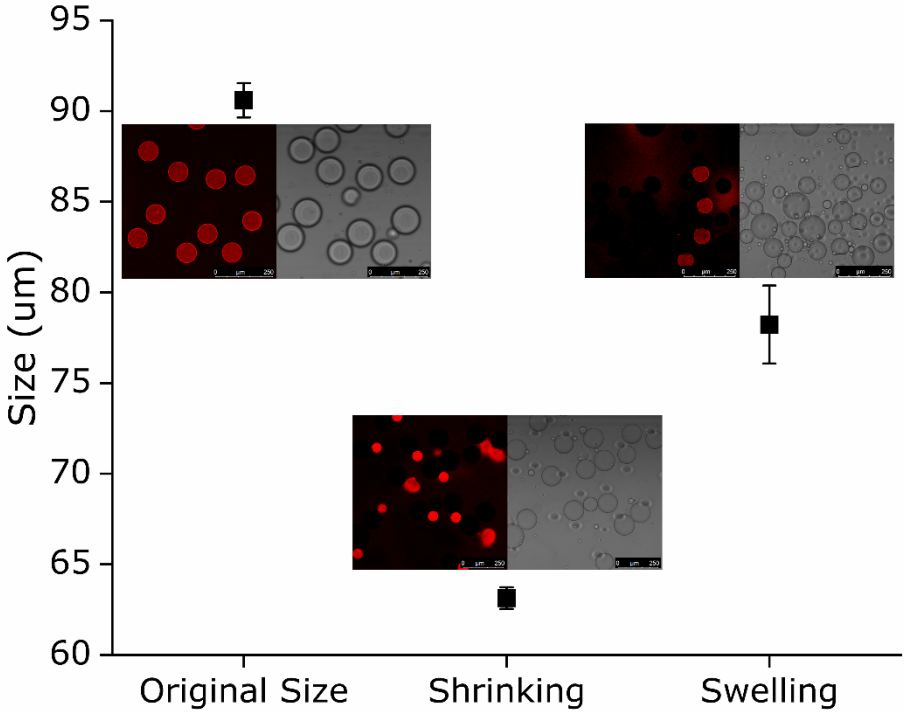

Figure S2: Confocal images and size measurements of partially dewetted lipid vesicles in the shrinking and swelling process in the hyperosmotic and hypoosmotic stress solutions respectively.

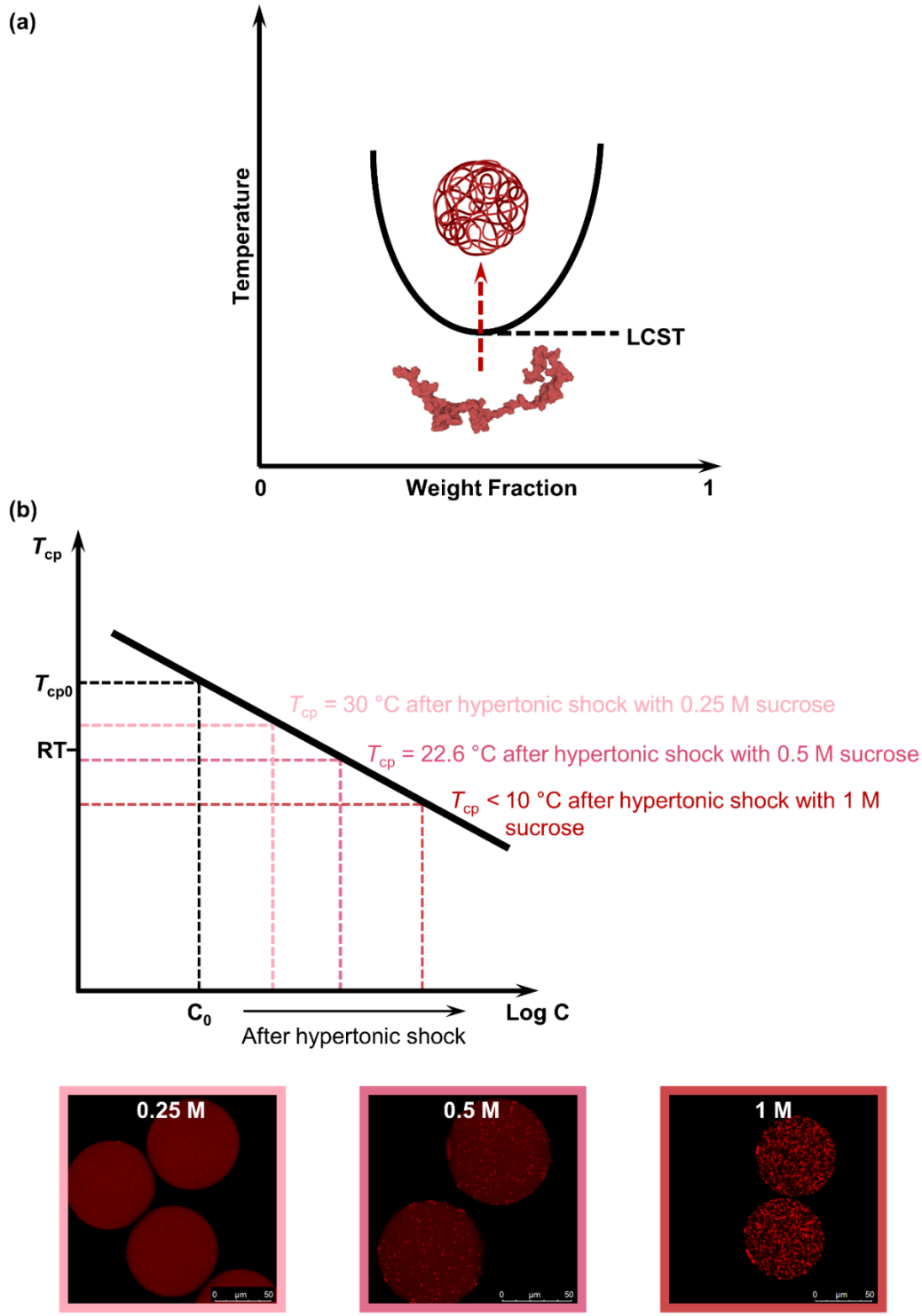

Figure S3: (a) ELPs exhibit a LCST behavior: at a specific concentration, below their cloud point temperature (T_{cp}), ELPs are water soluble and present as random coil chains; above T_{cp}, ELPs dehydrate and form coacervates. (b) Schematic illustration of the evolution of the T_{cp} of the ELP-b-PEG bioconjugate as a function of concentration. Hyperosmotic stress applied onto liposome-based artificial cells induce an isothermal concentration increase and therefore the assembly of rhodamine-labeled ELP-b-PEG chains into membraneless organelle mimics.

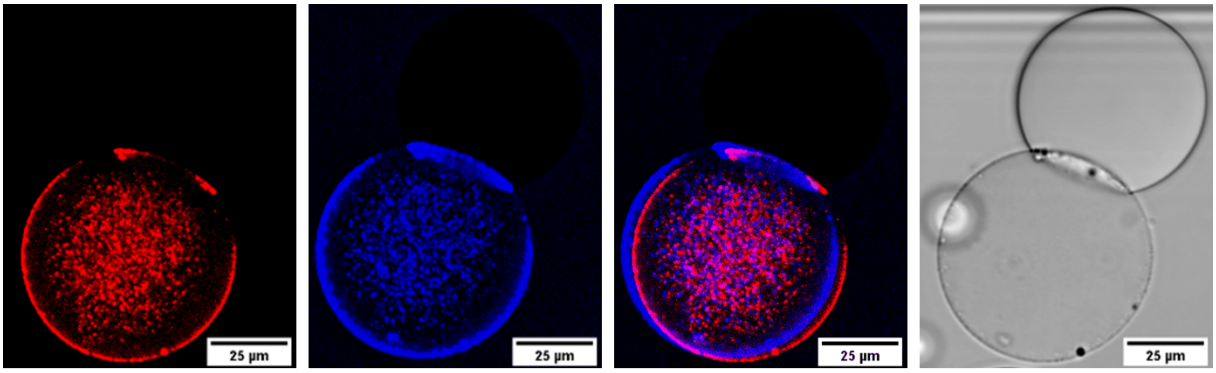

Figure S4: Representative confocal microscopy images of synthetic organelle-like assemblies from ELP-based multicomponent system (BDP-ELP + ELP-b-PEG) within a shrunken partially dewetted lipid vesicle; red color indicates ELP-b-PEG and blue indicates BDP-ELP.

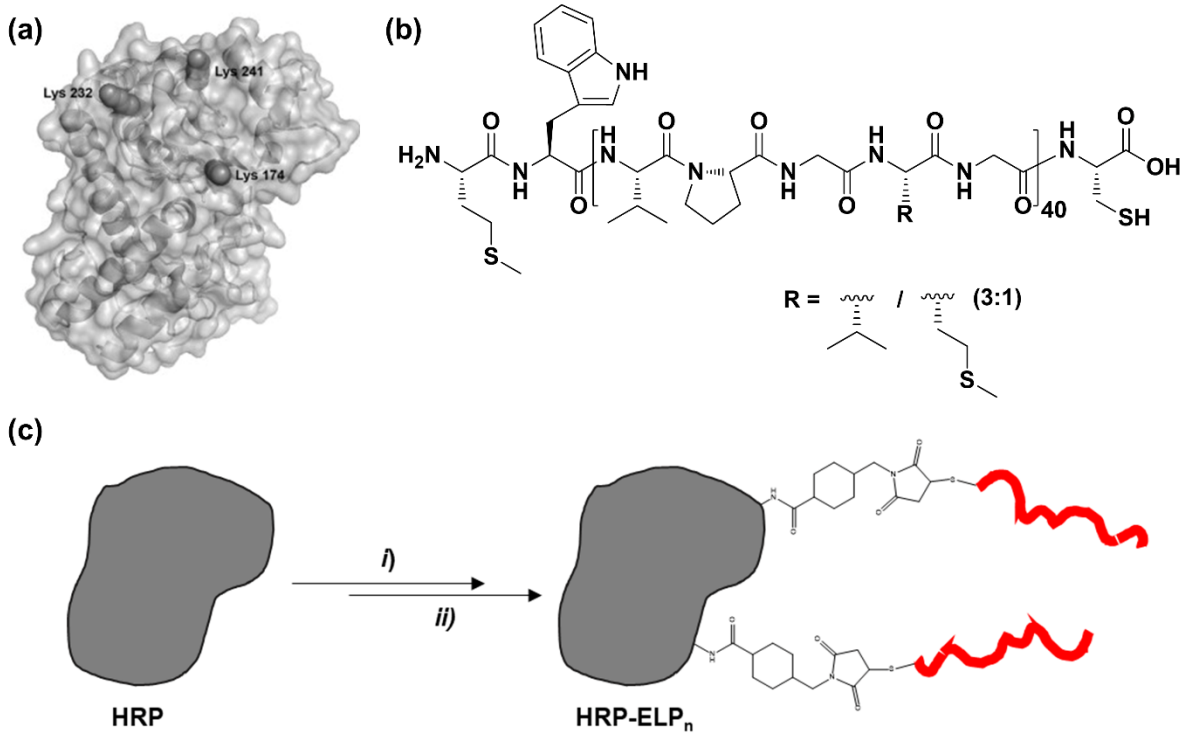

i) 10 equiv. Sulfo-SMCC, PBS pH 7.4, 2 equiv. DIPEA, 4 h, r.t.
ii) 2 equiv. ELP[M_1V_3-40]-Cys, PBS pH 7.4, 10 °C, 24h

Figure S5: (a) 3D representation of the average structure of HRP, showing 3 exposed Lys residues.[4] (b) Chemical structure of ELP[M_1V_3-40]-C. (c) Synthetic scheme and conditions to access the ELP-b-HRP conjugate.

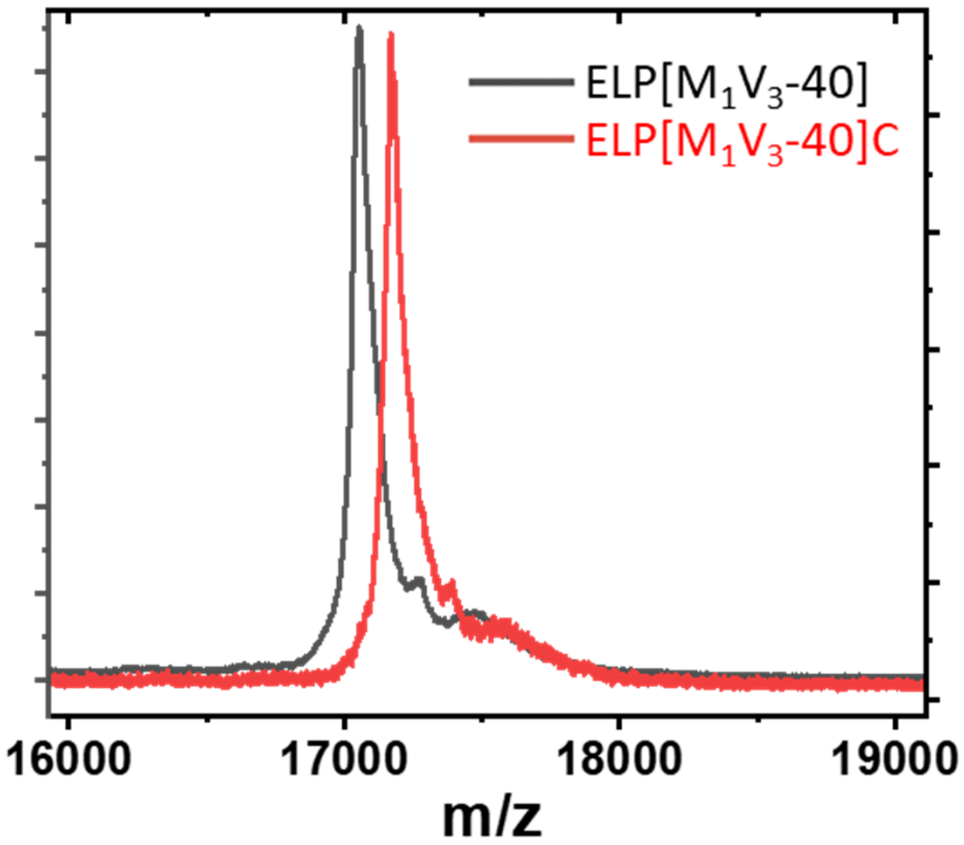

Figure S6: Superimposed MALDI mass spectra of ELP[M_1V_3-40] and ELP[M_1V_3-40]-C.

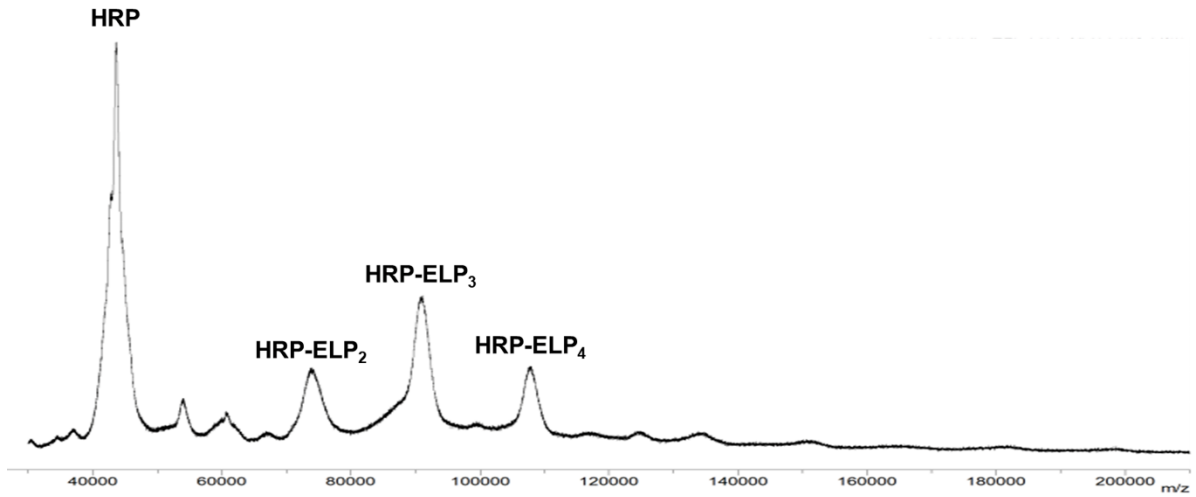

Figure S7: MALDI mass spectrum of ELP-b-HRP conjugate.

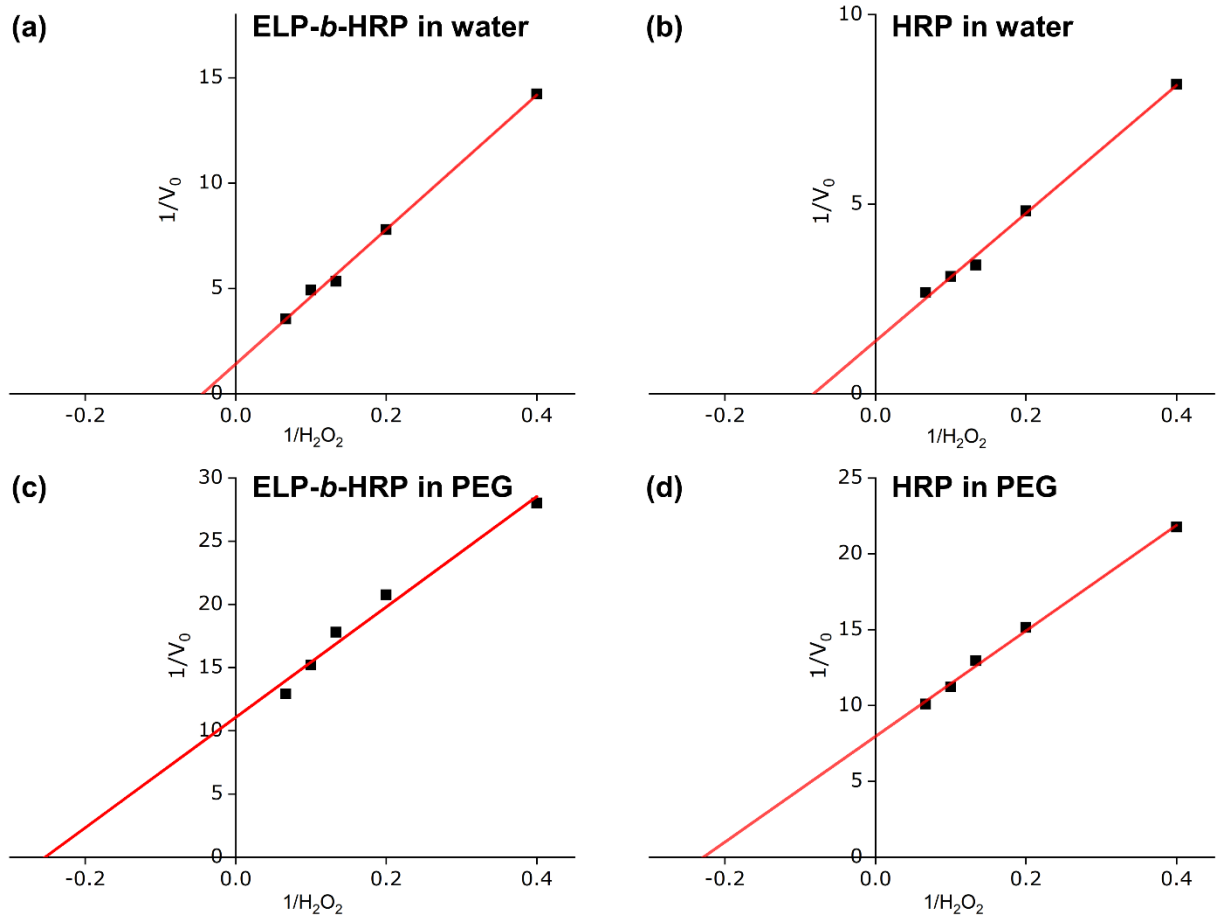

Figure S8: Lineweaver-Burk plots. Lineweaver Burk plots of ELP-b-HRP and HRP in water and PEG solution, respectively. The Michaelis Menten constant (K_m) of each condition was determined at the interception of the x axis, where x is -1/K_m.

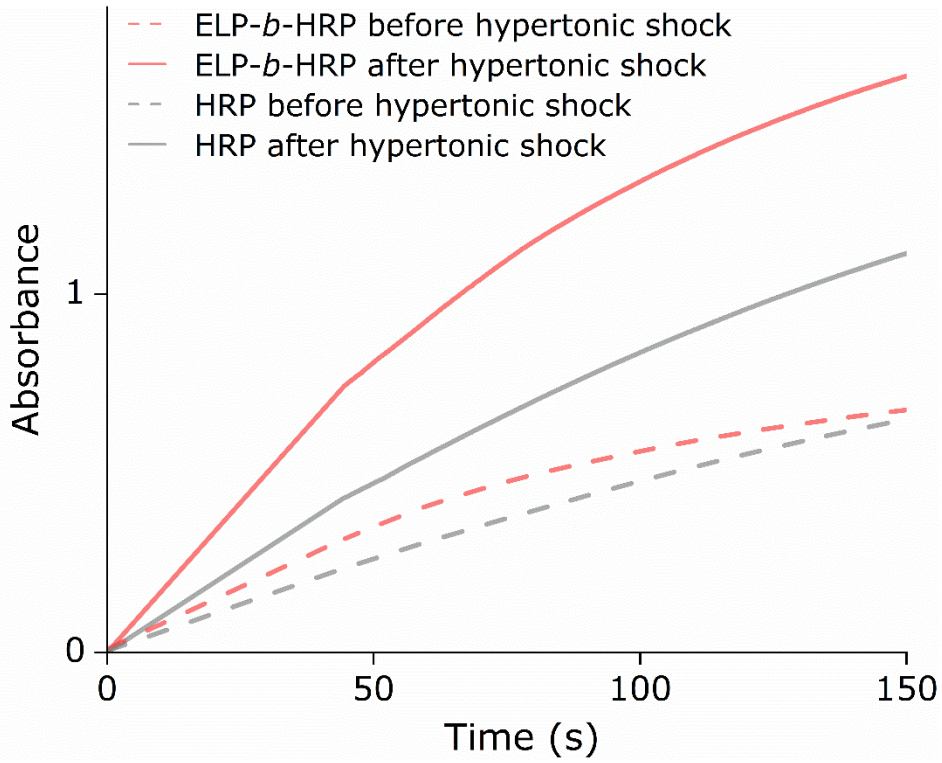

Figure S9: Kinetics of the enzymatic reaction using an alternative chemical substrate of ABTS determined by UV-Vis spectrometry.

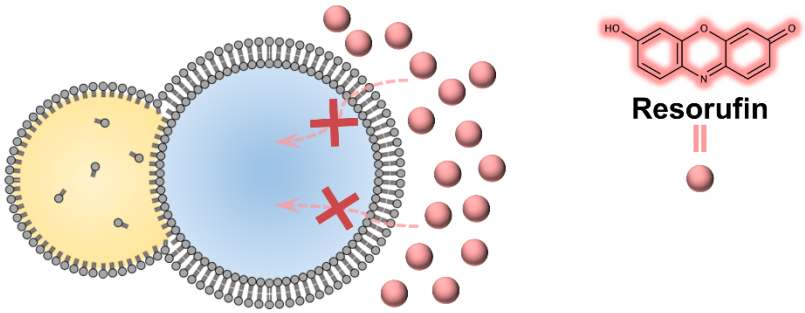
Resorufin

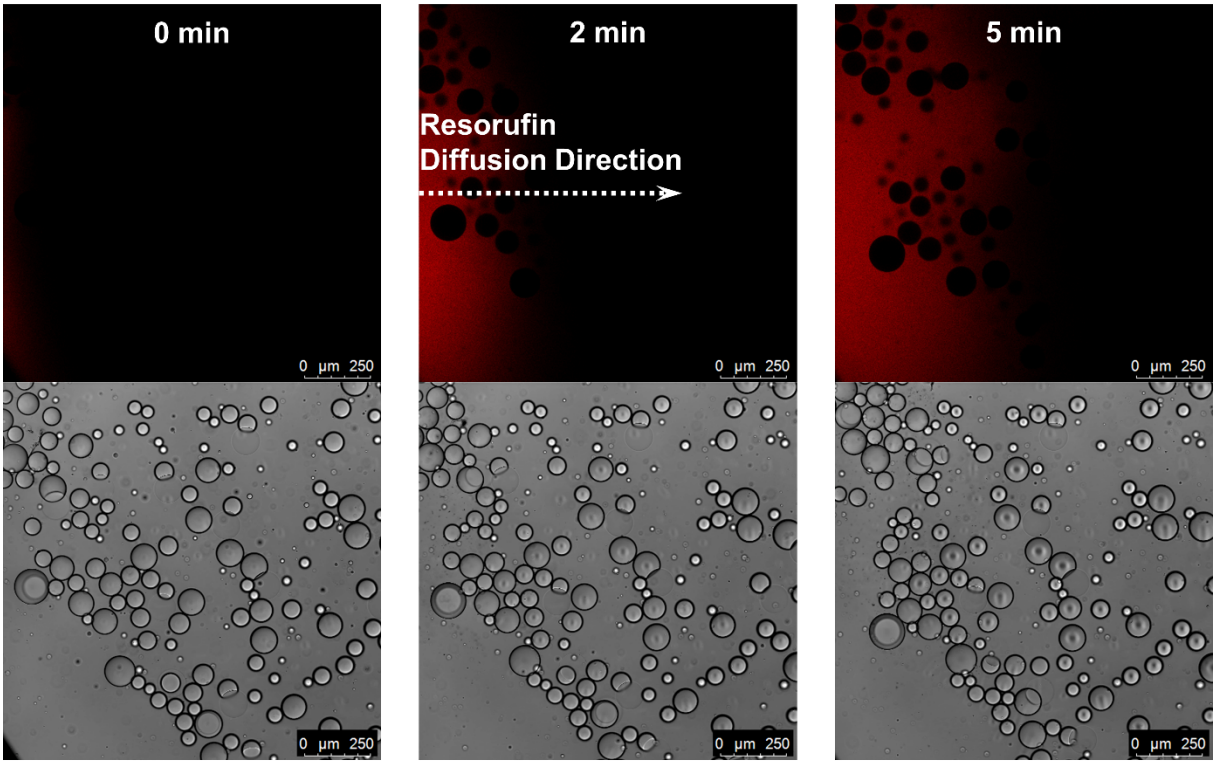
0 min
2 min
Resorufin
Diffusion Direction
5 min
10 min
15 min
20 min
0 µm 250

Figure S10: Permeability tests of the membrane towards resorufin. Illustration of non-permeable membranes to resorufin diffusing in the outer medium. Time series of confocal images (bright field and red channel) of monitoring resorufin diffusing in the sample. To assess the non-permeability of the membranes towards resorufin, partially dewetted liposomes, which have not been subjected to a hypertonic shock, were injected into an observation chamber and submitted to resorufin diffusion in the sample. After 20 min of observation, no resorufin was found to diffuse inside vesicles.

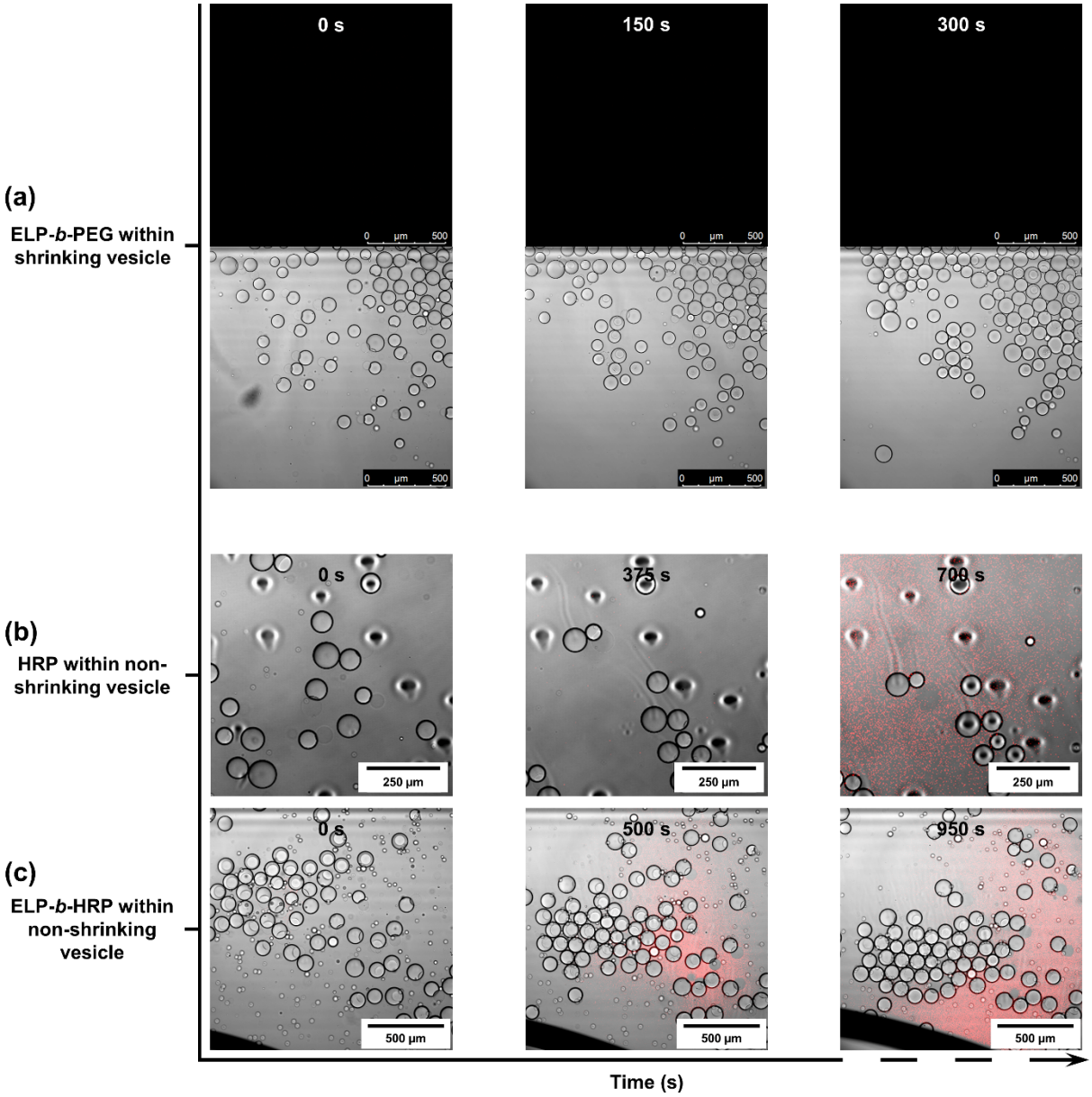

Figure S11: Enzymatic reaction of producing resorufin from amplex red in the absence/presence of the enzyme within shrinking or non-shrinking partially dewetted liposomes. (a) As a control, ELP-b-PEG to replace either free HRP or ELP-b-HRP was encapsulated inside the vesicles in the microfluidics process. 7 µL of partially dewetted vesicles were injected in an observation chamber, followed by an addition of 1 m_M H_2O_2 solution. The overall sample was monitored for 300 s,

without any detection of resorufin, proving that the HRP enzyme is needed to catalyze the reaction of producing resorufin. (b) HRP and (c) ELP-b-HRP were encapsulated respectively into liposomes which were not subjected to a hyperosmotic shock. Both of enzymatic reactions were monitored for over 10 min, without any visually imperceptible increase in fluorescence intensity being detected inside liposomes. The red background appeared over time as some vesicles bursted, releasing their inner content of amplex red and HRP/ELP-b-HRP, reacting with H_2O_2 and subsequently forming resorufin.

Table S1: Solution composition for spectrofluorescence analysis.

	Single HRP Before hypertonic shock	Single HRP After hypertonic shock	ELP-*b*-HRP Before hypertonic shock	ELP-*b*-HRP After hypertonic shock
HRP	0.054 n_M*	0.14 n_M	-	-
ELP-*b*-HRP	-	-	0.054 n_M*	0.14 n_M
ELP-*b*-PEG	-	-	0.125 mg ml^{-1}	0.325 mg ml^{-1}
BDP-ELP	-	-	0.250 mg ml^{-1}	0.65 mg ml^{-1}
Amplex Red	75 μ_M	195 μ_M	75 μ_M	195 μ_M
PEG	8 wt%	20.8 wt%	8 wt%	20.8 wt%
H_2O_2	75 μ_M	75 μ_M	75 μ_M	75 μ_M

*In the spectrofluorometer analysis, the concentration is 0.054 n_M for both free HRP and ELP-*b*-HRP, while in the scenario of inducing enzymatic reaction within partially dewetted liposomes, the concentration for both free HRP and ELP-*b*-HRP is increased by 10-fold to 0.54 n_M.

Supplementary Videos S1

Video S1. Enzymatic reaction within shrunken partially dewetted liposomes catalyzed either by HRP alone or by ELP-*b*-HRP.

6. References

[1] J. W. Szostak, D. P. Bartel, P. L. Luisi, *Nature* **2001**, *409*, 387.

[2] a) R. Roodbeen, J. C. M. van Hest, *Bioessays* **2009**, *31*, 1299; b) P. A. Beales, B. Ciani, S. Mann, *Interface Focus* **2018**, *8*, 20180046; c) M. Marguet, C. Bonduelle, S. Lecommandoux, *Chem. Soc. Rev.* **2013**, *42*, 512.

[3] a) N.-N. Deng, M. Yelleswarapu, L. Zheng, W. T. S. Huck, *J. Am. Chem. Soc.* **2017**, *139*, 587; b) A. Peyret, E. Ibarboure, N. Pippa, S. Lecommandoux, *Langmuir* **2017**, *33*, 7079; c) R. J. R. W. Peters, M. Marguet, S. Marais, M. W. Fraaije, J. C. M. van Hest, S. Lecommandoux, *Angew. Chem. Int. Ed.* **2014**, *53*, 146.

[4] a) N. G. Moreau, N. Martin, P. Gobbo, T. Y. D. Tang, S. Mann, *Chem. Commun.* **2020**, *56*, 12717; b) W. Mu, Z. Ji, M. Zhou, J. Wu, Y. Lin, Y. Qiao, *Sci. Adv. 7*, eabf9000.

[5] C. P. Brangwynne, C. R. Eckmann, D. S. Courson, A. Rybarska, C. Hoege, J. Gharakhani, F. Jülicher, A. A. Hyman, *Science* **2009**, *324*, 1729.

[6] a) S. F. Banani, H. O. Lee, A. A. Hyman, M. K. Rosen, *Nat. Rev. Mol. Cell Biol.* **2017**, *18*, 285; b) D. Bracha, M. T. Walls, C. P. Brangwynne, *Nat. Biotechnol.* **2019**, *37*, 1435; c) J. Liu, F. Zhorabek, Y. Chau, *Matter* **2022**, *5*, 2787; d) A. A. Hyman, C. A. Weber, F. Jülicher, *Annu. Rev. Cell Dev. Biol.* **2014**, *30*, 39.

[7] W. Stroberg, S. Schnell, *Biophys. J.* **2018**, *115*, 3.

[8] M. B. Burg, J. D. Ferraris, N. I. Dmitrieva, *Physiol. Rev.* **2007**, *87*, 1441.

[9] a) C. Gao, J. Gu, H. Zhang, K. Jiang, L. Tang, R. Liu, L. Zhang, P. Zhang, C. Liu, B. Dai, J. Song, *Cell Rep.* **2022**, *40*, 111086; b) C. R. Boyd-Shiwarski, D. J. Shiwarski, S. E. Griffiths, R. T. Beacham, L. Norrell, D. E. Morrison, J. Wang, J. Mann, W. Tennant, E. N. Anderson, J. Franks, M. Calderon, K. A. Connolly, M. U. Cheema, C. J. Weaver, L. J. Nkashama, C. C. Weckerly, K. E. Querry, U. B. Pandey, C. J. Donnelly, D. Sun, A. R. Rodan, A. R. Subramanya, *Cell* **2022**, *185*, 4488; c) W. van Leeuwen, C. Rabouille, *Traffic* **2019**, *20*, 623; d) A. P. Jalihal, S. Pitchiaya, L. Xiao, P. Bawa, X. Jiang, K. Bedi, A. Parolia, M. Cieslik, M. Ljungman, A. M. Chinnaiyan, N. G. Walter, *Mol. Cell* **2020**, *79*, 978.

[10] a) C. Xu, N. Martin, M. Li, S. Mann, *Nature* **2022**, *609*, 1029; b) N.-N. Deng, W. T. S. Huck, *Angew. Chem. Int. Ed.* **2017**, *56*, 9736; c) H. Zhao, E. Ibarboure, V. Ibrahimova, Y. Xiao, E. Garanger, S. Lecommandoux, *Adv. Sci.* **2021**, *8*, 2102508; d) H. Zhao, V. Ibrahimova, E. Garanger, S. Lecommandoux, *Angew. Chem. Int. Ed.* **2020**, *59*, 11028; e) A. T. Rowland, D. N. Cacace, N. Pulati, M. L. Gulley, C. D. Keating, *Chem. Mater.* **2019**, *31*, 10243; f) J. W. Hindley, D. G. Zheleva, Y. Elani, K. Charalambous, L. M. C. Barter, P. J. Booth, C. L. Bevan, R. V. Law, O. Ces, *Proc. Natl. Acad. Sci.* **2019**, *116*, 16711; g) S. Deshpande, F. Brandenburg, A. Lau, M. G. F. Last, W. K. Spoelstra, L. Reese, S. Wunnava, M. Dogterom, C. Dekker, *Nat. Commun.* **2019**, *10*, 1800; h) H. Seo, H. Lee, *Nat. Commun.* **2022**, *13*, 5179; i) T. E. Miller, T. Beneyton, T. Schwander, C. Diehl, M. Girault, R. McLean, T. Chotel, P. Claus, N. S. Cortina, J.-C. Baret, T. J. Erb, *Science* **2020**, *368*, 649; j) S. Cao, L. C. da Silva, K. Landfester, *Angew. Chem. Int. Ed.* **2022**, *61*, e202205266.

[11] a) J. R. Simon, S. A. Eghtesadi, M. Dzuricky, L. You, A. Chilkoti, *Mol. Cell* **2019**, *75*, 66; b) A. Belluati, S. Thamboo, A. Najer, V. Maffeis, C. von Planta, I. Craciun, C. G. Palivan, W. Meier, *Adv. Funct. Mater.* **2020**, *30*, 2002949; c) R. Booth, Y. Qiao, M. Li,

S. Mann, *Angew. Chem. Int. Ed.* **2019**, *58*, 9120; d) A. F. Mason, N. A. Yewdall, P. L. W. Welzen, J. Shao, M. van Stevendaal, J. C. M. van Hest, D. S. Williams, L. K. E. A. Abdelmohsen, *ACS Cent. Sci.* **2019**, *5*, 1360; e) C. L. Cuevas-Velazquez, T. Vellosillo, K. Guadalupe, H. B. Schmidt, F. Yu, D. Moses, J. A. N. Brophy, D. Cosio-Acosta, A. Das, L. Wang, A. M. Jones, A. A. Covarrubias, S. Sukenik, J. R. Dinneny, *Nat. Commun.* **2021**, *12*, 5438.

[12] E. Rideau, R. Dimova, P. Schwille, F. R. Wurm, K. Landfester, *Chem. Soc. Rev.* **2018**, *47*, 8572.

[13] a) C. Vanhille-Campos, A. Šarić, *Soft Matter* **2021**, *17*, 3798; b) M. Yanagisawa, M. Imai, T. Taniguchi, *Phys. Rev. Lett.* **2008**, *100*, 148102.

[14] N.-N. Deng, M. A. Vibhute, L. Zheng, H. Zhao, M. Yelleswarapu, W. T. S. Huck, *J. Am. Chem. Soc.* **2018**, *140*, 7399.

[15] D. E. Meyer, A. Chilkoti, *Nat. Biotechnol.* **1999**, *17*, 1112.

[16] D. W. Urry, *J. Phys. Chem. B.* **1997**, *101*, 11007.

[17] a) R. Petitdemange, E. Garanger, L. Bataille, K. Bathany, B. Garbay, T. J. Deming, S. Lecommandoux, *Bioconj. Chem.* **2017**, *28*, 1403; b) Y. Xiao, Z. S. Chinoy, G. Pecastaings, K. Bathany, E. Garanger, S. Lecommandoux, *Biomacromolecules* **2020**, *21*, 114.

[18] a) S. B. Zimmerman, A. P. Minton, *Annu. Rev. Biophys. Biomol. Struct.* **1993**, *22*, 27; b) C. D. Keating, *Acc. Chem. Res.* **2012**, *45*, 2114.

[19] P. Baumann, M. Spulber, O. Fischer, A. Car, W. Meier, *Small* **2017**, *13*, 1603943.

[20] A. Belluati, I. Craciun, J. Liu, C. G. Palivan, *Biomacromolecules* **2018**, *19*, 4023.

[21] H. Bisswanger, *Perspect. Sci.* **2014**, *1*, 41.

[22] W. M. Aumiller, Jr., B. W. Davis, E. Hatzakis, C. D. Keating, *J. Phys. Chem. B.* **2014**, *118*, 10624.

[23] R. Chong, J.-E. R. Rho, H.-J. Yoon, P. S. Park, T.-H. D. Rho, J. Y. Park, L. Park, Y.-H. Kim, J. H. Lee, *Talanta* **2013**, *116*, 403.

Supplementary References

[1] A. S. Utada, E. Lorenceau, D. R. Link, P. D. Kaplan, H. A. Stone, D. A. Weitz, *Science* **2005**, *308*, 537.

[2] a) R. Petitdemange, E. Garanger, L. Bataille, K. Bathany, B. Garbay, T. J. Deming, S. Lecommandoux, *Bioconj. Chem.* **2017**, *28*, 1403; b) R. Petitdemange, E. Garanger, L. Bataille, W. Dieryck, K. Bathany, B. Garbay, T. J. Deming, S. Lecommandoux, *Biomacromolecules* **2017**, *18*, 544.

[3] Y. Xiao, Z. S. Chinoy, G. Pecastaings, K. Bathany, E. Garanger, S. Lecommandoux, *Biomacromolecules* **2020**, *21*, 114.

[4] N. Mogharrab, H. Ghourchian, M. Amininasab, *Biophys. J.* **2007**, *92*, 1192.

[5] J. Schindelin, I. Arganda-Carreras, E. Frise, V. Kaynig, M. Longair, T. Pietzsch, S. Preibisch, C. Rueden, S. Saalfeld, B. Schmid, J.-Y. Tinevez, D. J. White, V. Hartenstein, K. Eliceiri, P. Tomancak, A. Cardona, *Nat. Methods* **2012**, *9*, 676.

Chapter IV – Compartmentalization of Enzymes within Coacervates, Characterization using FCS, Impact on Kinetics of Reaction

1. Introduction

Cells are intricate self-assembled structures, that use compartmentalization as a mean to partition their biomolecular content, regulate and carry out internal processes, crucial for their growth and survival.[1–3] Two main subcompartments can be found within eukaryotic cells, namely membranebound and membraneless organelles. Since their discovery by Brangwynne et al. in 2009,[4] membraneless organelles have gained significant attention in cell biology research. These compartments arise through a process called liquid-liquid phase separation (LLPS), involving RNA and intrinsically disordered proteins (IDPs), in response to biological variations in cytoplasmic pH, temperature or osmotic stress.[5,6] As such, stress granules and Cajal bodies are only few examples of these types of organelles. To synthetically reproduce membraneless structures, coacervates have been used as compartments that can sequester and concentrate a wide range of solutes, and their spontaneous formation makes coacervates interesting membraneless models.[7] Coacervates can be formed through both associative and simple phase separation processes. On one hand, associative phase separation involves attractive interactions between two soluble (macro)molecules, such as polyelectrolytes, leading to the formation of complex coacervates. On the other hand, simple phase separation occurs due to attractive interactions within a single (macro)molecule, resulting in the assembly of simple coacervates.[8] As they possess sequences of low complexity and are structurally similar to IDPs in cellular assemblies,[9] elastin-like polypeptides (ELPs) have been proposed as a relevant simplified model of IDPs.[10] They are sequences of (VPGXG) pentapeptides where the guest residue X can be any amino acid except for proline, and are recombinantly produced in Escherichia coli.[11] They exhibit a lower critical solubility temperature (LCST) in water, meaning that below their cloud point temperature (T_{cp}),

they are miscible in water and above their cloud point temperature, they phase separate and form coacervates.[11,12] The T_{cp} can be tuned mostly by controlling the amino acid repeat sequence and polymer length.[13]

In their work, Love et al.,[14] Booth et al.,[15] and Deshpande et al.[16] have been using pH variation or transmembrane diffusion to induce the LLPS of polyelectrolytes and assemble coacervates. Their results showed that segregation and specific accumulation of biomolecules occurred inside their coacervates. They also evidenced the role of coacervates as reaction centers as they enhance enzymatic reactivity by selectively trapping, creating a beneficial environment, and locally increasing the enzymes and substrates concentration. In the case of Deshpande's experiments, the fluorescein intensity within the coacervate phase increased roughly 14-fold over a course of a 2 h experiment. To monitor this enzymatic activity, authors commonly use fluorescence spectroscopy to quantitatively measure the transformation of a reactant into a fluorescent product, while confocal microscopy is generally employed to observe the distribution of labelled enzymes within the coacervates. In a recent contribution, Garenne et al.[17] used epifluorescence microscopy to visualize the encapsulation of proteins in their coacervates, and UV-Vis spectroscopy to quantify the amount of protein sequestered within the coacervates. To the best of our knowledge, Fluorescence Correlation Spectroscopy (FCS) has never been used in the literature to characterize the capacity of ELP coacervates to partition labelled enzymes. In this contribution, we furtherly deepen our understanding upon the ELP coacervates that have been used in **Chapter III**, by qualitatively demonstrating their capacity to partition certain molecules, and observe how this partitioning can influence the kinetics of enzymatic reactions.

2. Results and discussion

2.1. Partitioning of enzyme in coacervates by Fluorescence Correlation Spectroscopy (FCS)

To demonstrate the ability of ELP coacervates to sequester different enzymes, Fluorescence Correlation Spectroscopy (FCS) analyses were conducted. We thus compared the characteristic diffusion times of free fluorescent dyes (Atto-488 and Rhodamine) and fluorescently labeled enzymes (GOx-Atto 488 and HRP-Rhodamine) with or without the presence of coacervates. The coacervates are resulting from the phase separation of ELPs as detailed before. All experiments were thus conducted at 37°C, a temperature above the T_{cp} of the ELP that was also fluorescently

labelled with Bdpi. One could first confirm the presence of coacervates formed from the increase of diffusion time (τ_D) of ELP-Bdpi (from 305 µs to 2349 µs) (Table S1, Figure S3). Then, as illustrated in

Figure *47*, the normalized FCS auto-correlation curves of tagged GOx and HRP showed a shift towards higher τ_D (629 µs and 230 µs respectively) compared to free dyes (40 µs and 21 µs respectively for Atto 488 and Rhodamine), indicating successful labeling of these biomacromolecules. A significant increase in the diffusion time of the fluorescently labelled enzymes could then be observed in the presence of the coacervates, indicating the association between these compounds. Even if these observations are qualitatively clear, it must be noted that the τ_D values for GOx-Atto 488 and HRP-Rhodamine in coacervates are different (33669 µs and 44708 µs respectively). This could be due to several factors, including the evaporation in the analysis chamber and the uncontrolled size of the coacervates formed, that imped a more quantitative analysis.

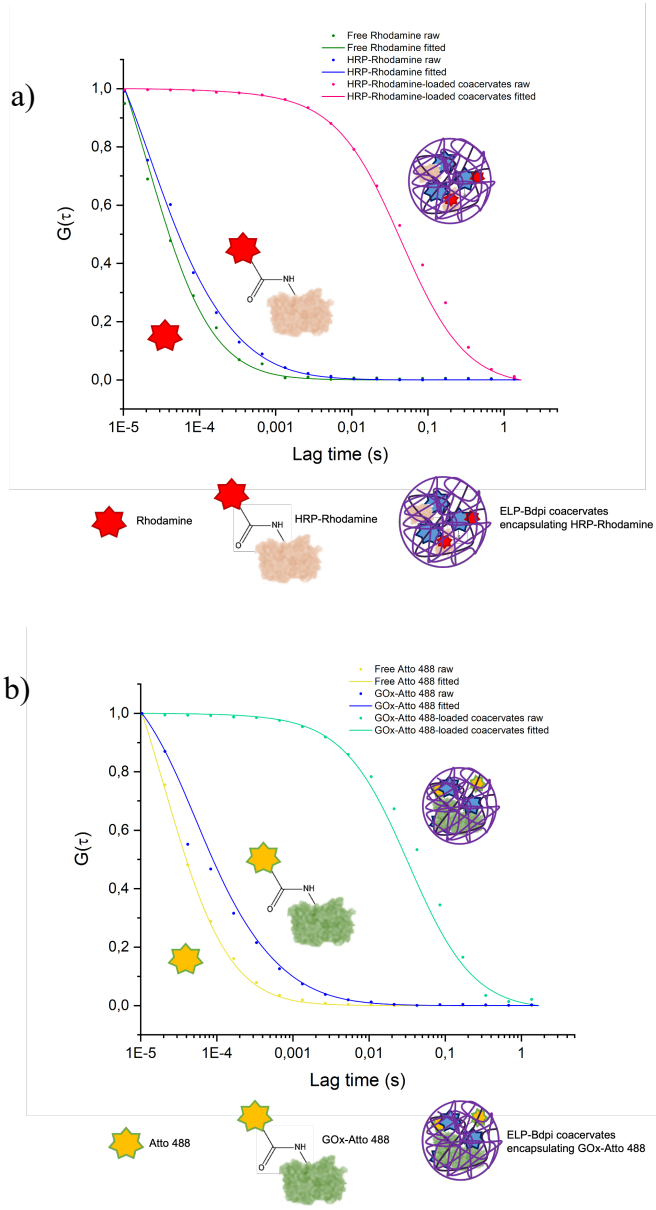

Figure 47: a) Normalized FCS autocorrelation curves of free rhodamine dye (green), rhodamine-tagged HRP (blue) and Bdpi-tagged coacervates encapsulating HRP-Rhodamine (pink) b) Normalized FCS autocorrelation curves of free Atto 488 dye (yellow), Atto 488-tagged GOx (blue) and Bdpi-tagged coacervates encapsulating GOx-Atto 488 (green). Dots: raw. Solid lines: fitted curves.

2.2. Enzyme and coacervate co-localization by Fluorescence cross-correlation spectroscopy (FCCS)

Figure 48 reports the autocorrelation curves of GOx-Atto 488 (blue) and coacervated ELP-Bdpi (green), without normalizing the results. Fluorescence cross-correlation spectroscopy (FCCS) analysis (orange) was performed as both compounds could be fluorescently labelled with different fluorophores. The results showed that the coacervated ELP-Bdpi successfully entrapped GOx-Atto 488, as an increase in the cross-correlation between the fluorescently labelled species was observed. As a control, Atto 488 and Bdpi (black) FCCS was performed. The absence of signal confirmed that the two compounds did not diffuse together.

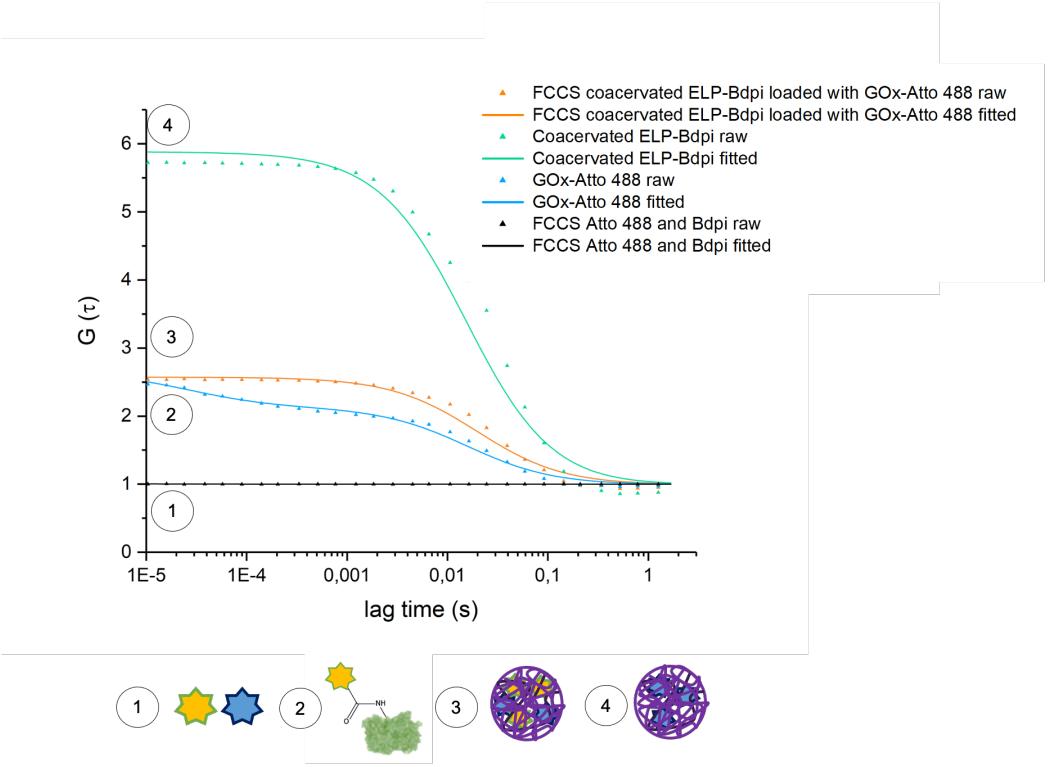

Figure 48: FCS autocorrelation curves of GOx-Atto 488 (blue), coacervated ELP-Bdpi (green), FCCS autocorrelation curve of coacervated ELP-Bdpi loaded with GOx-Atto 488 (orange), and FCCS autocorrelation curve control of free dyes Atto 488 and Bdpi (black). Triangles: raw. Solid lines: fitted curves.

Finally, a picture from the ZEISS ZEN software was taken to support these findings (Figure 49). The red peaks correspond to the coacervates crossing the detector during the analysis. In the zoom of the selected peak, a smaller blue peak appears, corresponding to the labeled enzyme. This demonstrates once again that the two compounds diffuse together at the same time, meaning that the tagged-enzyme is entrapped withing the labelled-coacervate.

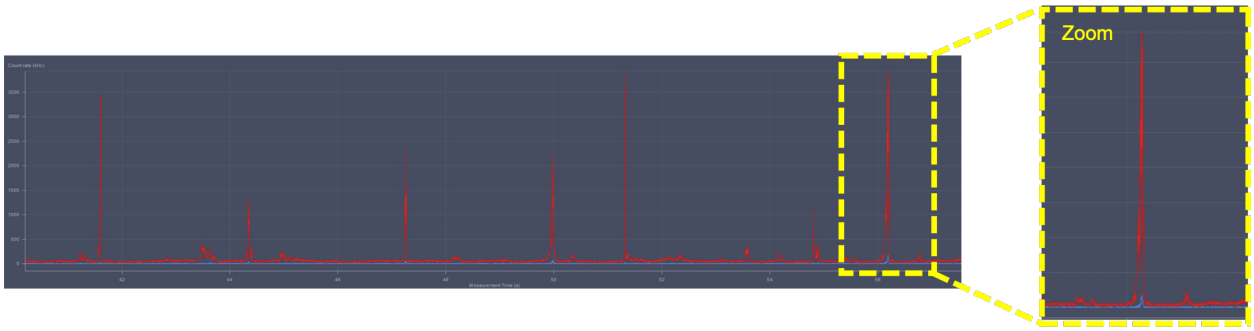

Figure 49: Picture from the ZEN program were the red peaks correspond to the coacervates and the blue peaks correspond to the Atto 488-labelled GOx respectively crossing the detector. The zoomed peak demonstrates the colocalization and co-diffusion of a coacervate and GOx-Atto 488 molecule.

2.3. Kinetics of enzymatic reactions in the presence/absence of coacervates

A single enzyme and two-enzyme cascade reactions were then performed to evaluate the effect of confinement of the enzyme in organelle-like systems, thus mimicking very closely cells' behaviour.[18,19] To create a cell-like crowed environment, enzymatic kinetics were measured in an 8 wt% PEG solution and ELP[M_1V_3-80] was added (1 mg.mL^{-1}) as previously reported.[20,21] The T_{cp} of ELP[M_1V_3-80] in these conditions was determined by Dynamic Light Scattering (DLS), exhibiting a T_{cp} of 18°C (Figure S4). To compare the kinetics of reaction, experiments were thus conducted below the T_{cp} of the ELP (13°C) in conditions where the ELP is fully soluble, and above the T_{cp} (25°C), in coacervate state.

First, the HRP enzymatic kinetics was analyzed. Amplex red should be oxidized by hydrogen peroxide (H_2O_2) through the catalysis of HRP to produce resorufin as a fluorescent probe. As seen in Figure 50, below the T_{cp} the kinetics of the reactions were comparable between the systems with and without ELPs, as the slopes of the curves were similar (Table 2). Also, the final fluorescence

intensity of the reaction was equivalent in both cases, proving that an equivalent concentration of HRP was used. In the conditions following the assembly of synthetic organelles, above the T_{cp}, the slope of the solution containing the ELP coacervates was much steeper (22.40 ± 0.82 a.u.·s^{-1}) than the one devoid of ELPs (11.85 ± 0.93 a.u.·s^{-1}), suggesting that the formation of synthetic organelles locally concentrated the enzyme and the amplex red, ensuring a faster enzymatic reaction. The steep decline in the red curve could potentially be attributed to the lack of ELP-*b*-PEG in the system. Indeed, as previously demonstrated,[22] ELP-*b*-PEG ensures the stabilization of coacervates, acting as a surfactant. Consequently, it is possible that the coacervates continue to grow throughout the enzymatic reaction and eventually settle at the bottom of the cuvette, resulting in a drop of fluorescence production. As a control, the kinetics of reaction were performed without using ELPs, to prove that heating was not inducing higher kinetics of reaction.

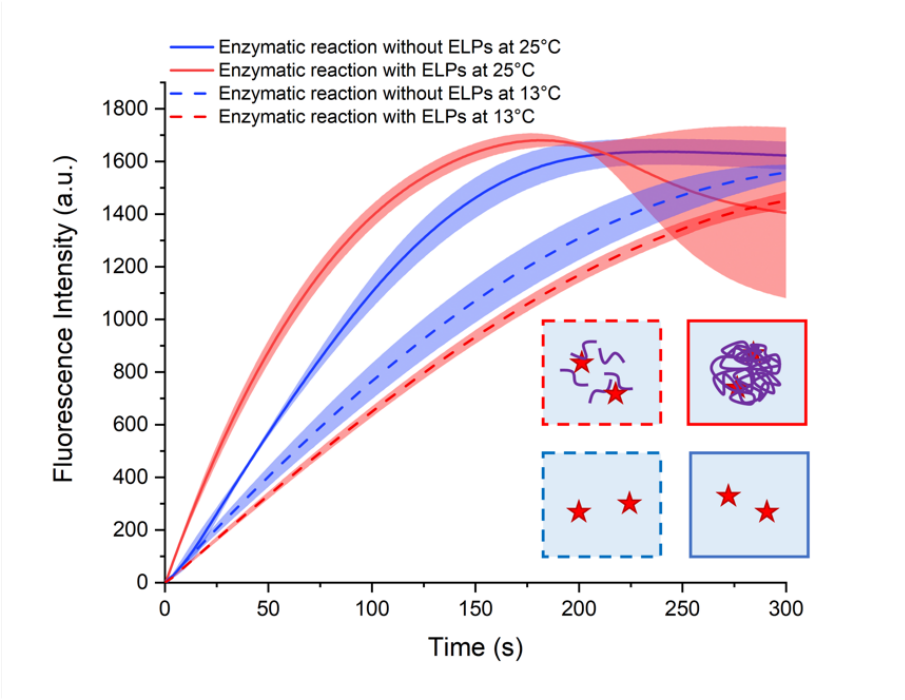

Figure 50: Kinetics of the HRP enzymatic reaction within ELP-based coacervates and free ELP systems, before and after inducing the coacervate assembly using temperature, reactions are monitored by the increase of fluorescence intensity detected with spectrofluorometer.

Table 2: Slope of the fluorescence intensity curves versus time for the HRP enzymatic reaction.

Solution	Slope (a.u.·s^{-1}) from (t = 0)
Enzymatic reaction without ELP 25°C	11.85 ± 0.93
Enzymatic reaction with ELP 25°C	22.40 ± 0.82
Enzymatic reaction without ELP 13°C	7.85 ± 0.77
Enzymatic reaction with ELP 13°C	6.55 ± 0.21

In a second step, a two-enzyme reaction was tested. When GOx is added, the enzyme catalyzes the oxidation of β-d-glucose to β-d-glucono-1,5-lactone and H_2O_2, which is furtherly used as a substrate to HRP for the oxidization of amplex red. The kinetic analysis of such cascade reaction is presented in Figure 51. In this case, the kinetics were surprisingly very similar whether there are coacervates or not (Table 3).

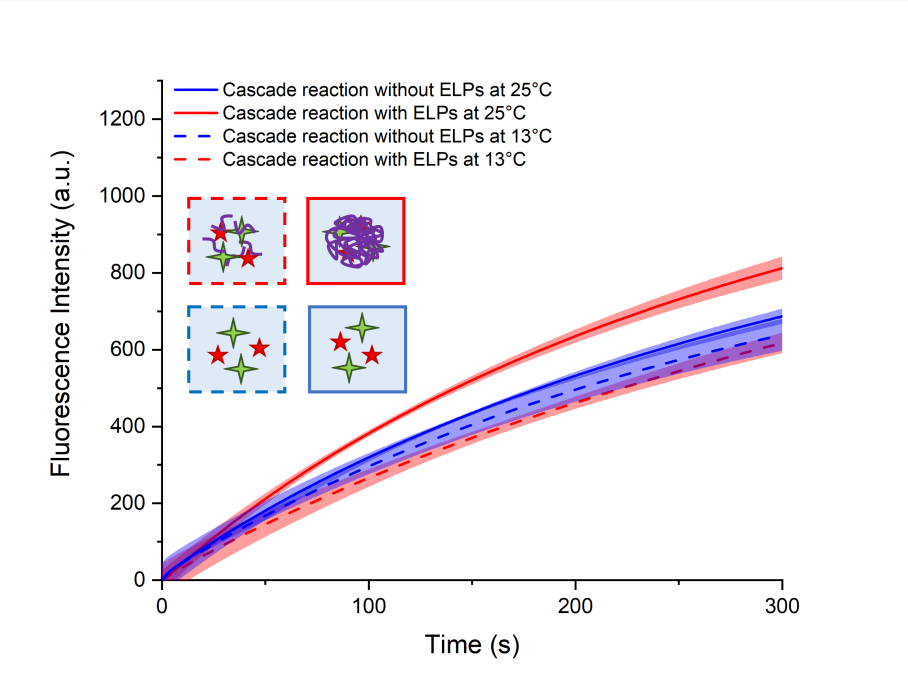

Figure 51: Kinetics of the GOx-HRP cascade reaction of ELP-based coacervates and free HRP system before and after inducing the coacervate assembly using temperature, reactions monitored by the increase of fluorescence intensity detected with spectrofluorometer.

Table 3: Slope of the fluorescence intensity curves versus time for the GOx-HRP cascade reaction

Solution	Slope (a.u.·s^{-1}) from (t = 0)
Cascade reaction without ELP 25°C	3.39 ± 0.60
Cascade reaction with ELP 25°C	4.30 ± 0.59
Cascade reaction without ELP 13°C	2.93 ± 0.24
Cascade reaction with ELP 13°C	2.79 ± 0.44

Actually, the main reasons for kinetics increase are the improved affinity of the enzyme and the substrate and their closed localization, limiting diffusion times.[22] Here, one can hypothesize that the enzymes might be localized in different coacervates and not necessarily co-localized in same coacervates. To evaluate this hypothesis, confocal microscopic experiments were conducted. First, GOx-Atto 488 and HRP-Rhodamine solutions (with 1 mg mL^{-1} ELP in 8 wt % PEG) were prepared separately (Figure 6 a and b). The solutions were heated to assemble the coacervates, and the tagged enzymes could be observed inside of the formed membraneless organelles. Then, the two enzymes were mixed together in a new batch of coacervates (Figure 52c). Co-localization, denoted by the yellow spots (circled for a better visibility), was observed only for a few coacervates, which could explain the previous results. As seen in Figure 5**Error! Reference source not found.**, the kinetics of the enzymatic reaction were mildly accelerated in the presence of the coacervates as only few of HRP and GOx were colocalized within a same coacervate. This makes their accessibility and interactions difficult, as well as increase the distance between the reactants and enzymes.

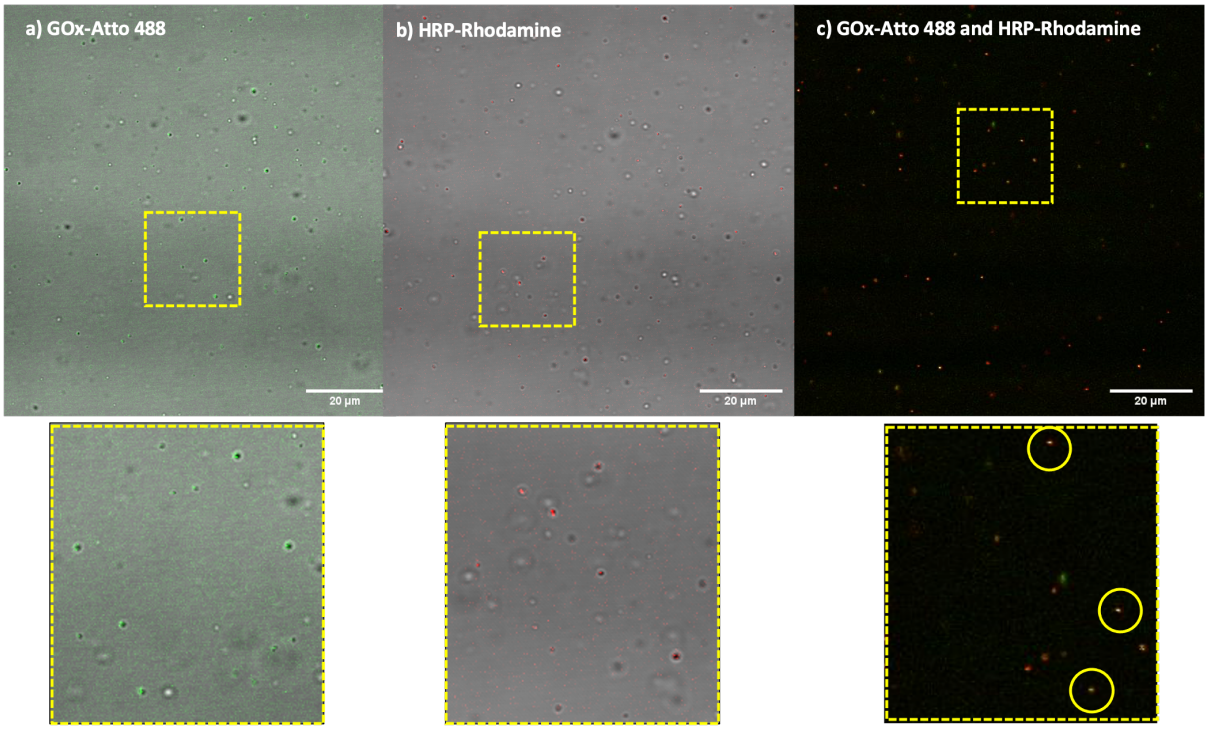

Figure 52: a) GOx-Atto 488 and b) HRP-rhodamine encapsulated within ELP coacervates c) Both enzymes entrapped together.

3. Conclusion

To conclude, we have been utilizing fluorescence correlation spectroscopy to demonstrate the uptake of labelled enzymes into our ELP coacervates, enhancing our understanding of these systems compared to our earlier investigation. Through the kinetic analysis, we have gained insight into the limited likelihood of co-encapsulating two enzymes within a single coacervate, enhanced by confocal microscopy observations. To potentially address this issue, the size of the coacervates could be increased to have higher probabilities of having several enzymes into one coacervates. The other possible solution could involve conjugating each enzyme to an ELP, as it was done in our previous work. Indeed, we previously demonstrated that having a single conjugated enzyme, HRP-b-ELP, did not clearly impact the kinetics of reaction compared to free HRP with free ELP, but in the case of two enzymes in a same system, having them conjugated to an ELP could increase the chances of having them together in a same coacervate. This breakthrough creates exciting opportunities for developing artificial cells from the bottom-up assembly and for exploring novel

functions and interactions between these two types of organelles, much like a natural eukaryotic cell would do.

4. Materials and Methods

Materials: Poly(ethylene glycol) (PEG, 6 kDa) polymer was purchased from Alfa Aesar. Ampliflu™ red (HPLC grade, 96%), the enzyme of horseradish peroxidase (HRP, hydrophilized powder, 150 $U.mg^{-1}$), the enzyme of glucose oxidaze (GOx, 100,000-250,000 U/g, solid), rhodamine-labelled HRP, rhodamine, D-(+)-Glucose (GC, 99.5%), Sodium bicarbonate (ACS reagent, ≥99.7%), Sodium hydroxide were purchased from Sigma Aldrich. Hydrogen peroxide (H_2O_2, 35%) was purchased from Acros. Atto 488 NHS-ester was bought from Atto-TEC. All compounds were used as received without further purification. Dimethyl sulfoxide (DMSO, 99.9%) was purchased from Sigma-Aldrich and used without further purification. Water with a resistivity of 18.2 $M\Omega.cm^{-1}$ was prepared using a Millipore Milli-Q system.

Bioproduction, isolation and purification of ELPs: The ELPs were produced by recombinant DNA and protein engineering techniques in *E. coli* and isolated using previously reported procedures.[23,24] The bioconjugate of ELP-*b*-PEG was produced and isolated as previously reported.[25] ELP[M_1V_3-40], ELP[M_1V_3-40]-Cysteine, ELP[M_1V_3-60] and ELP-PEG were used for FCS experiments; ELP[M_1V_3-80] was used for the rest of the experiments.

Determination of the cloud point temperature (T_{cp}) of ELP[M1V3-80] by dynamic light scattering (DLS): To determine the cloud point temperatures, the scattered light from solutions of ELP[M1V3-80] at 1 $mg.mL^{-1}$ in a 8 wt% PEG were performed on NanoZS instrument (Malvern, U.K) at a 173° angle, at a constant position in the cuvette (constant scattering volume), following a protocol described in detail elsewhere.[22] Briefly, the derived count rate (DCR) was defined as the mean scattered intensity normalized by the attenuation factor. The DCR was plotted against temperature and the T_{cp} is defined as the temperature corresponding to the point where the DCR starts increasing on the plot. Temperature ramps were performed from 5 °C to 50 °C for all conditions.

Determination of kinetics of enzymatic reactions in bulk by fluorescence spectrofluorometer: Measurements were carried out in bulk solution, in a high precision quartz glass cell from Hellma Analytics, simulating the inside environment of a vesicle. Experiments were conducted at 13 °C and 25 °C, before and after inducing the coacervation state of the ELP[M1V3-80] using temperature as a trigger. All the compounds constituting the solutions were thoroughly mixed in an Eppendorf tube and pipetted into the cuvette. Lastly, 1 m_M H_2O_2/ 1 m_M glucose stock solution was added and quickly mixed to the solution, before starting monitoring the increase in fluorescence intensity. Each experiment was repeated three times. Values were averaged and standard deviations calculated. To conduct these experiments, the fluorescence spectrometer (Jasco FP-8500) was used in the course measurement mode. To detect the produced resorufin, excitation and emission wavelength were set at 470 and 590 nm respectively.

Conjugation of fluorescently labelled ELP[M1V3-60] and enzymes: The synthesis and purification of fluorescently labeled ELP[M1V3-60] was performed by following a protocol described elsewhere.[26] DIPEA (1 equiv.) was added to a solution of ELP[M1V3-60] (20 mg) in anhydrous DMSO (2 mL). After stirring the solution, BDP 630/650 X NHS ester (2 equiv.) was added and the reaction was left under stirring for 24 hours at room temperature under Ar in the dark. Then the mixture was precipitated into diethyl ether and centrifuged. Precipitate was dissolved in cold water and purified by ITC. The final pale blue product BDP-ELP[M1V3-60] was obtained by lyophilisation. (19 mg, 95% product yield). To purify the fluorescent ELP product by ITC, precipitate was dissolved in 2 mL cold water and a few drops of 1.5 M NaCl solution was added into the solution. Tube was placed in heating bath (40°C) to fluctuate products and enhance the separation from free dye molecules. Solution was centrifuged 30 minutes at 38°C (3800 rpm speed) and supernatant was discarded. The dark blue pellet was dissolved in 3 mL cold water and few drops of 1.5 M NaCl solution was added into the supernatant and placed into the heating bath (40°C) and centrifuged 30 minutes at 38°C (3800 rpm speed). This process is repeated until the clear supernatant has been observed. Finally, the supernatant was discarded, and the pellet was dissolved in cold Milli-Q water. To remove the excess salt, the solution was washed three times with cold water by ultrafiltration technique. The final solution was lyophilized to obtain pure pale blue BDP- ELP[M1V3-60].

In a typical example, the labelling of the GOx protein with an amine-reactive Atto 488-label (Figure S1) was performed following the Atto-TEC protocol.[27] Briefly, a 0.2 M sodium bicarbonate solution was adjusted to pH 9 using a 2 M sodium hydroxide solution. Then, 13 µl of this solution was mixed with 50 µl of a 2 mg mL^{-1} GOx solution in water, and 100 µl of a 50 µM Atto 488 solution. The solution was left in the dark, under stirring for 48 h in a 4°C fridge. Purification of the solution was then performed using PD miditrap G-25 from Cytiva, and 30 K centrifugal filters, to remove any unconjugated dye. Labelled HRP-rhodamine was store-bought and used as received.

Determination of % of conjugation of GOx with Atto 488: To determine how much Atto 488 was conjugated to the GOX enzyme, several concentrations of Atto 488 solutions were analyzed using an Agilent Cary 100 UV-Vis spectrophotometer to determine their respective absorption. From these results, a calibration curve could be made (Figure S2), with the absorbance vs concentration. Finally, the absorbance of the GOx-Atto 488 solution was measured, and from the calibration curve, the concentration of dye could be determined using the Beer-Lambert law: $A=c.\text{Ɛ}.l$, with A being the absorbance, c the concentration (M), l the optical path length (cm) and Ɛ the molar absorption coefficient (M^{-1} cm^{-1}). Here, the molar absorption coefficient of Atto 488 equal to 90 000 $cm^{-1}M^{-1}$ at 498 nm. It was determined that 43.5% of dye was conjugated to the enzyme. The coupling reaction was also qualitatively proven from the shift of the auto-correlation curve as measured by FCS.

Microscopic observation of enzymes sequestration in coacervates: To demonstrate the capacity of ELP[M1V3-80] coacervates to segregate different enzymes such as GOx-Atto 488 and HRP-Rhod, 1 $mg.mL^{-1}$ of tagged enzymes were encapsulated within 1 $mg.mL^{-1}$ ELP[M1V3-80] in an 8 wt% PEG solution. The solutions were then heated at 25°C, in order to phase separate and assemble the ELP[M1V3-80] coacervates. They were then imaged in an imaging chamber (Ibidi GmbH, Germany), using a confocal laser scanning microscopy (Leica, SP5 AOBS) through an HCX PL APO 63×, NA 1.4 oil immersion objective. Argon and DPPS561 lasers were used to excite Atto 488 and rhodamine dyes respectively. The Pearson's coefficient could not be used to determine the percentage of co-localization of the enzymes within the coacervates as the assembled

coacervates were too small to be analysed with a too high mobility compared to our acquisition set-up.

Fluorescence Correlation Spectroscopy (FCS): To proceed to FCS measurements, an inverted laser scanning confocal microscope (LSM 880, Carl Zeiss, Germany) with a water immersion objective (Zeiss C/Apochromat, M = 40, NA = 1.2) was used. A 488 nm argon laser was used to excite Atto 488, a DPPS561 laser was used to excite rhodamine, and a 633 nm HeNe laser was used to excite Bodipy (Bdpi). The lasers were passed through MBS488, MBS488/561, MBS488/561/633 filters, and the signals were detected in the range of 500–532 nm, 580-610 and 657–690 nm, respectively. The pinhole size (34 µm, 1 AU) was adjusted before recording FCS curves of the free dye. For FCS measurements, the following solutions were prepared, taken from our previous work:[22]

Table 4: Solution composition for FCS analysis.

	T_{cp} = 35 °C	T_{cp} = 10 °C
Free dyes	10 nM	10 nM
HRP-Rhodamine	-	10 nM
Gox-Atto 488	-	10 nM
ELP-Bdpi	10 nM	10 nM
ELP-*b*-PEG	0.125 mg/ml	0.364 mg/ml
ELP M60	0.25 mg/ml	0.723 mg/ml
PEG	8 wt%	20.8 wt%

Due to the high sensitivity of the device, 10 µl of each prepared solution was diluted with 10 µl of water, and placed on a 0.15 mm thick glass coverslip mounted on the microscope stage. Diluting the solutions avoided crashing the measurements due to the high number of big coacervates in the samples. To maintain the coacervated state of the ELPs due to dilution, incubation chamber was set at 37°C. Fluorescence signals from free fluorophore, Atto488/Rhodamine-labelled enzyme/Bdpi-labelled ELP and coacervates loaded with Atto488/Rhodamine-labelled

enzyme/Bdpi-labelled ELP were measured in a real time (5 s with 30 repetitions) and autocorrelation function was obtained by a QuickFit 3.0 software calculator. The experimental autocorrelation curves for the free fluorophore were fitted according to Equation (1) with a one component diffusion model:

$$G(\tau) = 1 + \left(1 + \frac{T}{1-T} e^{-\left(\frac{\tau}{\tau_{trip}}\right)}\right) \frac{1}{N} \left[\frac{1}{1+\frac{\tau}{\tau_D}\sqrt{1+R^2\frac{\tau}{\tau_D}}}\right] \quad (1)$$

where N represents the average number of particles in the observation volume, τ_D is the diffusional correlation time and R is the structural parameter, set to 5. T is the fraction of molecules in triple state, while τ_{trip} is the triplet time. The diffusion coefficient D was calculated using the relation between the x–y dimension of the confocal volume (ω_{xy}) and τ_D as in following Equation (2):

$$\tau_D = \frac{\omega_{xy^2}}{4D} \quad (2)$$

Dual-color fluorescence cross-correlation spectroscopy (FCCS) was performed using both lasers simultaneously. A two-component diffusion model, presented in Equation (3) was used for fitting the experimental autocorrelation curves for the free labelled enzyme and the coacervate encapsulating labelled enzyme:

$$G(\tau) = 1 + \left(1 + \frac{T}{1-T} e^{-\left(\frac{\tau}{\tau_{trip}}\right)}\right) \frac{1}{N} \left[\frac{1}{1+\frac{\tau}{\tau_{D_1}}\sqrt{1+R^2\frac{\tau}{\tau_{D_1}}}} + \frac{f_2}{1+\frac{\tau}{\tau_{D_2}}\sqrt{1+R^2\frac{\tau}{\tau_{D_2}}}}\right] \quad (3)$$

5. Supporting information

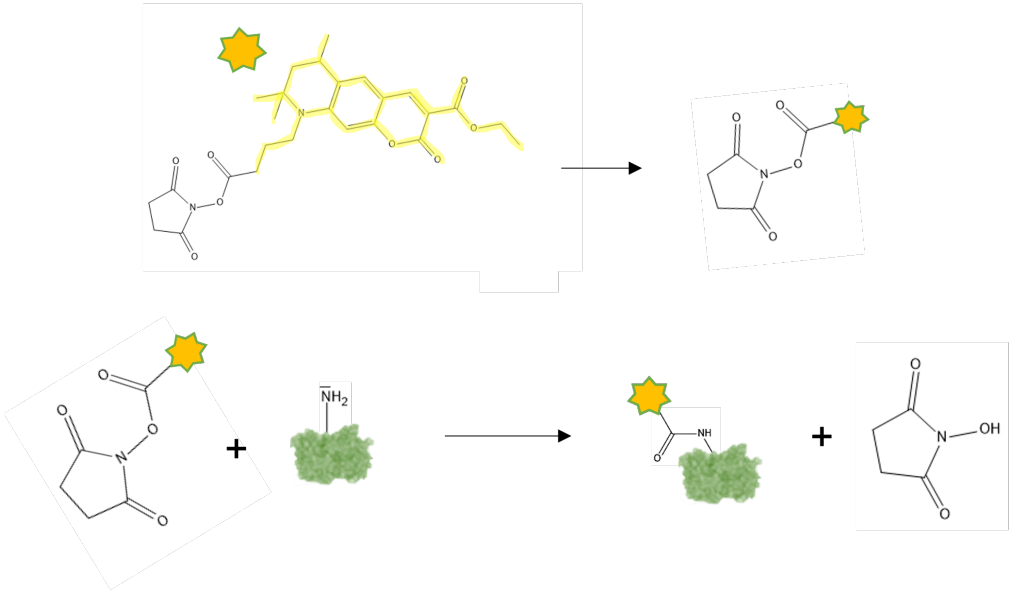

Figure S1: Click reaction of Atto 488 on Glucose Oxidase.

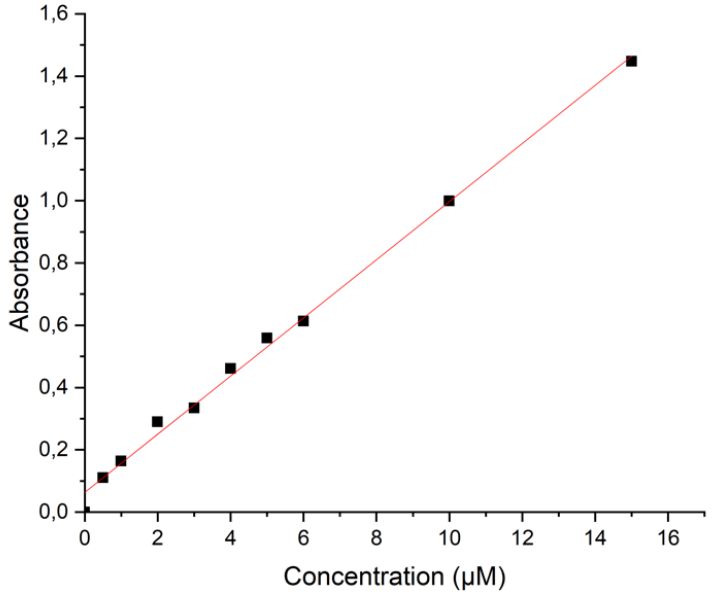

Figure S2: Calibration curve of Atto 488.

Table S1: Compound diffusion times quantified by FCS

Compounds	Free dye			Dye-labelled enzyme/ELP			Coacervates +		
	Atto 488	Rhodamine	Bdpi	GOx-Atto 488	HRP-Rhodamine	Bdpi-ELP	GOx-Atto 488	HRP-Rhodamine	ELP-Bdpi
Diffusion time (τ_D) (µs)	40	21	50	629	230	305	33669	44708	23549

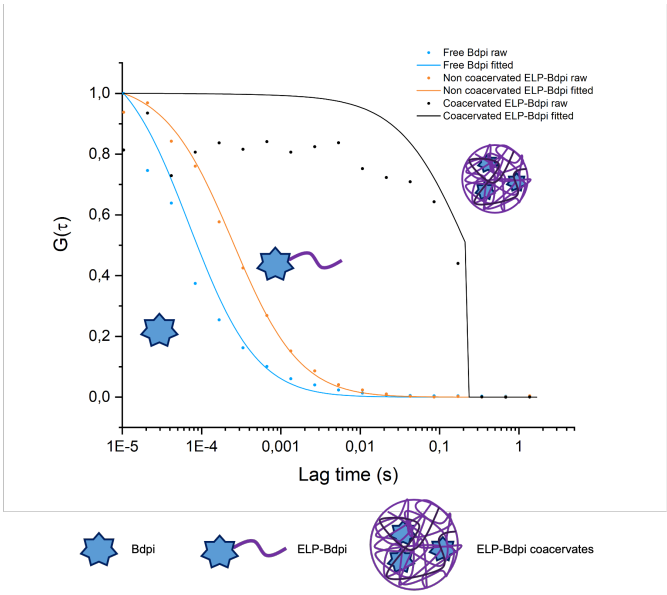

Figure S3: Normalized FCS autocorrelation curves of free Bdpi dye (cyan), non-coacervated ELP-Bdpi (orange) and coacervated ELP-Bdpi (black).

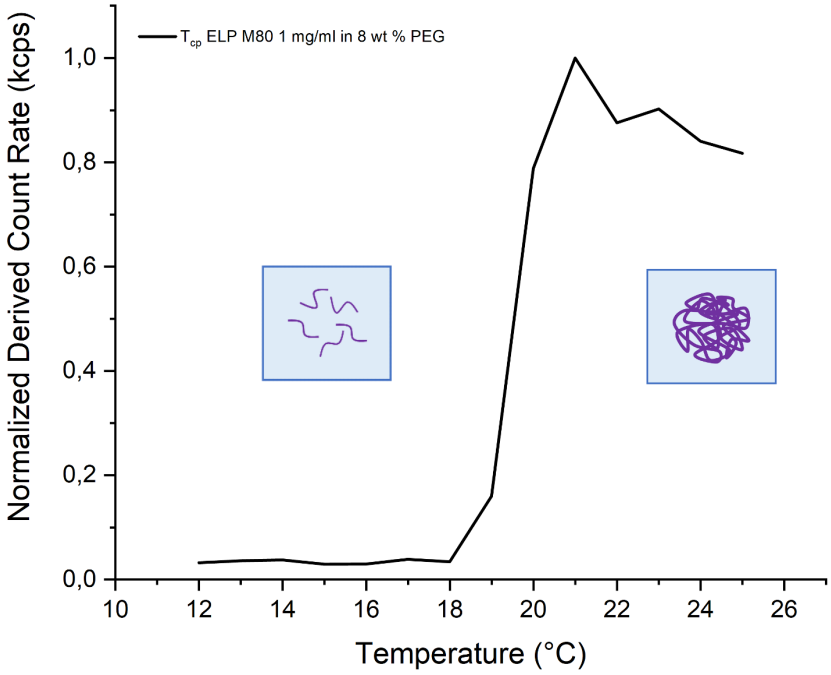

Figure S4: DLS analysis (measurement of the scattered light intensity, also referred to as the normalized derived count rate, DCR) to determine the T_{cp} of 1 mg mL^{-1} ELP M80 in a cell-like crowded environment.

6. References

[1] P. A. Beales, B. Ciani, S. Mann, *Interface Focus.* **2018**, *8*, 20180046.
[2] M. Marguet, C. Bonduelle, S. Lecommandoux, *Chem. Soc. Rev.* **2013**, *42*, 512–529.
[3] R. Roodbeen, van Hest J. C. M., *BioEssays* **2009**, *31*, 1299–1308.
[4] C. P. Brangwynne, C. R. Eckmann, D. S. Courson, A. Rybarska, C. Hoege, J. Gharakhani, F. Jülicher, A. A. Hyman, *Science* **2009**, *324*, 1729–1732.
[5] A. A. M. André, E. Spruijt, *Int J Mol Sci* **2020**, *21*, 5908.
[6] N. Martin, *ChemBioChem* **2019**, *20*, 2553–2568.
[7] N. A. Yewdall, A. A. M. André, T. Lu, E. Spruijt, *Current Opinion in Colloid & Interface Science* **2021**, *52*, 101416.
[8] C. D. Crowe, C. D. Keating, *Interface Focus* **2018**, *8*, 20180032.
[9] S. C. Weber, C. P. Brangwynne, *Cell* **2012**, *149*, 1188–1191.
[10] J. R. Simon, N. J. Carroll, M. Rubinstein, A. Chilkoti, G. P. López, *Nature Chem* **2017**, *9*, 509–515.
[11] D. E. Meyer, A. Chilkoti, *Nat Biotechnol* **1999**, *17*, 1112–1115.
[12] D. W. Urry, *J. Phys. Chem. B* **1997**, *101*, 11007–11028.
[13] F. G. Quiroz, A. Chilkoti, *Nature Mater* **2015**, *14*, 1164–1171.

[14] C. Love, J. Steinkühler, D. T. Gonzales, N. Yandrapalli, T. Robinson, R. Dimova, T. -Y. D. Tang, *Angew. Chem.* **2020**, *132*, 6006–6013.
[15] R. Booth, Y. Qiao, M. Li, S. Mann, *Angew. Chem. Int. Ed.* **2019**, *58*, 9120–9124.
[16] S. Deshpande, F. Brandenburg, A. Lau, M. G. F. Last, W. K. Spoelstra, L. Reese, S. Wunnava, M. Dogterom, C. Dekker, *Nat Commun* **2019**, *10*, 1800.
[17] D. Garenne, L. Beven, L. Navailles, F. Nallet, E. J. Dufourc, J.-P. Douliez, *Angew. Chem.* **2016**, *128*, 13673–13677.
[18] P. Baumann, M. Spulber, O. Fischer, A. Car, W. Meier, *Small* **2017**, *13*, DOI 10.1002/smll.201603943.
[19] T. Vöpel, G. I. Makhatadze, *PLoS One* **2012**, *7*, e39418.
[20] R. Petitdemange, Chemoselective Modifications of Recombinant Elastin-like Polypeptides: Tuning Thermosensitivity and Bioactivity, Bordeaux, **2016**.
[21] J. R. Kramer, R. Petitdemange, L. Bataille, K. Bathany, A.-L. Wirotius, B. Garbay, T. J. Deming, E. Garanger, S. Lecommandoux, *ACS Macro Lett.* **2015**, *4*, 1283–1286.
[22] C. Schvartzman, H. Zhao, E. Ibarboure, V. Ibrahimova, E. Garanger, S. Lecommandoux, *Advanced Materials* **2023**, 2301856.
[23] R. Petitdemange, E. Garanger, L. Bataille, W. Dieryck, K. Bathany, B. Garbay, T. J. Deming, S. Lecommandoux, *Biomacromolecules* **2017**, *18*, 544–550.
[24] R. Petitdemange, E. Garanger, L. Bataille, K. Bathany, B. Garbay, T. J. Deming, S. Lecommandoux, *Bioconjugate Chem.* **2017**, *28*, 1403.
[25] Y. Xiao, Z. S. Chinoy, G. Pecastaings, K. Bathany, E. Garanger, S. Lecommandoux, *Biomacromolecules* **2020**, *21*, 114–125.
[26] H. Zhao, V. Ibrahimova, E. Garanger, S. Lecommandoux, *Angew. Chem. Int. Ed.* **2020**, *59*, 11028–11036.
[27] ATTO-TEC, "Recommended Procedures for Labeling," can be found under https://www.atto-tec.com/fileadmin/user_upload/Katalog_Flyer_Support/Procedures, **n.d.**

Conclusion and Perspectives

The overall aim of this thesis was to take a step forward in the development of artificial cells by adding new structural and functional features to the existing toolbox in this field. Over the past decade, significant progress has been made in mimicking eukaryotic cells, with synthetic structures increasingly resembling their biological counterparts and providing a deeper understanding of their mechanical, (bio)chemical, and physical properties.

From a structural perspective, our first focus was to demonstrate the possible co-encapsulation of membranebound and membraneless organelles using a microfluidic system. These components can coexist without interfering with one another, as the presence of membrane-bound nanoparticles did not disrupt the Liquid-Liquid Phase Separation (LLPS) and coacervation of Elastin-Like Polypeptide (ELP), which serves as a model of membraneless organelles. This achievement opens exciting possibilities for building artificial cells from a bottom-up assembly and investigating novel functions and interactions between these types of organelles, as it would naturally occur in eukaryotic cells.

Our research then mainly focused towards membraneless organelles, and their assembly through Liquid-Liquid Phase Separation. These particular structures have been integrated in partially dewetted liposomes, strategy developed to investigate the ability of phase separation of enzyme-functionalized ELPs into a crowded biomacromolecule's environment mimicking the cell cytoplasm. Thanks to osmotic pressure modulation, the characteristic cloud point temperature (T_{cp}) of ELPs could be tuned so that synthetic organelle compartments of an ELP-based multicomponent system with HRP as a model enzyme could be formed as a response to hyperosmotic stress. In functional terms, the importance of assembling these synthetic organelles has been demonstrated for accelerating enzymatic reactions by locally increasing enzyme concentration. This work proposes a unique approach to create protocellular systems with a new osmotic trigger to dynamically assemble intracellular synthetic organelle formation. It also represents a significant advance towards the construction and induction of complex cascade reactions in more realistic synthetic cells, promising to further our understanding of the importance and role of membraneless organelles in biological enzymatic reactions.

Finally, we used fluorescence correlation spectroscopy to demonstrate the uptake of labeled enzymes by ELP coacervates, providing greater insights on the interactions between these compounds compared to our previous investigations. Through kinetic analysis and confocal microscopy observations, we gained insights into the limited likelihood of co-encapsulating two enzymes within a single coacervate. We first showed that a single enzyme (HRP) can be efficiently confined in free ELP coacervates, leading to an acceleration of the enzymatic reaction, without the need for a bioconjugation reaction. The system was made more complex and a cascade reaction combining GOx and HPR was tested under the same conditions. The resulting kinetic analysis enabled us to conclude that the probability of co-encapsulating two enzymes in a single coacervate was low, reinforced by confocal microscopy observations. As a possible solution to this problem, the size of the coacervates could be increased to give a higher probability of having several enzymes in a single coacervate. Another possible solution could be to conjugate each enzyme to an ELP, as was done in our previous work, again to increase the chances of finding them together in the same coacervate.

All these exciting advances open up fascinating possibilities for the development of artificial cells through bottom-up assembly and for exploring new functions and interactions between these organelle types, much like natural eukaryotic cells.

What comes next?

As previously mentioned, various aspects of eukaryotic cells have been artificially replicated, with some playing pivotal roles in these unique structures. These fundamental attributes include energy supply, metabolism, protein expression, communication, replication of genetic material, growth, motility, compartmentalization and cell division.[1–4] This latter is of particular interest for our future projects.

Given our recent achievements in controlling the LLPS of ELPs in response to osmotic changes, we are now exploring the prospect of integrating these systems with an Aqueous Two-Phase System (ATPS) composed of Polyethylene glycol (PEG) and Dextran, serving as a synthetic cytoplasm and crowding agent. A phase diagram of PEG-Dextran has been completed at 25°C to determine at which molar concentrations of the polymers we had a one- and two-phase system. As

seen in Figure 1, below the coexistence curve, PEG and Dextran are miscible and form a one-phase system (Figure 2a-b). Above the coexistence curve, PEG and Dextran phase separate into a two-phase system (Figure 2c-d). The overall structure will be encapsulated within hybrid lipid/polymer vesicles made of 1-palmitoyl-2-oleoyl-sn-glycero-3-phosphocholine (POPC) and poly(dimethylsiloxane)-*g*-poly(ethyleneglycol) (PDMSgPEO).

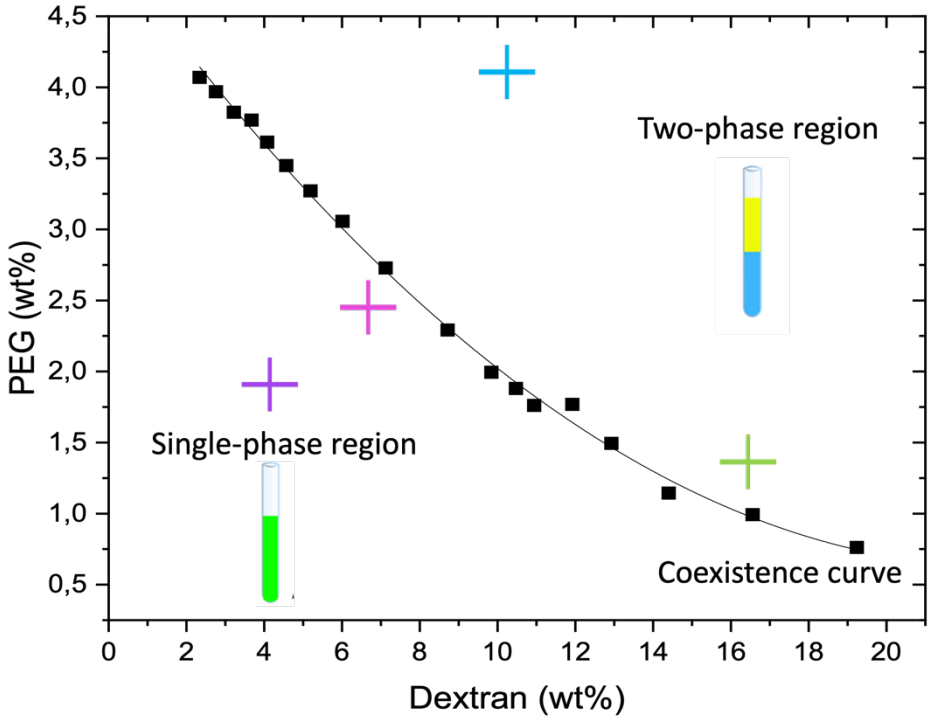

Figure 1: Phase diagram of PEG-Dextran system conducted at 25°C.

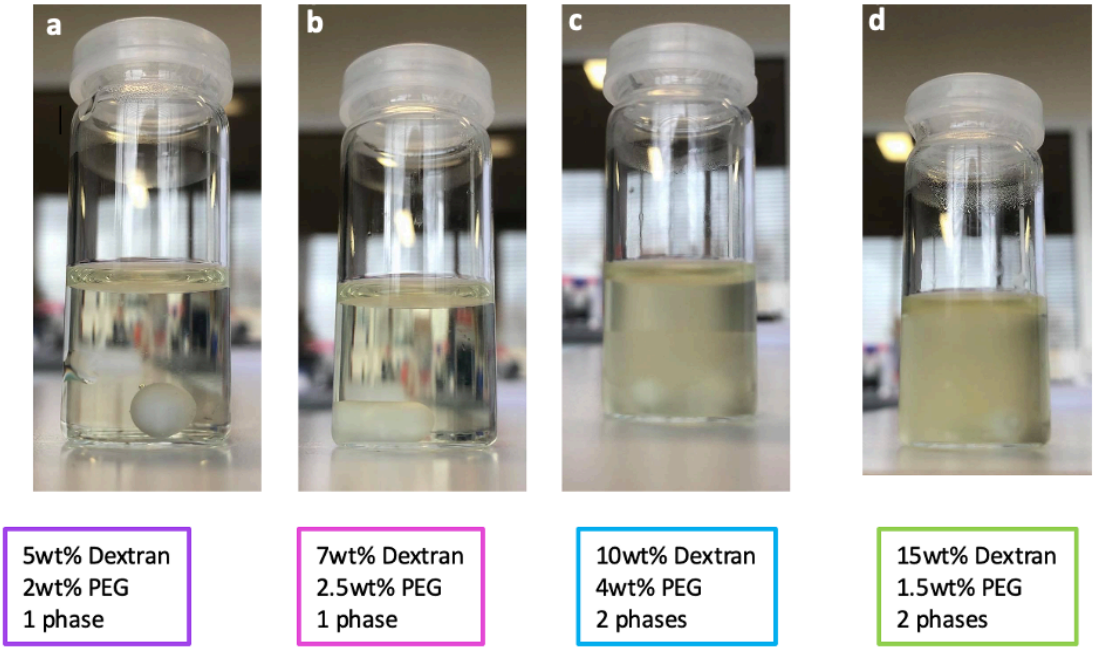

Figure 2: Molar concentration variations of PEG and Dextran (a-b) one-phase system (c-d) two-phase system.

The integration of an ATPS offers several advantages. First, it allows to observe how bio(macro)molecules preferentially and selectively partition within this complex system, as it has previously been demonstrated by Zhao *et al*.[5] Second, integrating an ATPS phase within the vesicles induces membrane reorganization. Indeed, by encapsulating ATPS molar concentrations slightly below the binodal curve (e.g., 7wt% Dextran and 2.5wt% PEG) and inducing an osmotic shock will locally concentrate the two polymers and hence, shift the system from a one-phase to two-phase system (Figure 3a-b). Therefore, the two distinct phases of PEG and Dextran can be observed within the vesicle, with the Dextran characteristically wetting the membrane as it is the denser phase, as previously reported by Dimova (Figure 3c).[6]

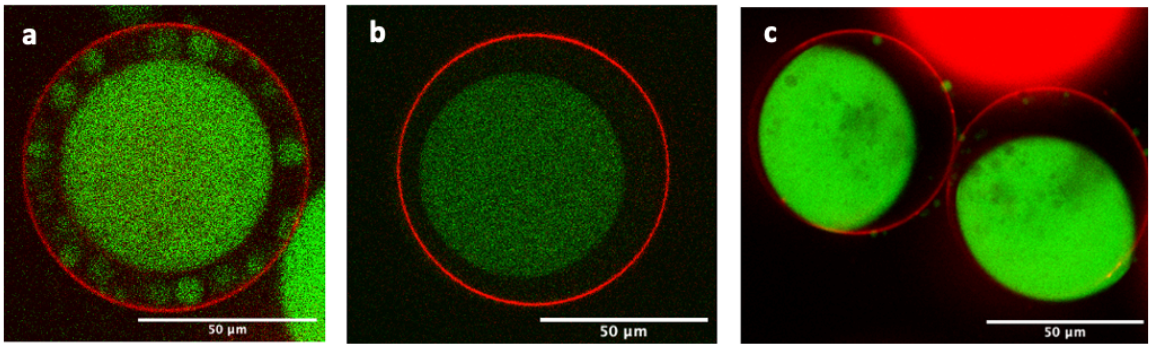

Figure 3: Encapsulation of ATPS in double-emulsions a) few minutes after collection of the droplets, observe the beginning of phase separation between the dextran phase (in green) and the PEG phase (in black) The membrane is depicted in red b) full separation of the two phases after osmotic shock c) full wetting of the membrane by Dextran.

This phase separation induces a reorganization within the membrane, as Dextran has more favorable interactions with lipids, and PEG with polymers.[7,8] Hence, the formation of domains should be visible on the membrane. Finally, a last osmotic shock will be induced to facilitate the scission between the nascent daughter cells. The emergence of two distinct daughter cells from one mother cell is expected, each possessing unique membrane compositions and encompassing biomacromolecules, enzymes, and organelles that have selectively partitioned within each respective ATPS phase (Figure 4).

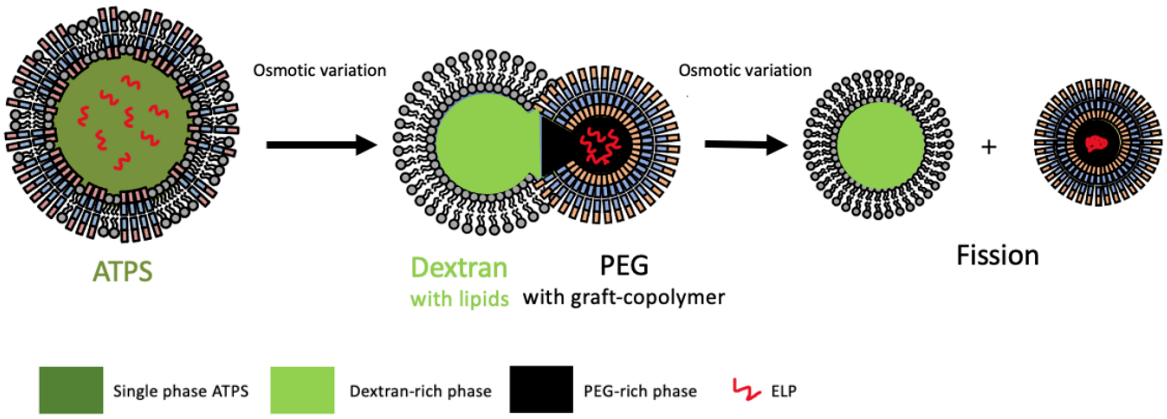

Figure 4: Synthetic cell construct and division of a mother cell into two distinct daughter cells.

Reaching this technical prowess would combine key structural and functional characteristics of live biological cells such as mimicking the biomembrane, the cytoplasm, organelles, the division of a mother cell into two daughter cells and reactions in confined environments. Unfortunately, due to a lack of time, the complete demonstration of such process has not been achieved.

References

[1] Z. Liu, W. Zhou, C. Qi, T. Kong, *Advanced Materials* **2020**, *32*, 2002932.
[2] B. C. Buddingh', J. C. M. Van Hest, *Acc. Chem. Res.* **2017**, *50*, 769–777.
[3] C. Guindani, L. C. Da Silva, S. Cao, T. Ivanov, K. Landfester, *Angew Chem Int Ed* **2022**, *61*, DOI 10.1002/anie.202110855.
[4] W. Jiang, Z. Wu, Z. Gao, M. Wan, M. Zhou, C. Mao, J. Shen, *ACS Nano* **2022**, *16*, 15705–15733.
[5] H. Zhao, V. Ibrahimova, E. Garanger, S. Lecommandoux, *Angew. Chem. Int. Ed.* **2020**, *59*, 11028–11036.
[6] Y. Li, R. Lipowsky, R. Dimova, *J. Am. Chem. Soc.* **2008**, *130*, 12252–12253.
[7] C. D. Keating, *Acc. Chem. Res.* **2012**, *45*, 2114–2124.
[8] M. S. Long, A.-S. Cans, C. D. Keating, *J. Am. Chem. Soc.* **2008**, *130*, 756–762.

Title: From structure to bioactivity: exploring confinement effects in multicompartment and multicomponent vesicles

Abstract: Artificial cells are designed to replicate the characteristics of natural cells, allowing scientists to investigate biological processes and the origin of life. In the last decades, there has been a significant advancement in creating artificial cells through both top-down and bottom-up approaches. Various materials such as lipids, polymers, lipid/polymer hybrids, natural cell membranes, colloids and coacervates have been used to fabricate various artificial cell components. These materials can be modified by introducing proteins and genes onto the cell surface or encapsulating them inside the cells, which determine the properties of artificial cells. These properties encompass functions such as energy generation, cellular growth, morphological alterations, division, transmembrane transportation, environmental responsiveness, and mobility. Herein, compartmentalization has been our main focus of research as it orchestrates every reaction and function of eukaryotic cells. This involved various approaches ranging from the co-encapsulation of membranebound and membraneless organelles within one single vesicle, to controlling the Liquid-Liquid Phase separation of functional thermo-responsive Elastin-Like Polypeptides to assemble membraneless organelles. This has been a unique way to fine-tune enzymatic reactions dynamically as a response to an osmotic change in isothermal conditions. Finally, our in-depth analysis of the interactions between enzymes and coacervates has yielded invaluable insights into this intricate process.

Keywords: Artificial cells, Elastin-Like Polypeptides, Liquid-Liquid Phase Separation, Microfluidics, Synthetic Organelles, Self-assembly.

Titre : De la structure à la bioactivité : étude des effets de confinement dans les vésicules multi-compartimentées et multicomposantes

Résumé : Les cellules artificielles sont conçues pour reproduire les caractéristiques des cellules naturelles, permettant ainsi l'étude de processus biologiques complexes et l'origine de la vie. Au cours des dernières décennies, il y a eu des avancées significatives dans la création de cellules artificielles grâce à des approches ascendantes et descendantes. Divers matériaux tels que les lipides, les polymères, les hybrides lipides/polymères, les membranes cellulaires naturelles, les colloïdes et les coacervats ont été utilisés pour fabriquer de telles cellules artificielles. Ces matériaux peuvent être modifiés en introduisant des protéines et des gènes à la surface de la cellule ou en les encapsulant à l'intérieur de celles-ci afin de leur conférer certaines propriétés. Ces dernières englobent des fonctions telles que la production d'énergie, la croissance et division cellulaire, le transport transmembranaire et la mobilité. Dans le cadre de cette thèse, la compartimentalisation a été notre principal domaine d'intérêt car elle orchestre de nombreuses réactions et fonctions des cellules eucaryotes. Cela implique diverses approches, allant de la co-encapsulation d'organites avec membrane et sans membrane dans une seule vésicule, à la maîtrise de la séparation de phase liquide-liquide des polypeptides thermo-sensibles tels que l'élastine pour assembler des organites sans membrane. Cela a constitué une manière unique d'ajuster dynamiquement des réactions enzymatiques modèles en réponse à un changement de pression osmotique dans des conditions isothermes. Enfin, notre analyse approfondie des interactions entre les enzymes et les coacervats a permis de fournir des explications sur ce processus complexe.

Mots clés : Cellules artificielles, Élastine-Like Polypeptides, Séparation de Phase Liquide-Liquide, Microfluidique, Organites Synthétiques, Auto-assemblage.